The stability of gravity-driven viscous films over topography

Von der Fakultät für Ingenieurwissenschaften
der Universität Bayreuth
zur Erlangung der Würde eines
Doktor-Ingenieur (Dr.-Ing.)
genehmigte Dissertation

von
Dipl.-Phys. Mario Schörner
aus
Rehau

Erstgutachter:	Prof. Dr. N. Aksel
Zweitgutachter:	Prof. Dr. Y. Trifonov
Tag der mündlichen Prüfung:	03. September 2018

Lehrstuhl für Technische Mechanik und Strömungsmechanik
Universität Bayreuth
2018

Journal publications

- Nuri Aksel and Mario Schörner:
  Films over topography: from creeping flow to linear stability, theory, and experiments, a review.
  Acta Mechanica, **229**, 1453–1482 (2018).

- Mario Schörner and Nuri Aksel:
  The stability cycle – A universal pathway for the stability of films over topography.
  Physics of Fluids, **30**, 012105 (2018).

- Mario Schörner, Daniel Reck, Nuri Aksel and Yuri Trifonov:
  Switching between different types of stability isles in films over topographies.
  Acta Mechanica, **229**, 423–436 (2018).

- Markus Dauth, Mario Schörner and Nuri Aksel:
  What makes the free surface waves over topographies convex or concave? A study with Fourier analysis and particle tracking.
  Physics of Fluids, **29**, 092108 (2017).

- Mario Schörner, Daniel Reck and Nuri Aksel:
  Stability phenomena far beyond the Nusselt flow – Revealed by experimental asymptotics.
  Physics of Fluids, **28**, 022102 (2016).

- Mario Schörner, Daniel Reck and Nuri Aksel:
  Does the topography's specific shape matter in general for the stability of film flows?
  Physics of Fluids, **27**, 042103 (2015).

- Mario Schörner, Sebastian R. Beyer, June Southall, Richard J. Cogdell and Jürgen Köhler:
  Conformational Memory of a Protein Revealed by Single-Molecule Spectroscopy.
  Journal of Physical Chemistry B, **119**, 13964–13970 (2015).

- Mario Schörner, Sebastian R. Beyer, June Southall, Richard J. Cogdell and Jürgen Köhler:
  Multi-Level, Multi Time-Scale Fluorescence Intermittency of Photosynthetic LH2 Complexes: A Precursor of Non-Photochemical Quenching?
  Journal of Physical Chemistry B, **119**, 13958–13963 (2015).

Abstract

The gravity-driven flow of a viscous film over an inclined surface is a fundamental problem in fluid mechanics. This type of flow serves as a model to catch the physics behind a wide range of technical and environmental processes which silently affect our lives. The most simplified case of this basic hydrodynamic configuration is the flow of a viscous film over an infinitely extended and perfectly flat substrate, which even has an exact analytical solution. However, in the real world, the substrates on which the films move are frequently rough – either intentionally or accidentally. The great challenge arises that, in general, the flows over such inclined topographies cannot be calculated analytically from the Navier-Stokes equations. The interaction between the underlying topography and the fluid layer results in a complicated dynamical behavior and gives rise to, e.g., the formation of eddies in the troughs and resonant standing waves at the flow's free surface. As already small substrate defects can significantly affect the film flows, the requirement for predictable product and process properties in coating industries generated considerable interest in improving the understanding of the associated flow mechanisms.

Since the interface between the liquid and the surrounding gas is a deformable boundary, waves can appear spontaneously at the free surface if a critical volume flux is exceeded. These waves are the reaction of the system to disturbances, like external forcing or ambient noise, and grow or shrink on their way downstream. Dependent on the volume flux, the perturbation's frequency, and the interaction between the fluid and the topography a complicated topology of stable (waves are damped) and unstable (waves are amplified) flow regimes appears. In medical and semiconductor industries, where uniformly thin coatings are essential, the formation of these waves gives rise to great difficulties in the manufacturing processes. As a pure analytical treatment of the vast majority of these hydrodynamic systems is impossible today, thorough experimental investigations and comprehensive computational modelings are inalienable to improve the understanding of the associated flow mechanisms.

The present dissertation deals with the effects of different types of topographies on the free surface stability of gravity-driven viscous films. Comprehensive new experiments were combined with all existing analytical, numerical and experimental findings on this complex problem. That way, new flow phenomena were uncovered and attributed to the fundamental mechanisms which determine the flow dynamics. The aim of the present study was to characterize these results for the sake of unveiling a universally valid principle, being able to describe and unify all findings on the stability of gravity-driven viscous film flows.

The first step in order to unveil whether the above-mentioned universal principle indeed exists was to investigate whether the flows over different topographies can exhibit the same stability behavior, or whether all systems are intrinsically different in terms of their stability. A fundamental question arose from this thought: does the topography's specific shape matter in general for the linear stability of gravity-driven viscous films? In order to understand this complex problem, five topographies of different shapes (e.g., sinusoidal and rectangular), but equal amplitude, wavelength, and inclination against the horizontal were chosen as a model for the different types of rough substrates in real-world film flows. For each topography, the basic flow was characterized by measuring the flow field and the free surface contour. Experiments on the

flow's linear stability followed. That way, insights into how the topography's specific shape can manipulate both the basic flow and the linear stability of gravity-driven films were obtained. In particular, as long as the steady-state free surface remained unchanged, modifications of the topography's specific shape were found to not affect the linear stability of this type of flow.

The subsequent parameter study went one step further in order to unveil the phenomena which are decisive for the flow's stability. In the experiments, the well-known Nusselt flow over a flat incline was asymptotically left, either by gradually increasing the amplitude of sinusoidal undulations or by decreasing the tip width of rectangular corrugations. Systematic variations of the channel's inclination, the fluid's viscosity and the topography's wavelength followed. That way, nontrivial stability charts and phenomena far beyond the Nusselt flow were revealed. For the sake of understanding these phenomena, the steady-state velocity fields of the respective flows were measured. This comprehensive approach provided the exceptional opportunity to unveil that the complex shape, which stability charts of films over inclined topographies exhibit, can be attributed to the simultaneous presence of stabilizing as well as destabilizing effects, both provoked by the topography. The stabilization of the flow due to an increased film thickness and the destabilization of the flow due to resonant standing waves were shown to be competing effects. Which effect dominates in this competition depends primarily on the amplitude, tip width, wavelength, and inclination of the topography and on the viscosity of the fluid.

The systematic parameter variations mentioned above uncovered a switching between different types of stability isles, i.e. between stable and unstable regions in the linear stability charts. This abrupt change of the flow's free surface stability was detected for all system parameters varied and gave rise to an intriguing question: Is there a universal principle, being valid to describe the parametric evolution of the flow's linear stability chart for variations of different system parameters? In search of an answer to this question, all experimental and numerical stability charts available in the literature were screened. New experiments were carried out only to fill the gaps which remained in the combined parameter space of all precedent work. Variations of the fluid's viscosity and the topography's specific shape, amplitude, wavelength, tip width and inclination were considered. That way, a set of six characteristic patterns of stability charts was identified to be sufficient and powerful enough to uniformly describe all available linear stability charts of two-dimensional Newtonian films flowing over periodically corrugated inclines. No counterexample was found, which did not fit to one of these six patterns. Based on these six stability patterns, a universal pathway – the 'stability cycle' – was unveiled, along which the linear stability charts of all considered films evolved when the system parameters were changed. The physical significance of the stability cycle is at hand, as it is a universal guide on how to tune the linear stability of viscous films in a way which is desired.

The characteristic stability chart patterns and the stability cycle were found to be valid for all two-dimensional Newtonian films, which are perturbed by linear free surface waves, and flowing down periodically undulated inclines. No contradicting observations are reported. Yet, it remained an open question whether similar phenomena can also be found for other systems like, e.g., non-Newtonian fluids, nonlinear waves, or three-dimensional channel flow with sidewalls. By briefly considering these three exemplary systems, the study presented in the last part of this thesis went beyond the linear stability of two-dimensional Newtonian films. New steady-state flow phenomena were uncovered with their potential effects on the flow's stability being discussed. Although an in-depth investigation of these systems is beyond the scope of this thesis, all results indicate that the characteristic stability chart patterns and the stability cycle are, with some restrictions, still valid beyond the linear stability of two-dimensional Newtonian films.

Zusammenfassung

Die schwerkraftgetriebene Strömung eines viskosen Flüssigkeitsfilms über einen geneigten Untergrund ist ein fundamentales Problem der Strömungsmechanik. Diese Klasse von Strömungen dient als physikalisches Modell für eine Vielzahl von Prozessen in Natur und Technik, die ganz im Stillen unser aller Leben beeinflussen. Der einfachste Fall dieser hydrodynamischen Grundkonfiguration ist der Fluss eines viskosen Films über ein unendlich ausgedehntes und flaches Substrat, für den es sogar eine exakte analytische Lösung gibt. In der realen Welt sind die Böden, auf denen sich die Flüssigkeitsfilme bewegen, jedoch häufig rau – entweder aus Absicht oder durch Zufall. Es stellt eine große Herausforderung dar, dass die Strömung über derartige Topographien im Allgemeinen nicht mehr analytisch berechnet werden kann. Die Wechselwirkung zwischen der zugrunde liegenden Bodenstruktur und der darüber fließenden Flüssigkeitsschicht führt zu einer komplizierten Dynamik, die wiederum beispielsweise zu Wirbelbildung in den Mulden und zu stehenden Oberflächenwellen führt. Da bereits kleine Substratfehlstellen die Flüssigkeitsfilme sehr stark beeinflussen können, hat der Bedarf nach vorhersagbaren Produkt- und Prozesseigenschaften in der Beschichtungsindustrie ein erhebliches Interesse an einem besseren Verständnis der zugrunde liegenden Strömungsmechanismen hervorgerufen.

Die Grenzfläche zwischen der Flüssigkeit und dem sie umgebenden Gas stellt eine verformbare Grenze dar, an der es aufgrund von Trägheitseffekten bei Überschreitung eines kritischen Volumenstroms zur spontanen Bildung von stromabwärts laufenden Oberflächenwellen kommen kann. Diese Wellen sind die Reaktion des Systems auf Störungen, wie beispielsweise externe Anregungen oder das allgegenwärtige Umgebungsrauschen. Abhängig vom Volumenstrom, von der Frequenz der Störung und von der Wechselwirkung zwischen der Flüssigkeit und dem gewellten Boden tritt ein komplexes Gebilde aus stabilen (die Wellen werden gedämpft) und instabilen (die Wellen werden verstärkt) Strömungsgebieten auf. In der Medizin- und Halbleiterindustrie, wo es auf gleichmäßig dünne Beschichtungen ankommt, gehen mit der Bildung dieser Wellen allerdings große Schwierigkeiten in den Fertigungsprozessen einher. Da für die überwiegende Mehrheit dieser hydrodynamischen Systeme eine rein analytische Behandlung derzeit jedoch unmöglich ist, sind gründliche experimentelle Untersuchungen und umfassende computergestützte Modellierungen unabdingbar, um das Verständnis der zugrunde liegenden Mechanismen zu verbessern.

Die hier vorliegende Dissertation beschäftigt sich mit den Auswirkungen gewellter Substrate auf die Stabilität der freien Oberfläche schwerkraftgetriebener viskoser Filmströmungen. Umfassende neue Experimente wurden mit allen vorhandenen analytischen, numerischen und experimentellen Erkenntnissen über dieses komplexe Problem kombiniert. Auf diese Art und Weise wurden neue Strömungsphänomene entdeckt und fundamentalen Mechanismen zugeschrieben, welche die Dynamik der Strömung bestimmen. Ziel der vorliegenden Arbeit war es insbesondere, die so gewonnenen Ergebnisse zu charakterisieren, um ein allgemeingültiges Prinzip zu entwickeln, das alle Erkenntnisse über die Stabilität schwerkraftgetriebener viskoser Filmströmungen beschreiben und vereinheitlichen kann.

Der erste Schritt um herauszufinden, ob das oben genannte universelle Prinzip tatsächlich existiert, bestand darin zu untersuchen, ob Strömungen über verschiedenartig gewellte Böden

überhaupt dasselbe Stabilitätsverhalten aufweisen können oder ob alle Systeme hinsichtlich ihrer Stabilität von sich aus verschieden sind. Aus dieser Überlegung heraus ergab sich eine grundlegende Frage: Ist die spezifische Form der Topographie im Allgemeinen für die lineare Stabilität schwerkraftgetriebener Filmströmungen von Bedeutung? Um dieses komplizierte Problem zu verstehen, wurden fünf Topographien unterschiedlicher Form (z.B. sinusförmig und rechteckig), aber gleicher Amplitude, Wellenlänge und Neigung gegenüber der Horizontalen als Modell für die verschiedenen Arten rauer Substrate, die in den Filmströmungen der realen Welt vorkommen können, gewählt. Für jede Topographie wurde die Grundströmung durch Messung sowohl des Strömungsfeldes als auch der Kontur der freien Flüssigkeitsoberfläche charakterisiert. Es folgten Experimente zur linearen Stabilität der Strömung. Auf diese Weise konnten Erkenntnisse darüber erzielt werden, wie die spezifische Form des gewellten Bodens sowohl die Grundströmung als auch die lineare Stabilität schwerkraftgetriebener Filmströmungen beeinflussen kann. Insbesondere konnte festgestellt werden, dass sich Änderungen der Topographieform nicht auf die lineare Stabilität dieser Art von Strömungen auswirken, solange die stationäre freie Oberfläche von diesen Veränderungen im Wesentlichen unbeeinflusst bleibt.

Die anschließende Parameterstudie ging noch einen Schritt weiter, um diejenigen Phänomene zu untersuchen, welche die Stabilität einer Filmströmung bestimmen. Dazu wurden Experimente durchgeführt, in denen die bekannte Nusselt-Strömung über eine flache geneigte Ebene asymptotisch verlassen wurde, indem entweder die Amplitude eines sinusförmigen Bodens stufenweise erhöht oder die Breite der Spitzen eines rechteckigen Bodens verringert wurde. Es folgten systematische Variationen der Kanalneigung, der Flüssigkeitsviskosität und der Wellenlänge der Bodentopographie. Auf diese Art und Weise kamen nicht-triviale Stabilitätskarten und Phänomene ans Licht, die sich stark von denen der Nusselt-Strömung unterschieden. Um diese Phänomene zu verstehen, wurden die Geschwindigkeitsfelder der zugehörigen stationären Strömungen gemessen. Durch diesen umfassenden Ansatz konnte belegt werden, dass die komplexe Form, welche die Stabilitätskarten von Filmströmungen über geneigten Topographien aufweisen, auf das gleichzeitige Vorhandensein stabilisierender und destabilisierender Topographieeffekte zurückzuführen ist. Die Stabilisierung der Strömung durch eine erhöhte Filmdicke und ihre Destabilisierung aufgrund der Resonanz der Strömung mit dem gewellten Boden erwiesen sich als konkurrierende Effekte. Welcher der beiden Effekte dominiert, hängt primär von der Amplitude, Spitzenbreite, Wellenlänge und Neigung des gewellten Bodens sowie von der Viskosität der Flüssigkeit ab.

Bei den oben genannten systematischen Parametervariationen konnte ein Hin- und Herschalten zwischen verschiedenen Arten von Stabilitätsinseln, d.h. zwischen abgeschlossenen stabilen und instabilen Bereichen in den linearen Stabilitätskarten, nachgewiesen werden. Diese Art der abrupten Änderung der Stabilität der freien Oberfläche konnte bei der Variation jedes untersuchten Systemparameters beobachtet werden, was zu einer weiteren interessanten Frage führte: Gibt es ein universelles Prinzip, das die parametrische Entwicklung der linearen Stabilitätskarte einer Filmströmung für die Veränderung mehrerer Systemparameter gleichermaßen beschreibt? Zur Beantwortung dieser Frage wurden alle in der Literatur verfügbaren experimentellen und numerischen Stabilitätskarten gesichtet. Die neu durchgeführten Experimente dienten ausschließlich dazu, die verbleibenden Lücken des kombinierten Parameterraums zu schließen. Es wurden die Viskosität der Flüssigkeit sowie die spezifische Form, Amplitude, Wellenlänge, Spitzenbreite und Neigung des Bodens variiert. Auf diese Art und Weise konnten sechs charakteristische Muster von Stabilitätskarten identifiziert werden, die in ihrer Gesamtheit ausreichend sind, um alle verfügbaren linearen Stabilitätskarten zweidimensionaler Newtonscher Filmströmungen, die schwerkraftgetrieben über gewellte Böden fließen, einheit-

lich zu beschreiben. Es wurde nicht ein einziges Gegenbeispiel gefunden, welches nicht durch eines dieser sechs Muster dargestellt werden konnte. Auf der Grundlage dieser Muster wurde ein universell gültiger Pfad – der Stabilitätszyklus – entdeckt, entlang dessen sich die linearen Stabilitätskarten aller untersuchten Filmströmungen entwickeln, wenn die im Rahmen dieser Arbeit betrachteten Systemparameter geändert werden. Die physikalische Bedeutung des Stabilitätszyklus liegt auf der Hand, denn er ist ein universeller Leitfaden dafür, wie die lineare Stabilität viskoser Filme derart modifiziert werden kann, dass sie den Anforderungen der jeweiligen Anwendung entspricht.

Die im Rahmen dieser Arbeit nachgewiesenen charakteristischen Stabilitätskartenmuster und der Stabilitätszyklus gelten für alle zweidimensionalen Newtonschen Filmströmungen, deren freie Oberfläche durch lineare Wellen gestört wird und die über periodisch gewellte, geneigte Böden fließen. Es gibt keinerlei Beobachtungen, die diese universelle Gültigkeit widerlegen. Dennoch bleibt die Frage offen, ob ähnliche Phänomene auch für andere Systeme, wie beispielsweise nicht-Newtonsche Flüssigkeiten, nichtlineare Wellen oder dreidimensionale Kanalströmungen mit Seitenwänden, gefunden werden können. Durch eine kurze Betrachtung dieser drei beispielhaften Systeme geht die hier vorliegende Arbeit über die lineare Stabilität zweidimensionaler Newtonscher Filme hinaus. Neue Phänomene wurden in den stationären Strömungen entdeckt und deren möglicher Einfluss auf die Stabilität der Strömung wurde kurz diskutiert. Obwohl eine tiefergehende Untersuchung dieser Systeme über den Rahmen dieser Arbeit hinausgehen würde, deuten alle bisherigen Ergebnisse darauf hin, dass sowohl die charakteristischen Stabilitätskartenmuster als auch der Stabilitätszyklus bis zu einem gewissen Grad über die lineare Stabilität zweidimensionaler Newtonscher Filmströmungen hinaus Gültigkeit besitzen.

Contents

1. Introduction: From creeping flow to the linear stability of films over topography

We encounter film flows in our everyday life as drops, bubbles, pearls, and waves [1], in our bodies as tear film [2], in nature as avalanches [3], and in moving glaciers [4] as well as in biotechnological applications like biofilm growth [5] to name a few prominent examples. Moreover, film flows play an important role in engineering-technical applications like heat transfer [6] and coating [7, 8], where also boundary effects caused by sidewalls are of particular interest [9]. For the sake of optimizing these processes, a sound understanding of the physics of gravity-driven films is needed.

In this introductory Chapter 1, the large body of precedent papers on the effects of topography and inertia on gravity-driven film flows is summarized and discussed – beginning with the creeping flow and going up to the stability of the flow over topography. Fingering and spreading, non-Newtonian fluids, heated boundaries, porous media, multilayer systems, and surfactants are excluded, i.e. considered only in the limits of the main topic. Gravity is the only driving force considered, centrifugal and electromagnetic forces are left aside. With one exception, the author refrains from discussing film flows over flat inclines without sidewalls, as their dynamics was frequently reviewed, e.g., in the References [10–12]. The exception is the seminal work of Wilhelm Nusselt [13], including its stability, which opened up this field of research. Nusselt unveiled that a steady-state water flow down a flat incline features a parabolic velocity profile. However, in technical and experimental systems a steady-state Nusselt flow is not always present. An overview on how the interplay of bounding topography and inertia affects gravity-driven films will be given in this introductory Chapter 1, which relies on the publication *"Films over topography: from creeping flow to linear stability, theory, and experiments, a review"* from Aksel and Schörner [14].

To acknowledge the original papers, the author sticks to their nomenclatures in the present Chapter 1 with the exception of the dimensionality of the substrate, which was not defined uniformly in the literature. The substrates are denoted as one- or two-dimensional according to the number of independent variables defining their geometry. The flow over one-dimensional topography is usually considered as two-dimensional, though its potential instability may lead to three-dimensional patterns. On the contrary, the flow over two-dimensional topography is inherently three-dimensional.

1.1. Creeping film flow and films in lubrication approximation

The lubrication approximation is based on the asymptotic reduction of the governing equations and boundary conditions to a simplified system which often consists of a single nonlinear partial differential equation formulated in terms of the local thickness of the film [10]. The unknown fluid velocity and the pressure are then determined via functionals of the solution of that differential equation [10]. Formally, the lubrication approximation fails precisely at sharp boundaries and must be replaced by the Stokes equation for creeping films, there [12]. For

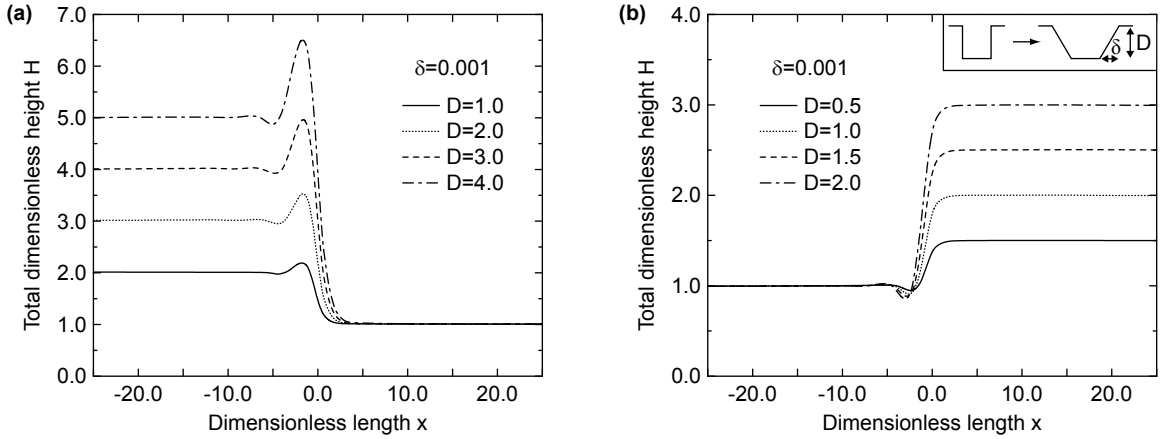

Figure 1.1.: Free surface profiles $H(x) = h(x) + S(x)$ for the step-down (a) and the step-up (b) for the wall steepness $\delta = 0.001$ and different depths D. Note the presence of the capillary ridge right before the entrance to the step-down and the capillary depression region right before the step-up. Their height increases as D increases. The dimensionless length in streamwise direction is $x = x^\star/l$, the capillary scale is $l = h_0/Ca^{1/3}$, the dimensionless local film thickness is $h(x) = h^\star(x)/h_0$, the capillary number is $Ca = \mu U/\sigma$, the characteristic velocity is $U = \rho g \sin\alpha h_0^2/\mu$, the film thickness far from the feature is h_0, the dimensionless topography shape is $S = S^\star/h_0$, the dimensionless wall steepness is $\delta = \delta^\star/l$, and the dimensionless step depth is $D = D^\star/l$. The respective dimensional quantities are indicated by stars ($\star$). The fluid parameters are the density ρ, the dynamic viscosity μ and the surface tension σ. Modified and reprinted with permission from Kalliadasis *et al.* [16]. © AIP Publishing.

further details on the lubrication approximation and creeping flow conditions, please see Spurk and Aksel [15]. For convenience, creeping film flow and films in lubrication approximation are considered together in the following.

1.1.1. Two-dimensional flow

Kalliadasis *et al.* [16, 17] used the lubrication theory to study the flow of a thin film over a trench, as an example of a one-dimensional localized topographical feature. They found that the dynamics of the film is governed by the depth, the width, and the steepness of the obstacle. They showed that the free surface developed a ridge right before a step-down (Figure 1.1a) and a depression region right before a step-up (Figure 1.1b) with the minimum film thickness always being located near the concave corner of the profile. Moreover, they identified the capillary ridge to be a manifestation of the effect of the capillary pressure gradient induced by the substrate curvature. The numerical work by Mazouchi and Homsy [18] showed that the magnitude and location of the ridge and the depletion region depended on the capillary number and the step depth. The effect of capillarity and inclination angle on a film flow over an inclined plane with an edge was studied analytically, numerically and experimentally by Aksel [19]. He showed that capillary forces cause the free surface to develop a ridge before a downwards edge. In particular, he studied the region of influence of the capillarity in dependence of the inclination angle. This paper gave rise to an inverse problem in Heining *et al.* [20]. Gaskell *et al.* [21] considered thin film flow over one- and two-dimensional (see Section 1.1.2) localized topographies by means of finite element solutions of the Navier-Stokes equations and multigrid finite difference predictions. In the one-dimensional case, Stokes solutions for the flow over a wide trench were shown to be in excellent agreement with those of Mazouchi and Homsy [18], and Navier-Stokes solutions revealed that the effect of increasing Reynolds number is to increase the amplitude of the 'bow wave.' The effects of inertia will be studied in Section 1.2.

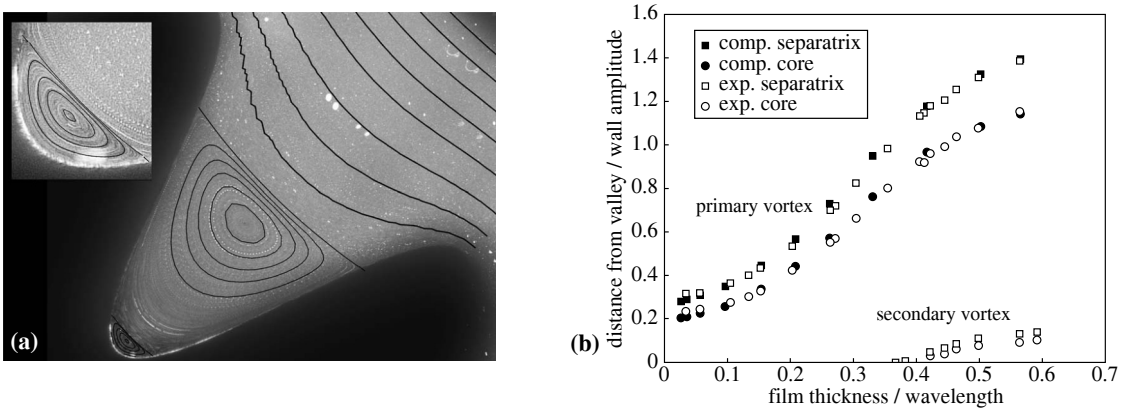

Figure 1.2.: (a) Primary and secondary vortex of a film flow with waviness $a = 9\pi/10 \approx 2.83$, mean film thickness $h = 0.89$, inclination angle $\alpha = 45°$ and capillary number $Ca = 1.6$. The waviness is $a = 2\pi A/\lambda$, the dimensional topography amplitude is A, the dimensional topography wavelength is λ, the capillary number is $Ca = \eta U/\sigma$, the characteristic velocity is $U = \rho g \lambda^2 \sin\alpha/(8\pi^2\eta)$, the dimensional mean film thickness is H, the dimensionless mean film thickness is $h = 2\pi H/\lambda$. The fluid parameters are the density ρ, the dynamic viscosity η and the surface tension σ. Reprinted with permission from Scholle *et al.* [23]. © Springer Nature. (b) Size of the primary and the secondary vortex as a function of the film thickness and the peak-peak amplitude of the free surface. The distances of the vortex core and of the separatrix to the center of the trough are shown as circles and squares, respectively. Computations [27] are represented by filled symbols, experiments [26] by open symbols. The experimental data of the secondary vortex were added from [26]. Modified and reprinted with permission from Nguyen and Bontozoglou [27]. © AIP Publishing.

Wang [22] analytically studied a liquid film flowing slowly down a wavy incline. He found that the amplitude and phase shift of the free surface depend, in a complicated manner, on the surface tension and the wavelength and orientation of the wavy striations. The mean film thickness was found to increase hand in hand with the waviness of the topography and, hence, was larger than the corresponding Nusselt film thickness [23]. The idea that eddies generated in the valleys of riblets act like fluidic roller bearings was considered by Scholle *et al.* [24] with the method of holomorphy, previously demonstrated in [23]. They discussed the resulting film elevation and reported that the presence of fluidic roller bearings may cause a small drag reduction and improve material transport in creeping films.

Besides the free surface, periodic topographies also change the velocity field of a film flow. For the free surface Stokes flow of a liquid film along an undulated incline, Pozrikidis [25] presented an extensive parametric study for the case of sinusoidal topography. The effects of substrate amplitude, inclination angle, flow rate, and surface tension were considered. Using integral boundary method he reported on flow reversal in the troughs of different sinusoidal undulations which appears when a sufficiently thick film flows over steep topographies. Experiments by Wierschem *et al.* [26], the analytical approach by Scholle *et al.* [23] and numerics by Nguyen and Bontozoglou [27] focused on this flow reversal in creeping films over strongly undulated, harmonic bottom profiles. The References [23, 26, 27] show that the radius of curvature of the crests and the film thickness are the decisive parameters for the creation and the evolution of the vortices in the troughs. Multiple eddies were reported to form if the crests were sufficiently deep and sharp [23] (see Figure 1.2). In films over undulated substrates the minimum radius of curvature determines the size of the smallest eddy. The depth of the crests, their radius of curvature, and the film thickness are finite and constitute characteristic lengths of the flow problem. This limits the number of the kinematically induced eddies appearing in free surface flows over topographies to a finite number as it prohibits similarity solutions. Hence, the eddies appearing in films over topography are similar to but not identical with Moffatt eddies [28].

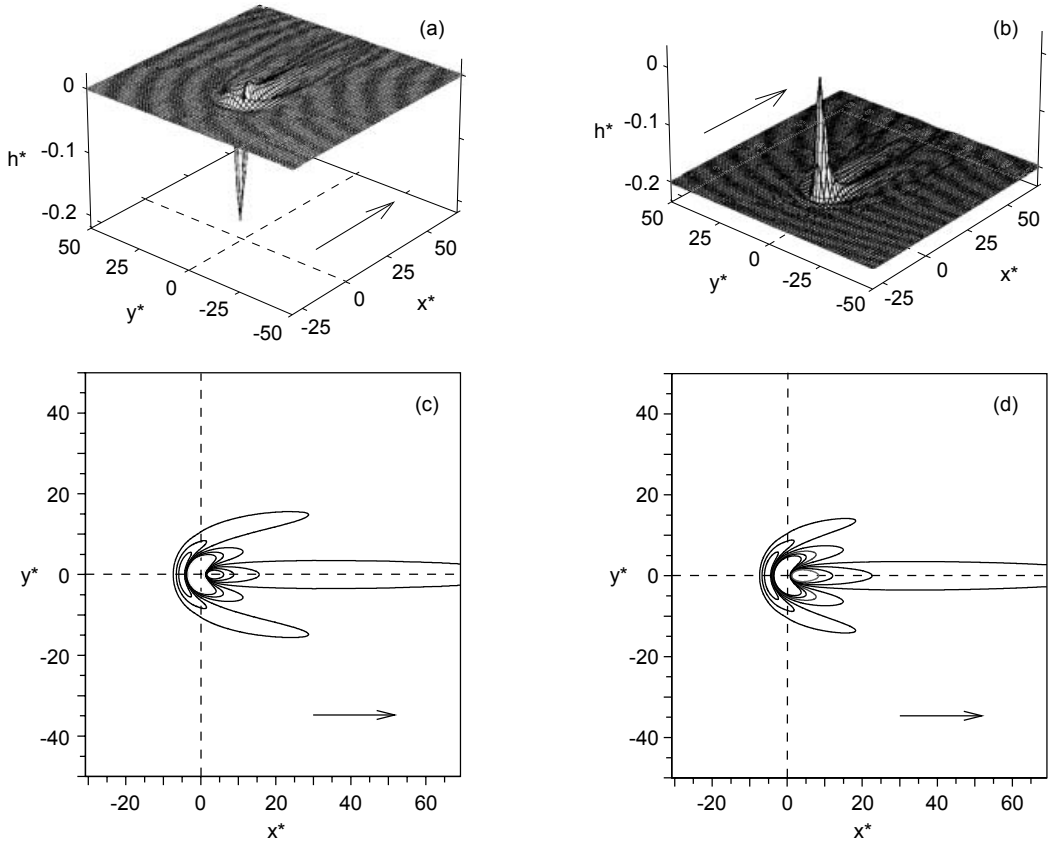

Figure 1.3.: Flow of a thin water film over square topographies with $w = 1.54$, $A = 1$, and $|s_0| = 0.25$. In the three-dimensional views, the flow is from bottom-left to top-right: (a) trench; (b) peak. In the contour plots, the flow is from left to right and the contours show the free surface height. Contour values are chosen to be equal in magnitude but opposite in sign: (c) trench; (d) peak. The crossed dashed lines indicate the center of the topography and the arrow indicates the direction of the flow. The dimensional topography parameters are the streamwise length L_T in X-direction, the span width W_T in Y-direction, the amplitude S_0 in Z-direction ($S_0 > 0$: protrusion; $S_0 < 0$: depression) and the form $S(X, Y)$. The dimensional trench amplitude is $s_0 = S_0/H_0$ with $H_0 = [3\mu Q_0/(\rho g \sin\theta)]^{1/3}$ being the dimensional film thickness of the fully developed undisturbed flow of the flux Q_0. The dimensionless velocity in z-direction is $w = W/(\epsilon U_0)$ with $\epsilon = H_0/L_0$, $U_0 = 3Q_0/(2H_0)$ being the dimensional surface velocity of the fully developed film, $L_0 = H_0/(6Ca)^{1/3}$ being the characteristic in-plane length scale, $Ca = \mu U_0/\sigma$ being the capillary number and W being the dimensional velocity in z-direction. The aspect ratio of the topography is $A = w_t/l_t$. The non-dimensional coordinates are $(x, y) = (X, Y)/L_0$. The coordinate system $(x^\star, y^\star)$ has its origin at the center of the topography (x_t, y_t) with $(x^\star, y^\star) = (x - x_t, y - y_t)$ such that $h^\star(x^\star, y^\star) = [h(x^\star, y^\star) + s(x^\star, y^\star) - 1]/s_0$. The dimensionless shape of the topography is $s(x, y) = S(X, Y)/H_0$. The fluid parameters are the density ρ, the dynamic viscosity μ and the surface tension σ. Modified and reprinted with permission from Gaskell *et al.* [21]. © Cambridge University Press. Please compare to Figure 1.14 for the effect of inertia.

1.1.2. Three-dimensional flow

Pozrikidis and Thoroddsen [29] studied three-dimensional film flow down an inclined plane over a particle in the asymptotic limit where the size of the obstacle is much smaller than the film thickness. Using Green's function and boundary-integral method for Stokes flow they demonstrated that the presence of a moderated-sized two-dimensional localized topography caused a marked deformation of the free surface upstream right before the obstacle, and a surface response resembling to a surface wake downstream right behind it. The geometry of the particle, the surface tension, and the inclination of the wall were found to be decisive for

the deflection of the free surface. The contribution of Hayes *et al.* [30] can be regarded as an extension of the work of Pozrikidis and Thoroddsen [29] though their approach is different in that from the outset they use a thin film approach to derive a lubrication approximation specialized for the case of a viscous liquid flowing over a small topography. They developed a Green's function for the linearized problem and the solutions so obtained could be used to analyze the effect of an arbitrary two-dimensional localized topography (wall defect) on the coating applied to a substrate. Blyth and Pozrikidis [31] considered the low Reynolds number flow of a liquid film down an inclined plane over a particle attached to the wall. Results were presented for small particles following the earlier asymptotic analysis of Pozrikidis and Thoroddsen [29], and for moderate-sized particles of different shapes. Their simulations revealed that the free surface caused an upstream hump and a horseshoe type of deformation downstream, whose intensity depended on the Bond number and was largely insensitive to the specific shape of the particle.

Gaskell *et al.* [21] analyzed thin film flow over both one-dimensional (Section 1.1.1) and two-dimensional localized topographies within the framework of the lubrication approximation, where accurate numerical solution of the governing nonlinear equations was achieved using an efficient multigrid solver. Their discussion of three-dimensional flow focused mainly on the flow over a square trench (Figure 1.3a) or peak (Figure 1.3b). Particular thought was given to the 'bow wave' and to the cause of the 'downstream surge,' which was not present in the flow over the corresponding one-dimensional topographies. Baxter *et al.* [32] studied three-dimensional gravity-driven thin film flow over and around an obstacle on an inclined plane. They reproduced previously published flow profiles for asymptotically small obstacles [29] and extended the small free surface deflection assumption [31] to larger obstacles – either fully submerged or exhibiting a contact line. Cylinders and hemispheres were considered. The curvature of the free surface was calculated using both finite difference approximations and Hermitian radial basis function interpolations. The resulting solutions were compared to each other. All free surface profiles indicated an upstream peak, followed by a depression downstream of the obstacle with the peak decaying in a horseshoe deformation. The flow profiles were mainly governed by the inclination, the Bond number, the obstacle geometry, and, for not fully submerged obstacles, the contact angle.

Lee *et al.* [33] modeled the gravity-driven continuous thin film flow over a plane, containing well-defined single and grouped topographical features. They showed that for the accurate solution of the associated lubrication equations, adaptive local mesh refinement and multigriding offers increased flexibility together with a significant reduction in memory requirement. Automatic grid refinement effectively restricted the use of fine grids to regions of rapid flow development, e.g., the upstream capillary ridge, the downstream surge region, and the characteristic bow wave. Sellier *et al.* [34] compared finite element method (FEM) and adaptive local mesh refinement and multigriding for the flow of a liquid film, only several microns in thickness, over an inclined plane. Although the adaptive multigrid approach was clearly found to be the most efficient, with the two sets of solutions indistinguishable, FEM was found to offer an attractive alternative to the non-specialist user. Both methods revealed that occlusions lead to many of the features inherent in the flow of thin liquid films over fully submerged microscale topographical features; namely, the presence of capillary ridges linked to 'bow wave' plus 'comet-tail' free surface disturbances. The benefits of using a general Newton globally convergent flow solver within a flexible and adaptive multigrid framework for solving the increasingly complex system and number of equations that arise when thin film and droplet flows are subjected to additional physical effects was addressed by Lee *et al.* [35]. Its advantages were demonstrated by solving

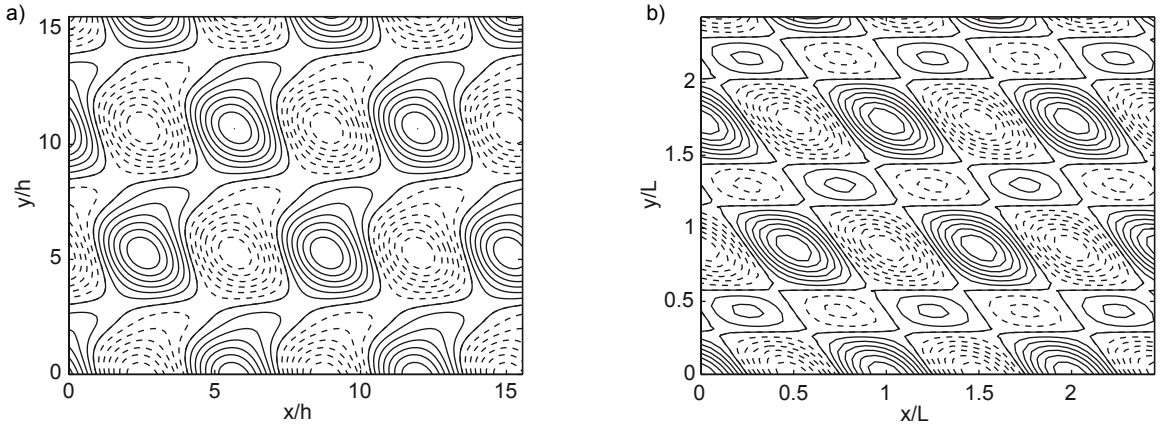

Figure 1.4.: The free surface (a) for flow over wall topography (b) with hexagonal pattern. Positive levels are shown as solid lines, negative levels are shown as dashed lines. The side length of the hexagonal lattice is L and h is the mean film thickness. It is $2\pi h/L = 1$, the capillary number is $Ca = \mu U/\gamma_0 = \sqrt{2}/4$ and the inclination is $\pi/4$. The unperturbed surface velocity along the x-axis is U, the dynamic viscosity of the fluid is μ, its surface tension γ_0. Modified and reprinted with permission from Luo and Pozrikidis [37]. © Springer Nature.

two three-dimensional, gravity-driven free surface flows, involving the mixing of solute species on rigid and flexible substrates and droplet flow past an occlusion. Using the same technique, Lee *et al.* [36] explored the dynamics of thin film flow over flexible substrates and demonstrated how substrate flexibility affects the practical issue of free surface planarization.

Luo and Pozrikidis [37] studied the effect of small-amplitude doubly periodic wall corrugations on gravity-driven film flow down an inclined plane using a perturbation analysis for Stokes flow. They observed that the shape of the free surface deviates significantly from that of the wall. Figure 1.4 illustrates one of the topographies considered and the contours of the free surface of the corresponding flow. Beyond, their results showed that two-dimensional corrugations reduce the surface deformation by increasing the effective wave numbers and reducing the effective capillarity, compared to their one-dimensional counterparts.

1.2. Inertial flow

1.2.1. Two-dimensional flow

The transition from creeping flow to inertial flow was studied numerically by Bontozoglou and Serifi [38] for film flows along a vertical substrate with isolated, deep step changes, i.e., step-downs and step-ups. They showed that the capillary ridge before a step-down and the capillary depression before a step-up change their streamwise length scale in the presence of inertia. The way of change was directly predicted from an order-of-magnitude balance of gravity, capillary, and inertia forces. The height of the capillary features was found to first grow with the Reynolds number (Figure 1.5a), but eventually diminish when inertial forces overpower capillary forces (Figure 1.5b). Downstream of a step-up, an inertial ridge appeared at the free surface with increasing Reynolds number (Figure 1.5c). The inertial ridge was attributed to a liquid overshoot in the horizontal direction, and its height was shown to be restrained by capillary forces at low Reynolds numbers and by inertial forces (a low-pressure region appears) at high Reynolds numbers.

Wierschem *et al.* [39] studied the flow of a liquid down an incline with weak sinusoidal undula-

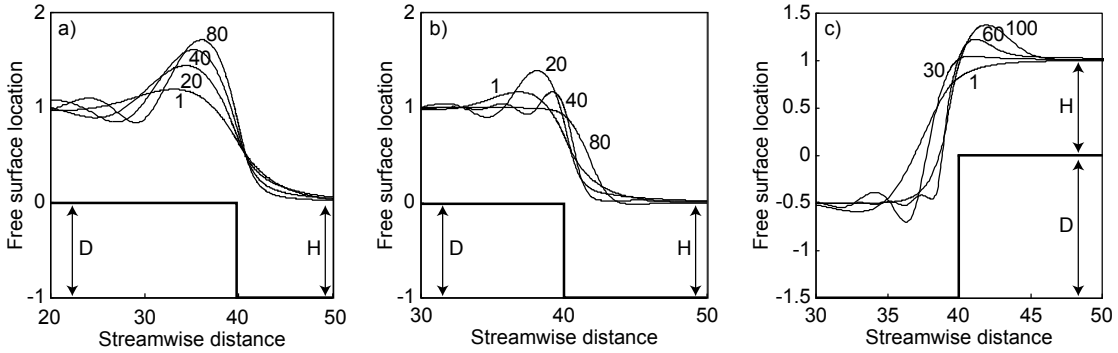

Figure 1.5.: The free surface profiles in the vicinity of a step-down with $D/H = 1$, for $Re = 1, 20, 40, 80$ and (a) $Ca = 0.01$, (b) $Ca = 0.075$ and for a step-up (c) with $D/H = 1.5$, $Ca = 0.075$ and $Re = 1, 30, 60, 100$. The Reynolds number is $Re = Q/\nu$ with Q being the volumetric flow rate per unit span. The capillary number is $Ca = 3\mu U/\sigma$ with the mean velocity $U = Q/H = gH^2/3\nu$, the film thickness $H = (3\nu Q/g)^{1/3}$ and gravity g. The fluid parameters are the dynamic viscosity μ, the density ρ, the kinematic viscosity $\nu = \mu/\rho$ and the surface tension σ. Modified and reprinted with permission from Bontozoglou and Serifi [38]. © Elsevier.

tions. They showed how wavy bottom variations, which are long compared to the film thickness or the corrugation amplitude, modify the flow with respect to that down a flat incline. The effects of waviness, inclination angle, film thickness, and Reynolds number were considered using different perturbation analyses. They compared these asymptotic results to measured velocity profiles and film thicknesses. That way, they revealed the influence of inertia on the surface shape and the deviation from the parabolic Nusselt profile. Subsequently, Wierschem and Aksel [40] carried out experiments on the influence of inertia on the eddies that form in gravity-driven films creeping over strongly sinusoidally undulated substrates. They found that in the laminar regime the eddies became tilted as inertia became significant and that their size increased as a function of the Froude number. Inertia-induced surface waves provoked an oscillation and a breakup of the separatrix by the turnstile-lobe mechanism. This material exchange between the eddy and the overlying film is still an open question. Scholle *et al.* [41] extended previous work on the formation of eddies in creeping [26] (see Section 1.1.1) and inertial [40] flow of gravity-driven films over sinusoidal undulations. They solved the governing equations semi-analytically using a complex variable method for Stokes flow and numerically via a full finite element formulation for the more general problem when inertia is dominant. The effect of varying geometry (involving changes in the film thickness or the amplitude and wavelength of the substrate) and inertia was explored separately. Persistent eddies, which existed even for vanishingly thin films, occurred for sufficiently steep inclinations and corrugations. Moreover, they showed that the formation and presence of eddies can be manipulated in one of two ways. A decrease/increase in the corrugation steepness led to the disappearance/appearance of kinematically induced eddies (see creeping flows in Section 1.1.1). An increase/decrease in inertia led to the appearance/disappearance of inertially induced eddies due to boundary-layer separation (please see Figure 1.6). Beyond, they defined a critical corrugation steepness for a given film thickness, demarking the transition from a kinematically to an inertially induced local eddy flow structure and vice versa.

The inviscid free surface flow over a wavy substrate was analyzed by Bontozoglou *et al.* [42] with a numerical method, based on the hodograph formulation (devised by Stokes in 1880). They were the first to demonstrate that a series of resonances is possible between the substrate undulations and the free surface. The steady, free surface profiles were calculated for a

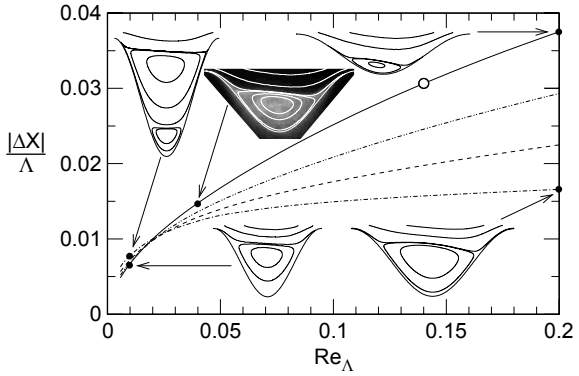

Figure 1.6.: Effect of the local Reynolds number Re_Λ on the horizontal shift of the eddy center, $|\Delta X|/\Lambda$ for $Re_H = 228$ and inclination $\alpha = 45°$. The inlaid streamline plots illustrate the local flow structure for parameter values corresponding to the points shown as black circles. The inlaid experimentally observed flow was taken from [26]. The open circle marks the transition from a kinematically to an inertially induced eddy. The length ΔX is taken as a measure of flow asymmetry and represents the horizontal shift of an eddy center relative to the same centerline and hence the Stokes solution. The global Reynolds number is $Re_H = \rho^2 g H^3 \sin\alpha/(2\eta^2)$, with H being the corresponding Nusselt film thickness. For the flow structures in the vicinity of the substrate, the local Reynolds number is $Re_\Lambda = \rho^2 g \Lambda^3 \sin\alpha/(16\pi^3\eta^2)$ with the topography wavelength Λ. The gravitational acceleration is g. The fluid parameters are the dynamic viscosity η and the density ρ. Reprinted with permission from Scholle *et al.* [41]. © AIP Publishing.

wide range of undulation amplitudes and current velocities and were shown to be significantly dimpled by higher harmonics. The flow field indicated that the free surface shape strongly affects the velocities close to the substrate, leading to distributions which change dramatically with current velocity. Some implications on the phenomena of wall dissolution or material deposition, Bragg scattering of surface waves, and sediment transport in rivers were discussed as well. The subsequent numerical work by Bontozoglou and Papapolymerou [43] considered viscous, laminar film flow down an inclined plane with sinusoidal corrugations. They examined the free surface amplitude and phase shift relative to the underlying topography. In a range of Reynolds numbers, a resonance phenomenon was calculated, leading to an amplification of the free surface amplitude. Trifonov [44] investigated viscous film flow down a vertical, harmonic substrate based on both Navier-Stokes and integral equations. He performed calculations over a wide range of Reynolds numbers and geometry characteristics of the substrate, taking into account viscosity, inertia, and surface tension and unveiled resonance of the free surface with the undulated bottom. Two qualitatively different regions in flow behavior were distinguished within the studied range of Reynolds numbers. In the region of moderate Reynolds numbers, the flow was found to be controlled significantly by the forces of surface tension, and in the region of large Reynolds numbers by inertial forces. The comparison between the results obtained on the basis of the integral model and the Navier-Stokes equations demonstrated that the integral approach is correct in the area where the flow is defined mainly by surface tension forces. Bontozoglou [45] extended the previous papers [42, 43] to large-amplitude sinusoidal corrugations by using a spectral spatial discretization method involving Fourier modes in the streamwise direction and Chebyshev polynomials across the film. Free surface profile and flow structure were studied as a function of the Reynolds number and the topography amplitude. The minimum corrugation height for flow separation to occur was found to generally decrease with the Reynolds number, but to attain larger values around the resonance conditions. Besides, the distribution of the shear stress along the substrate and of the normal velocity gradient close to the free surface was computed and related to heat and mass transport.

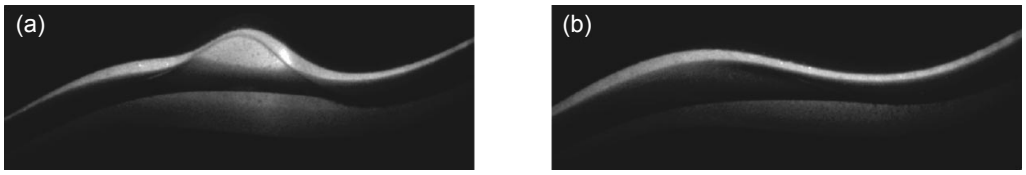

Figure 1.7.: Side views of resonant standing waves. (a) Hump at the flat side of the bottom undulation ($h = 13.6$ mm, $Re = 62$). (b) Standing wave without a hump ($h = 14.7$ mm, $Re = 79$). The flow is from right to left. The inclination angle is $\alpha = 11.9^\circ$ and $Re = U_s h/\nu$ denotes the Reynolds number with the surface velocity U_s and the film thickness h of the Nusselt solution. The kinematic viscosity of the fluid is ν. Reprinted with permission from Wierschem and Aksel [46]. © AIP Publishing.

Wierschem and Aksel [46] experimentally studied the flow of a viscous liquid down an inclined channel with a sinusoidal bottom profile of moderate waviness. At low inclination angles, basins appeared and, at the inflow of the basins, stationary hydraulic jumps formed as shock fronts and surface rollers. A bistable region in which both jump phenomena exist depending on the flow history was identified. The critical Froude numbers that confine the bistable branch were found to depend on the inclination angle. At the low end of the bistable region, an instationary regime of a shock with a fingering-like lateral modulation appeared. The bistability could be traced back to that of a shock front with and without fingers. All experiments [46] indicated that surface tension is important for the existence of the bistability. In thicker films, the surface rollers were suppressed and standing gravity waves appeared, generated by resonant interaction with the bottom undulation (Figure 1.7). At the rising edge of the resonance curves, humps that were apparently due to a nonlinear resonance with the bottom contour were observed. In a small regime of inclination angles, the humps and shocks were bistable. At the transition between the surface rollers and the standing waves, a small region of periodic switching was identified. Figure 1.8 shows an overview over the different flow regimes.

Nguyen and Bontozoglou [27] investigated steady flow of liquid films along sinusoidal, steeply corrugated inclines by finite element simulation of the Navier-Stokes equations. They unveiled resonant interaction between the wall and the free surface and used the resonance maximum to

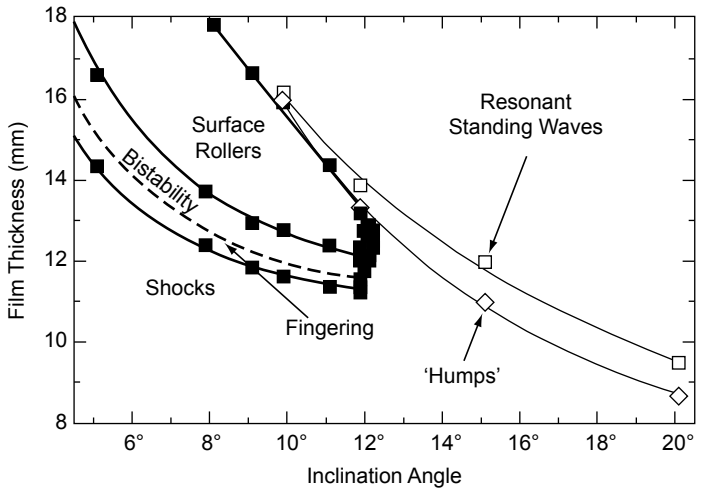

Figure 1.8.: Overview over the different flow regimes as a function of film thickness and inclination angle. The open squares and diamonds indicate the maximum of the first and second Fourier mode of the standing wave, respectively. Modified and reprinted with permission from Wierschem and Aksel [46]. © AIP Publishing.

define a critical Reynolds number which separates the flow into two regimes. Steep corrugations triggered extensive flow separation in both regimes. However, the separation characteristics – most notably the limiting behavior for very thin and very thick films – varied because of the different significance of the capillary forces in the two regimes. Wierschem *et al.* [47] demonstrated linear resonance in viscous films on inclined wavy planes and identified different behaviors for thin, intermediate and thick films. They applied a method previously used by Anshus and Goren [48] for getting approximate solutions to the Orr-Sommerfeld equation for the flow on a vertical substrate. In line with Anshus and Goren [48], Wierschem *et al.* [47] replaced the velocity, usually a function of the distance from the bottom, by its value at the free surface while the second derivative of the velocity is kept at its true value. These results supported the view that the resonance phenomenon is associated with an interaction of the undulated film with capillary-gravity waves traveling against the main flow direction. The resonance peak is attained under conditions that render the wave phase velocity equal to zero in the laboratory reference frame and thus permit direct exchange of energy between the steadily deformed film and the free surface. The subsequent work of Heining *et al.* [49] studied nonlinear resonance in viscous gravity-driven films flowing over sinusoidally undulated substrates. Numerically, they solved the full, steady Navier-Stokes equations to follow the emergence of the first few free surface harmonics with increasing corrugation amplitude, and to study their parametric dependence on film thickness, inertia, and capillarity. They documented that, with increasing dimensionless corrugation amplitude, higher harmonics were generated on the free surface and the resonance becomes bistable. Analytically, they applied the integral boundary-layer method and derived an asymptotic equation valid for rather thin films. The analysis revealed that higher harmonics were generated by the nonlinear coupling of the topography with lower-order harmonics of the free surface. Furthermore, their asymptotic analysis has also accounted for bistable resonance in flows over steep bottom undulations. They showed that the solution of a minimum model retaining the essential nonlinearities responsible for bistability is similar to that of the driven nonlinear Duffing oscillator [50].

Numerics by Malamataris and Bontozoglou [51] considered viscous film flow down an inclined plane with periodic but not harmonic corrugations using finite element method. The dimensionless Navier-Stokes equations were solved in the whole range of the laminar flow regime and the results were compared with available experimental data for very low Reynolds numbers. Particular emphasis was given to free surface profiles, streamlines, velocity, and pressure distributions along the free surface and the substrate. The free surface shape was found to be mainly influenced by the capillary number, its phase shift relative to the substrate undulations by the Reynolds number. Resonance of the free surface with the undulated bottom appeared at high Reynolds numbers and the amplification factor was found to decrease with the corrugation amplitude. Besides, criteria for flow reversal in the troughs were established. The gravity-driven film flow along a substrate with rectangular periodical corrugations was studied numerically by Pak and Hu [52]. They used the volume of fluid method to show that the phase shift between the free surface and the underlying topography increases with the Reynolds number. Deeper corrugations or smaller inclination angles raised the resonant Reynolds number. Moreover, they calculated the streamlines and reported on vortical structures in the steady flows, either produced by the interaction between capillary wrinkling and inertia, or by the rectangular geometry. The vortices were closely related to the deformation of the free surface and appeared either only in the troughs, or simultaneously in the troughs and on the crests (see Figure 1.9). Vlachogiannis and Bontozoglou [53] performed experiments on the structure of gravity-driven film flow along an inclined periodic substrate with rectangular corrugations.

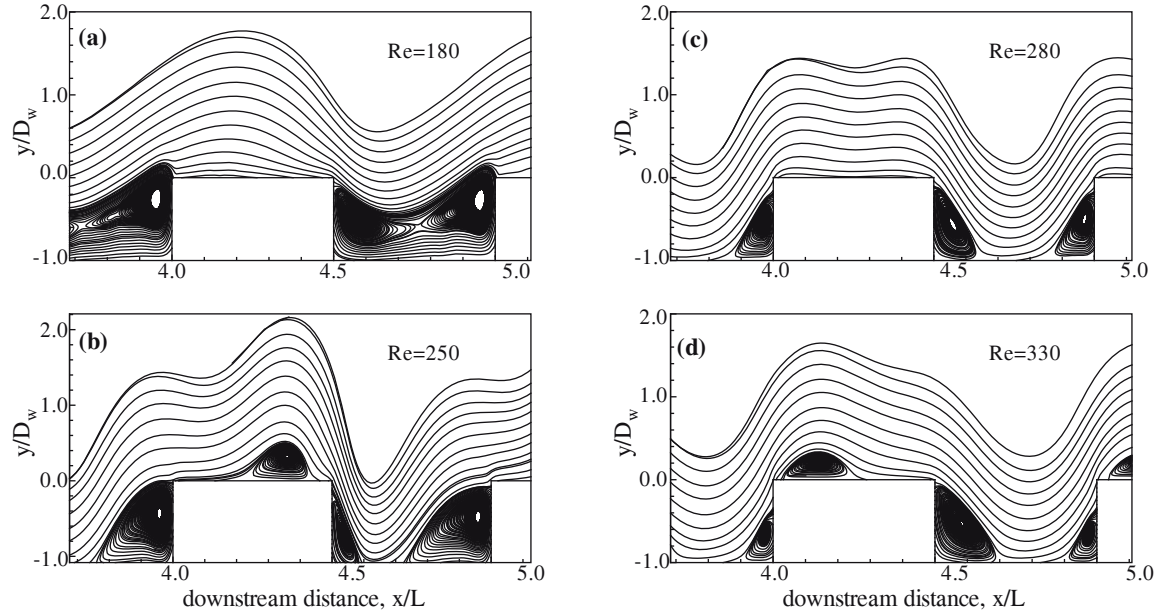

Figure 1.9.: Effects of inertia on the local flow structure for the relative wall depth $\zeta = D_w/h_N = 0.8$ and inclination $\varphi = 5.4°$. (a) $Re = 180$, (b) $Re = 250$, (c) $Re = 280$ and (d) $Re = 330$. The depth of the corrugated wall is D_w, the Nusselt film thickness is h_N, the Reynolds number is $Re = u_n h_N/\nu_l$, the mean Nusselt velocity in x-direction is u_N, the kinematic viscosity of the liquid is ν_l. Modified and reprinted with permission from Pak and Hu [52]. © Elsevier.

They used a fluorescence imaging method to capture the evolution of film height in space and time. Please see Section 1.4.2 for the time-dependent results. The steady flow was found to exhibit a statically deformed free surface with the same wavelength as the bottom. Its properties, i.e. the amplitude, phase, and harmonic content, were correlated with the Reynolds and Kapitza number. They interpreted their measurement in terms of the resonant interaction between the substrate and the free surface proposed by Bontozoglou and Papapolymerou [43]. The gravity-driven film flow along an inclined periodic substrate with rectangular corrugations was considered experimentally by Argyriadi *et al.* [54]. They studied the effect of corrugation steepness on two-dimensional steady flow, three-dimensional steady flow (Section 1.2.2) and traveling surface waves (Section 1.4). The steady inertial flow over the undulations led to a static deformation of the free surface (Figure 1.10a), which had the same wavelength as the wall, and was interpreted in terms of a resonant interaction [43] with maximum deformation at a peak Reynolds number (Figure 1.10b, 1.10c).

Trifonov [44], Wierschem *et al.* [55], and Pak and Hu [52] reported on a coupling of the velocity field and the free surface in films over inclined periodical structures, namely the suppression of eddies. Trifonov [44] investigated viscous film flow down a vertical, harmonic substrate based on both Navier-Stokes and integral equations. He found stagnation zones and studied their transformation with increasing Reynolds number (Figure 1.11). Stagnation zones appeared at both small and large Reynolds numbers. At intermediate Reynolds numbers, an eddy-free window was found. This eddy suppression was considered in detail by the subsequent work of Wierschem *et al.* [55]. They studied inertial film flow down a sinusoidally undulated incline in both experiments and numerics. With increasing Reynolds number, eddies were found to form in the troughs of the bottom undulation (Figure 1.12a, 1.12b). A further increase of the Reynolds number led to a diminution of the eddies until they vanished completely (Figure 1.12c). At even higher Reynolds numbers, they reappeared yielding an eddy-free window of

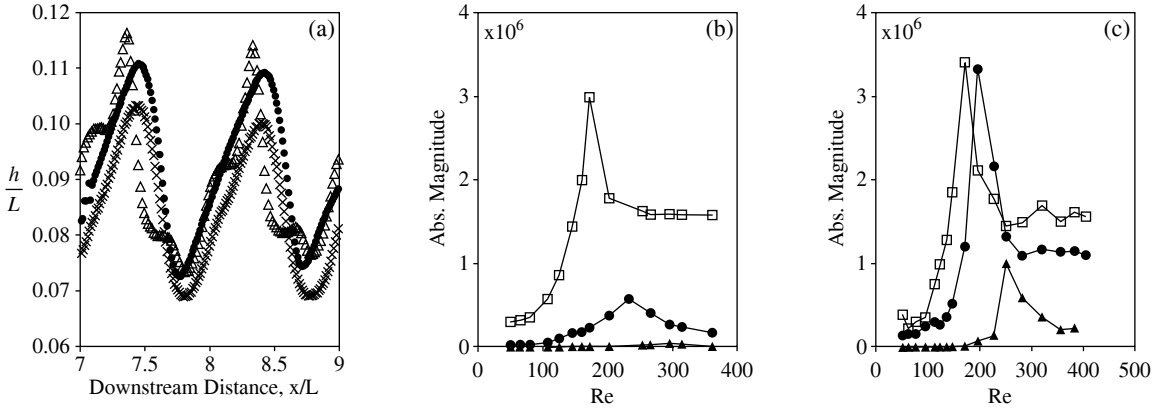

Figure 1.10.: (a) The statically deformed free surface, h/L, at Reynolds number $Re = 315$ and inclination angle $\varphi = 3.4°$, for wall steepness $B/L = 1/60$ (crosses), 1/30 (circles), and 1/15 (triangles). The first curve has been displaced from its true mean elevation for clarity. (b) The amplitude of the first (squares), the second (circles) and the third (triangles) harmonics of the free surface profile as a function of Re for $\varphi = 3.4°$ and wall steepness $B/L = 1/30$. (c) Same as (b) for wall steepness 1/15. The mean film thickness is h. The wavelength of the rectangular corrugations is L, their amplitude is B. The Reynolds number is defined as $Re = q/\nu$, with q being the volumetric flow rate per unit width and ν being the kinematic viscosity of the fluid. Modified and reprinted with permission from Argyriadi *et al.* [54]. © AIP Publishing.

Reynolds numbers (Figure 1.12d). Within this window, the free surface shape changed abruptly. The change came along with a sudden decrease in the mean film thickness and an abrupt transition of the surface shape type from anharmonic with a strong indentation to harmonic. The anharmonic surface shape showed typical features of a hydraulic jump, which vanished during the transition. The formation of the eddies was found to be suppressed at Reynolds numbers where the first harmonic of the free surface contour was sufficiently strong regardless of the exact surface shape. Hence, they identified eddy suppression to be a consequence of the resonance of the free surface with the substrate undulations. Besides the eddies in the troughs, eddies appearing on the crests of rectangular corrugations can be suppressed as shown by Pak and Hu [52]. In their numerical study, the eddy on the crest first formed when the Reynolds number was increased (Figure 1.9a, 1.9b), then disappeared (Figure 1.9c) and reappeared again at even higher Reynolds numbers (Figure 1.9d). The experimental verification of the appearance and the disappearance of eddies on the crests of rectangular corrugations is still lacking.

An example for the physical significance of the above-mentioned findings is the optimization of liquids flowing over structured packings. This type of technical application was studied, e.g., by Valluri *et al.* [56]. They used integral boundary method with a parabolic velocity profile to investigate films flowing over structured substrates of sinusoidal or doubly sinusoidal shapes which resembled Mellapak® packings. Besides, in coating industry, the homogeneity of a coating is decisive for its quality. In order to improve coating quality Varchanis *et al.* [57] numerically studied the mechanisms leading to different types of air inclusions in the troughs of steeply inclined substrates which featured periodical trenches of rectangular shape.

1.2.2. Three-dimensional flow

Decré and Baret [58] performed experiments on gravity-driven thin viscous films flowing over both one- and two-dimensional non-periodic topographies. Steps, trenches, rectangular and square topographies of different steepness were considered. They measured full two-dimensional

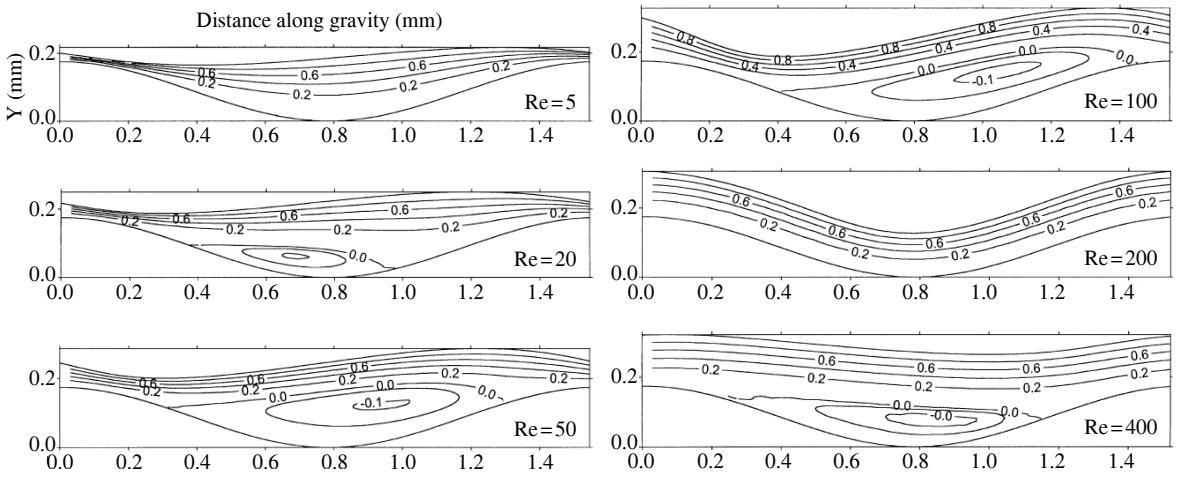

Figure 1.11.: Contour lines of the streamline function. Film flow of a liquid with small viscosity over a corrugated surface with amplitude $A = 0.175\,\text{mm}$ and wavelength $L = 1.57\,\text{mm}$. The Reynolds number is defined as $Re = Q_0/\nu$ with flow rate Q_0 and kinematic viscosity ν. The calculations are based on the Navier-Stokes equations. Modified and reprinted with permission from Trifonov [44]. © Elsevier.

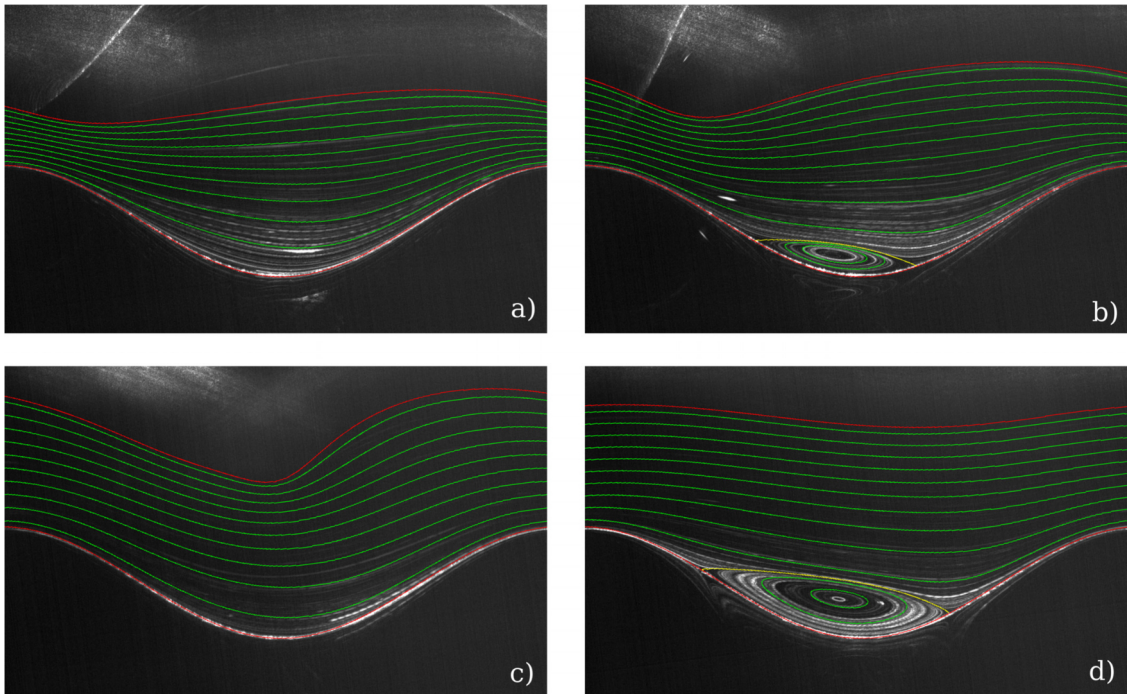

Figure 1.12.: Comparison of experimental pathlines to numerical streamlines. The image is rotated by the inclination of the channel. The volume flux is continuously increased from (a) to (d). (a) $Re = 9$: no eddy at low Reynolds numbers. (b) $Re = 16$: increasing inertia results in the generation of an eddy in the trough of the undulation. (c) $Re = 31$: increasing inertia further, the eddy vanishes. (d) $Re = 48$: flow separation reappears at even higher Reynolds numbers. Bottom contour: lower bright sinusoidal line; lines below and inversely bent lines in the upper part of the pictures are reflections of the pathlines at the bottom and at the free surface. Channel inclination angle: 8°. The Reynolds number is defined as $Re = \dot{q}/\nu$ with flow rate $\dot{q}$ and kinematic viscosity ν. Modified and reprinted with permission from Wierschem *et al.* [55]. © AIP Publishing.

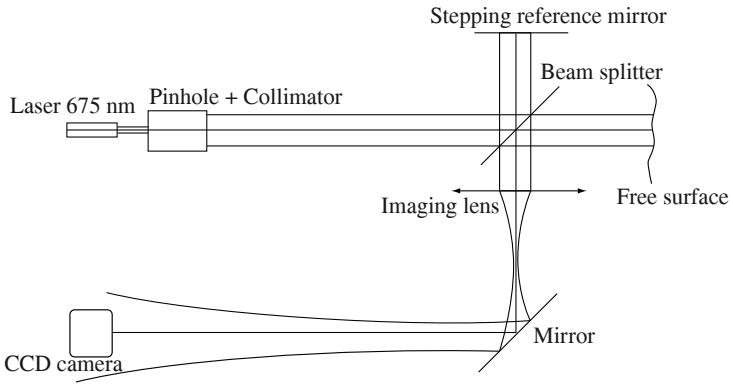

Figure 1.13.: Schematic view of the interferometric setup used by Decré and Baret [58] to map the free surface shape of a three-dimensional film flow over localized two-dimensional topography. Modified and reprinted with permission from Decré and Baret [58]. © Cambridge University Press.

maps of the free surface with phase-stepped interferometry. The interferometric setup is shown in Figure 1.13. For one-dimensional topographies, the local curvature of the substrate caused a standing capillary ridge upstream of the step-down topography, followed by an exponential relaxation downstream of the topography. Also for two-dimensional topographies a capillary ridge arose upstream of the step-down topography, please see the bow-shaped dark region in Figure 1.14. For the two-dimensional topography, the localized pressure peak led to a negative pressure gradient outwards in all directions, instead of along the x-axis only. A spanwise perturbation was created that relaxed very slowly in the wake of the localized topography. Hence, they showed that the disturbances induced by small-scale topography can persist over length scales several orders of magnitude larger than the size of the topographical feature itself, a finding relevant for coating applications. The experimental results by Decré and Baret [58] were in good agreement with existing models for flow over both one-dimensional [16, 17] and two-dimensional [30] topography. The numerical work by Veremieiev *et al.* [59] studied gravity-driven inertial flow of a thin viscous liquid over a trench. The problem was modeled via a depth-averaged form of the Navier-Stokes equations, akin to the integral boundary-layer approximation. The discrete analogue of the resulting set of coupled equations was solved using full approximation storage and multigriding. For two-dimensional localized topography, the free surface disturbance was found to be significantly affected by the presence of inertia. As in the case of spanwise topography, inertia led to an increase in the magnitude of the resulting capillary ridge and trough formation. The effects of inclination angle and topography aspect ratio were similarly explored. In their subsequent work Veremieiev *et al.* [60] considered gravity-driven three-dimensional flow over different types of two-dimensional topographies, i.e. hemisphere and trench. The Navier-Stokes and continuity equations were solved within a finite element framework for the case of surface tension dominated film flow, and a direct parallel multifrontal solver was implemented along with out-of-core storage. That way, they were able to predict the internal flow structure and the corresponding free surface disturbance. Their results fitted well to those obtained by Baxter *et al.* [32] (hemisphere in Stokes flow, see Section 1.1.2) and Decré and Baret [58] (trench).

Argyriadi *et al.* [54] performed experiments on gravity-driven film flows along inclined periodic substrates with transverse, one-dimensional rectangular corrugations of different steepness. Beyond the peak Reynolds number, which corresponded to the maximum of the free surface resonance amplitude of the two-dimensional flow (Section 1.2.1), a three-dimensional surface

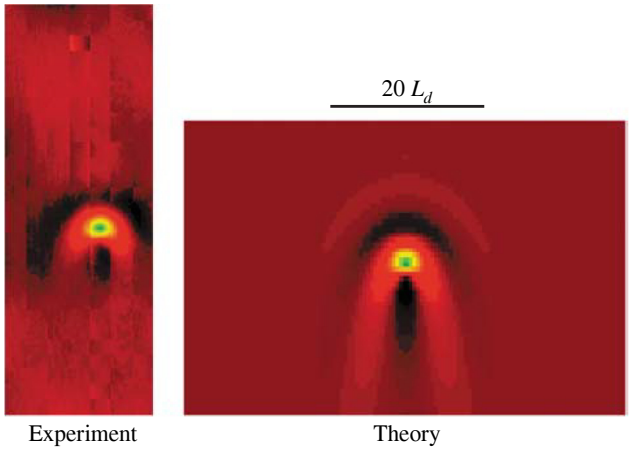

Figure 1.14.: False color representation of the free surface over a square. Comparison between experiment and theory. All scales, lateral and vertical, are the same. Background red: $h_1/T \approx 0$; dark red: $h_1/T > 0$; dark green: $h_1/T < 0$. $w/L_d = 1.54$, $T/h_\infty = 0.25$. The flow is from top to bottom. The trench depth in z-direction is T, and its width in x-direction w. The dynamic capillary length is defined as $L_d = h_\infty/Ca^{1/3} = (\gamma h_\infty/(3\rho g \sin\alpha))^{1/3}$ with h_∞ being the film thickness far away from the topography. The fluid parameters are the surface tension γ and the density ρ. The gravitational acceleration is g, the inclination of the topography against the horizontal is α. Decré and Baret [58] discussed dimensionless perturbation profiles $h_1(x,y)/T = (h(x,y) - h_\infty)/T$ to remove the offset caused by the asymptotic thickness h_∞. Reprinted with permission from Decré and Baret [58]. © Cambridge University Press.

pattern established. This pattern consisted of transverse arrays of depressions along corrugation valleys. Notably the peak Reynolds number and, hence, the onset of the three-dimensional pattern, was insensitive to the steepness of the substrate and appeared at all inclinations tested.

The analytical study by Wang [61] was the first to consider three-dimensional films flowing over two-dimensional doubly periodical sinusoidal undulations in the asymptotic limit of low Reynolds numbers and small waviness. Perturbations on the primary variables and the complex boundary conditions led to a system of successive equations. For undulations of small amplitude, the free surface was found to have a similar structure as the bottom, but with a phase lag and decreased amplitude. Both the free surface and the secondary transverse flow depended on the topography's wavelength and a combined surface tension–inclination parameter. Moreover, he showed that there exists an optimum aspect ratio of protuberances for maximal flow rate. Luo and Pozrikidis [62, 63] studied the effect of inertia on gravity-driven film flow over two-dimensional doubly periodic sinusoidal corrugations for finite Reynolds numbers. Their key idea was to express the substrate's geometry as a Fourier series, and then reconstruct the three-dimensional flow in terms of the individual two-dimensional transverse and unidirectional flows over the constituent oblique corrugations. They found that two-dimensional corrugations may either reduce or amplify the surface deformation with respect to their one-dimensional counterparts. The underlying mechanism was the simultaneous effect of the constituent oblique components on the effective wave number, capillary number, and Reynolds number. The combined analytical, numerical, and experimental approach by Heining *et al.* [64] scrutinized the effect of inertia on gravity-driven free surface flow over different two-dimensional periodic corrugations of sinusoidal shape. At bottom amplitudes which were large compared to the film thickness complex free surface structures appeared, especially in cases where the topography was not fully flooded by the liquid. In any case, a rich variety of pattern formation phenomena and laminar mixing was reported, depending on the interplay between substrate geometry and inertia (Figure 1.15).

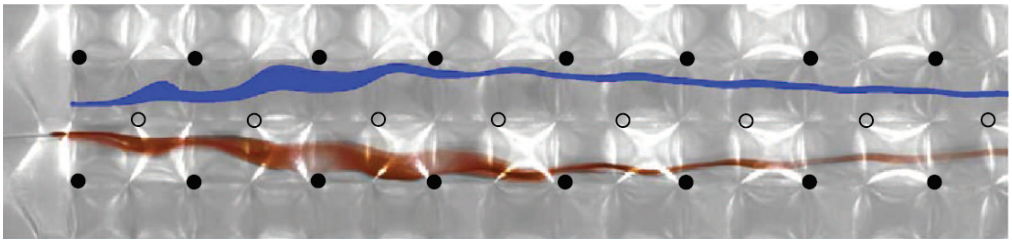

Figure 1.15.: Streamlines of colored silicone oil (red) injected close to the bottom $b(x,z) = a[\cos(2\pi x/\lambda) + \cos(2\pi z/\lambda)]$ and close to the symmetry plane $z = \pi$ (deepest point of the troughs). The lower red lines show the experimental image, the numerical streamlines are the upper blue lines. $Re = 8.2$. The filled circles indicate the global maxima while the open circles indicate the global minima of the topography. The flow direction is from left to right (x-direction). The Reynolds number is defined as $Re = q/\nu$ with the flow rate q and the kinematic viscosity ν. The topography has the amplitude a and the wavelength λ. Reprinted with permission from Heining *et al.* [64]. © AIP Publishing.

1.2.3. Inertial flow with sidewalls as bounding topography

In the real world of engineering and environmental systems, gravity-driven films are neither purely two-dimensional (Figure 1.16a) nor are they infinitely extended in three dimensions. The films are bounded by sidewalls, which can be interpreted as a special class of bounding topographies. The increasing demand for thinner films in scientific and technological applications requires a better knowledge of the effects of the sidewalls on gravity-driven film flows. For example, the recent work by Gugler *et al.* [9] discussed the operative limits of curtain coating due to edges to demonstrate the importance of considering the sidewalls in technical applications. They summarized the existing theories on edge profiles in curtain coating and presented methods to analyze edge issues in production.

Scholle and Aksel [65] presented an exact solution of visco-capillary flow in an inclined, flat channel bounded by sidewalls. Assuming that the flow is steady and unidirectional the surface shape and the velocity profile were obtained as exact solutions of the Navier-Stokes equations, valid for arbitrary Reynolds numbers. They unveiled a structural change in the velocity profile, the 'velocity overshoot' near the sidewalls, for cases with meniscus elevation higher than the apex height of the flow (Figure 1.16c). In their subsequent work, Scholle and Aksel [66] discussed the special case of thin film limit and film rupture of the visco-capillary gravity-driven channel flow. The shape of the free surface, the velocity field, and the flow rate were obtained from

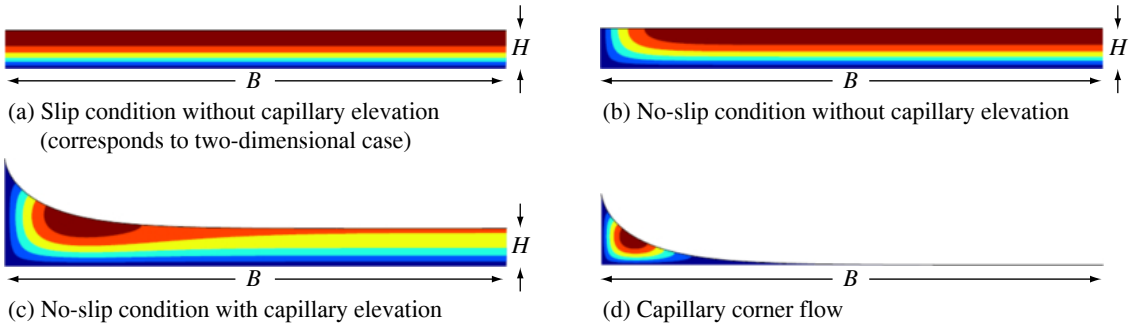

Figure 1.16.: Cross-sectional velocity field and flow configurations for different types of sidewall influence. The velocity is color-coded: blue corresponds to slow and red corresponds to fast. The geometry is described by the channel half width B and the film thickness at the center of the channel H. Modified and reprinted with permission from Haas *et al.* [67]. Grayscale was converted to color. © AIP Publishing.

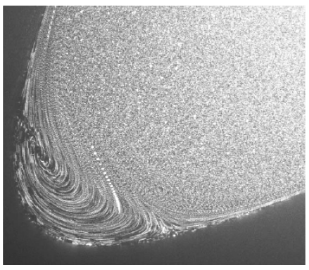

Figure 1.17.: Spiral-like pathline patterns similar to those in the vicinity of the sidewalls, where the vortex is deformed into a spiral. The film flow was visualized by adding up a series of tracer images. The main flow direction is along the mean inclination angle 45° of the substrate contour. The substrate wavelength is 20 mm, its amplitude is 9 mm, and the film thickness is 11.35 mm. Reprinted with permission from Wierschem *et al.* [26].

a pure analytical treatment. Rescaling the problem with a generalized capillary length they payed particular attention to vanishingly thin films, where capillary effects become dominant. Their calculations showed that the capillary effects caused an increased flow rate for both thin and vanishingly thin films. Beyond, they identified a rupture criterion, defining the minimum flow rate in order to avoid film rupture and capillary corner flow (Figure 1.16d). In their combined analytical, numerical and experimental approach, Haas *et al.* [67] focused on the influence of the sidewalls on thin gravity-driven films for the case of steady and draining flow. They highlighted the competing effects of the no-slip condition and the velocity overshoot due to capillary elevation at the sidewalls and discussed the deviations from the two-dimensional reference system. Please see Figure 1.16 for the respective results on the cross-sectional velocity field and the classifications of the flow configurations for the different types of sidewall influences.

To the author's knowledge, the effects of corrugated sidewalls on films flowing down flat or wavy inclines have not yet been addressed. Besides, no publication was found which considered the influence of flat sidewalls on film flows over undulated inclines explicitly. Both problem statements still remain as open questions. The only paper to mention in this context is the experimental study by Wierschem *et al.* [26]. In their experiments, they considered the structure of the vortices which formed in the troughs of deep sinusoidal undulations for gravity-driven creeping flow conditions (Section 1.1.1). They briefly outlined a symmetry break, induced by the presence of the sidewalls, the undulated bottom and a slight inclination along the channel width. This symmetry break led to a deformation of the vortex into a spiral. Spiral-like pathline patterns, similar to those shown in Figure 1.17, were observed. These patterns indicate a mixing of the main flow with the recirculation zones in the vicinity of the sidewalls. This mixing would not appear in infinitely extended, two-dimensional flow over inclined topography without sidewalls.

1.3. The inverse problem

Film flows are often investigated in the usual cause-to-effect paradigm, the so-called direct problem (Sections 1.1 and 1.2). It consists in finding the observable consequences of a set of causes and conditions. For example, information about the underlying topography is given and the free surface shape and the flow field are unknown. In the inverse problem the causes and conditions of the flow are reconstructed from the knowledge of observable consequences. In this effect-to-cause paradigm, the free surface is a signature of the flow which can be related to unknown flow quantities, i.e., unknown boundaries, flow conditions or material properties [68].

Sellier [69] calculated an a priori unknown substrate shape from a given free surface by solving the inverse problem for two-dimensional flow. He showed that the lubrication approximation, which governs the flow of a thin liquid film down an inclined topography, can be explicitly inverted. An exact analytical solution was found to reconstruct the bottom shape and the corresponding flow field from the prescribed free surface. Two applications in coating industry were mentioned: the reconstruction of the substrate from measured free surfaces and the possibility to infer the bottom topography for a target free surface profile. Heining and Aksel [70] included the influence of inertia on the reconstruction of substrate topography in steady thin film flow. They used the weighted-residual integral boundary-layer method (WRIBL) to model the flow in an asymptotic approach for thin films and moderate Reynolds numbers. That way, they were able to derive an explicit equation which allowed the reconstruction of the substrate from a known free surface. They prescribed the free surface as a monofrequent periodic function and discussed the influence of inertia, film thickness, and surface tension on the shape of the corresponding substrate. Subsequently, Heining [71] presented a numerical algorithm for reconstructing the velocity field of a viscous liquid flowing over unknown topography beyond the borderline case of thin films. This approach was based on the full Navier-Stokes equations and therefore was not relying on any simplifying assumption. The iterative algorithm relied on a discretization of the transient kinematic boundary condition. For given fluid properties, he was able to determine both the topography and the velocity field from the free surface shape. He confirmed the results of previous computations in the thin film limit [70]. Besides, he compared WRIBL and finite element method (FEM) and generalized the numerical solution to arbitrary film thicknesses.

The inverse problem for two-dimensional gravity-driven free surface flows at vanishing Reynolds numbers was addressed by Heining *et al.* [20]. In the framework of lubrication approximation they demonstrated that the knowledge of the free surface velocity is sufficient to reconstruct the free surface elevation, the film thickness, and the substrate's geometry. In line with Aksel [19], Heining *et al.* [20] showed that the wall shear stress can be inferred indirectly from a prescribed free surface velocity. Being able to infer the wall shear stress from the mere measurement of the free surface is potentially an extremely useful feat since the wall shear stress is responsible for important mechanisms such as sediment transport and erosion in geophysical flows. With the help of the integral boundary-layer approach, Heining *et al.* [72] showed that it is sufficient to know one component of the free surface velocity to reconstruct free surface elevation, film thickness, and substrate topography. They derived an explicit formula for bottom reconstruction, which could be solved analytically with a Fourier series approach. The algorithm was found to be robust against noisy input data, but its accuracy became limited when vortices appeared. Anjalaiah *et al.* [73] considered the inverse problem in gravity-driven films of shear-thinning fluids flowing down a substrate of unknown shape. They were interested in controlling the film's free surface using a suitable design of the bottom topography. Therefor, the authors assumed a power-law fluid (power-law index $n = 1$ denotes Newtonian fluid, relevant for the present consideration) and derived a WRIBL formulation analogous to the lubrication approximation. The authors obtained a single partial differential equation which related the film thickness and the free surface elevation. The problem could be approached from two directions: either finding the topography for prescribed free surface (the inverse problem) or reverse (the direct problem). For a weakly undulated, periodic free surface an exact expression for the required substrate geometry was derived.

Usha and Anjalaiah [74] included the influence of a slippery substrate on bottom reconstruction, relevant for technical systems incorporating superhydrophobic surfaces. Prescribing the free

surface of a two-dimensional flow, their goal was to obtain the corresponding geometry of a slippery substrate. Their approach followed the previous papers by Sellier [69] and Heining and Aksel [70] and extended them to the reconstruction of slippery bottoms. In the steady case, the model equations for the film thickness were derived under lubrication approximation for creeping flow and using WRIBL for inertial flow. Particular emphasis was given to the analysis of the effects of the slip parameter and the inertia on the shape of the reconstructed topography for different prescribed shapes of the free surface, i.e., sinusoidal, trench, and bell-shaped.

Heining and Sellier [75] extended previous work [20] by presenting a method to reconstruct the flow domain in three-dimensional, creeping, thin films under the action of gravity using an inversion strategy of the lubrication equation. Their method was able to reconstruct the film thickness, the internal pressure field, and the substrate with only the knowledge of the free surface velocity. They derived the corresponding partial differential equation for each unknown variable and solved them numerically. Besides, they showed that the inversion strategy is robust with respect to external perturbations in the form of noisy input data.

In the last years, the understanding of free surface flows has grown tremendously with the progress in mathematical modeling and numerical simulation. The inverse problem was not left aside by this development. A comprehensive survey of the literature dealing with inverse problems in free surface flows can be found in the recent review article by Sellier [68]. However, despite all recent progress in this field of research, the inverse problem is inherently not well posed. An uncertainty remains as the identifiability of the substrate's shape is limited by the fact that different topographies with the same amplitude and wavelength can exhibit only barely distinguishable free surfaces when recirculation zones appear [76].

1.4. Stability of film flows

1.4.1. A brief review on the stability of films over flat inclines

Two-dimensional flow

For convenience, before beginning with the stability of gravity-driven films over topographies, some issues on the stability of Nusselt films over flat inclines will shortly be recapitulated. In their pioneering theoretical [77] and experimental [78] studies, Pjotr and Sergei Kapitza unveiled that traveling free surface waves can appear spontaneously at the free surface of a gravity-driven film of water, if a critical volume flux threshold is exceeded (Figure 1.18). A few years later, Benjamin [79] and Yih [80] considered the formation of traveling free surface waves on two-dimensional laminar liquid films flowing down inclined, flat planes. In their linear stability analysis, they adapted the Orr-Sommerfeld equation [81–83] to thin film flows. They found that all Newtonian films flowing over infinitely extended flat substrates, inclined by the angle β against the horizontal, become unstable at Reynolds numbers beyond $Re_c = (5/4)\cot\beta$. Their results were valid for linear, infinitely long free surface perturbations with wave numbers $k \to 0$ and infinitesimally small amplitudes. Above the critical Reynolds number Re_c of this

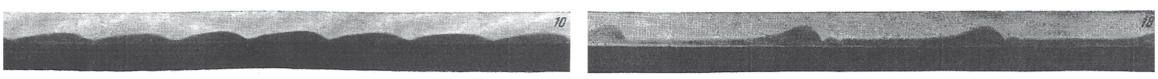

Figure 1.18.: Two examples of silhouettes of traveling waves that appear at the free surface of a film of water flowing down a flat incline. Figure taken from Kapitza and Kapitza [78].

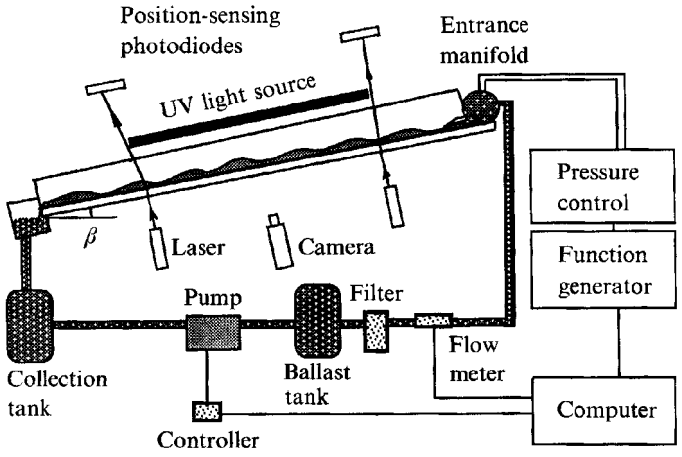

Figure 1.19.: Sketch of the film flow apparatus with variable inclination angle β. The automated flow control system with a ballast tank for noise reduction and the method of introducing periodic forcing of the input flow rate into the entrance manifold are shown. The setups to measure the local, time-resolved film thickness and, hence, flow stability are illustrated as well, i.e., laser beam deflection and fluorescence imaging. Reprinted with permission from Liu *et al.* [87]. © Cambridge University Press.

long-wave primary instability the flow was denoted as 'convectively unstable,' which means that small free surface waves grow while traveling downstream.

Subsequent work, e.g., by Lin [84] and Gjevik [85], considered the dynamics of two-dimensional films over inclined planes in the nonlinear regime – mainly built on the approach adopted by Benney [86]: an evolution equation for the film thickness, which accounts for inertia, viscosity, capillarity, and hydrostatic pressure. Lin [84] studied the finite-amplitude stability of a parallel flow with a free surface by deriving a closed-form expression for the nonlinear development of long-wave surface perturbations. He showed that in the neighborhood of the neutral curve an exponentially growing infinitesimal disturbance may develop into saturated waves of small but finite amplitude if the surface tension is sufficiently large. His results fitted well to those of the Kapitza's [77, 78]. Gjevik [85] considered the finite-amplitude traveling waves which appeared at the free surface of a viscous fluid layer flowing down an inclined plane. The growth of a linear unstable periodic perturbation and its nonlinear interaction with higher harmonics was studied. In line with the results published by Lin [84] he reported on a damping effect of the surface tension in films flowing down a vertical plane, i.e. the appearance of saturated finite-amplitude surface waves. About twenty years later, Liu *et al.* [87] and Liu and Gollub [88] experimentally validated previous theoretical findings on the primary convective instability [79, 80] and the development of saturated waves [84, 85] in two-dimensional film flow over flat inclines. Liu *et al.* [87] measured the primary instability of thin liquid films flowing over inclined planes with laser beam deflection. The setup they used is shown in Figure 1.19 and was a prototype for further measurements, also over topography. Despite their experiments dealing with waves of small but finite wave numbers, they were able to locate the onset of the primary convective instability at the theoretically predicted critical Reynolds number $Re_c = (5/4)\cot\beta$. The evolution of the waves depended strongly on the initial wave number (or the frequency f) as shown exemplarily in Figure 1.20a. Liu and Gollub [88] performed experiments on both the linear stability of films flowing down inclined planes and the dynamics of solitary waves that can form sufficiently far downstream. They showed how the curve of the neutral frequency disturbances f_c of the primary instability depends on the

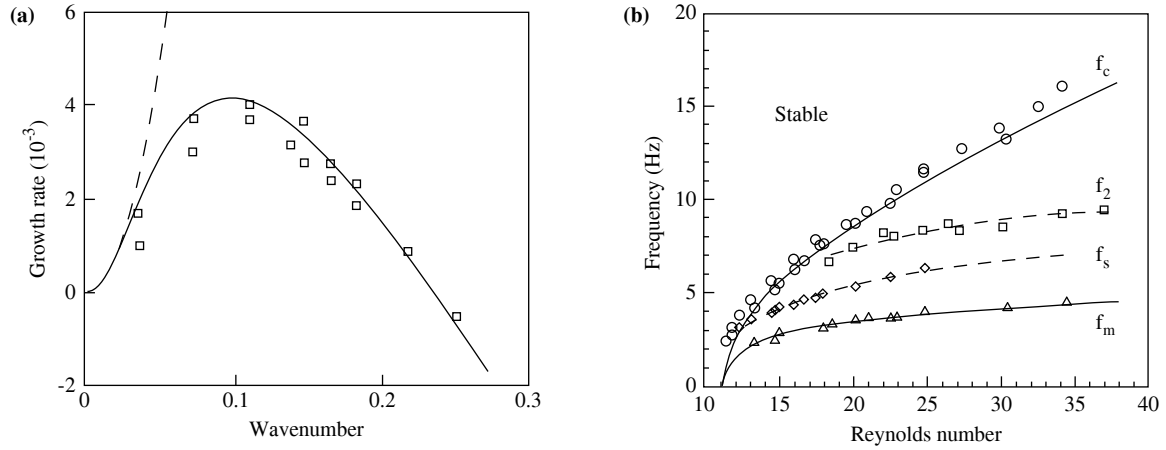

Figure 1.20.: (a) Dimensionless spatial growth rate of linear waves as a function of the wave number for glycerin-water films flowing over a plane, inclined at the angle $\beta = 4.6°$ against the horizontal. The Reynolds number is $R = 23$ and the Weber number is $W = 62$. The solid line corresponds to the predictions computed with the method due to Anshus and Goren [48]. The dashed line is the linear result of the Benney equation [86] (equation (5) in [87]). Reprinted with permission from Liu *et al.* [87]. © Cambridge University Press. (b) Phase diagram in frequency f and Reynolds number showing various regimes of linear stability, nonlinear evolution, and secondary instabilities. The inclination angle is $\beta = 6.4°$, and aqueous solutions of glycerin (54% by weight) were used. The circles are measurements of the neutral stability frequency f_c of the primary instability, below which the free surface is convectively unstable. The upper solid line is calculated from linear stability theory. The triangles show measurements of the maximum amplified frequency f_m, and the solid line through them is also the result of linear theory. The bifurcation phase boundary f_s separates two types of nonlinear evolution [87] and is given by the diamonds with a dashed trend-line. Between f_s and f_c saturated finite-amplitude waves with one maximum per period can be found. Below f_s, waves evolve into multipeaked waveforms, including solitary waves, by strongly nonlinear mechanisms. Another phase boundary f_2, shown by squares, separates the sideband and subharmonic two-dimensional secondary convective instabilities of periodic waves [89]. The sideband instability of the primary waves predominates above f_2, and the subharmonic instability at frequencies below the boundary (and close to f_m). Reprinted with permission from Liu and Gollub [88]. © AIP Publishing. In (a) and (b), the Reynolds number is defined as $R = h_0 u_0/\nu$, with the unperturbed film thickness h_0, the free surface velocity $u_0 = g h_0^2 \sin\beta/(2\nu)$, the kinematic viscosity ν and the gravitational acceleration g. The Weber number is $W = \gamma/(\rho h_0^2 g \sin\beta)$ with the surface tension γ and the density ρ of the fluid.

Reynolds number. Besides, they discussed the bifurcation phase boundary f_s which separated two types of nonlinear evolution [87]: the appearing of saturated finite-amplitude waves above f_s and multipeaked and solitary waves below. The respective results are shown in Figure 1.20b together with the phase boundary f_2, separating the sideband and subharmonic two-dimensional secondary convective instability of periodic waves, previously described by Liu *et al.* [87].

Three-dimensional flow

Three-dimensional instabilities of film flows over flat inclines were considered in experiment and theory by, e.g., Liu *et al.* [90]. They showed a primary, two-dimensional wave (k, f) to interact strongly with a pair of oblique waves (k_1,f_1) and (k_2,f_2) when they satisfy the conditions of phase synchronism: $k = k_1 + k_2$, and $f = f_1 + f_2$, where k is the wave vector. Both synchronous and subharmonic three-dimensional instabilities were found. In the first case, the spanwise deformations of adjacent wave fronts had the same transverse phase. In the second case, where the instability appeared for frequencies close to the neutral curve f_c, the transverse modulations were out of phase for successive wave fronts and herringbone patterns appeared (Figure 1.21).

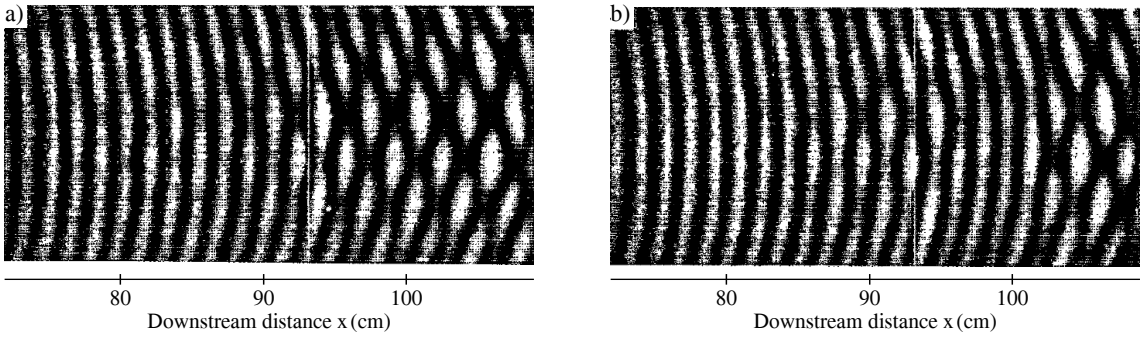

Figure 1.21.: Stabilized herringbone patterns generated by subharmonic and detuned disturbances. The herringbone patterns resulted from a broad band of subharmonic resonances. Liu *et al.* [90] superposed small periodic disturbances at frequency $f/2 + \Delta f$ on the primary two-dimensional waves of frequency f at the entrance manifold, where f is in the subharmonic three-dimensional region. They defined the 'detuning parameter' $\mu = |\Delta f|/f$. The inclination is $\beta = 4.0°$, the Reynolds number is $R = h_0 u_0/\nu = 50.5$ with the unperturbed film thickness h_0 and the free surface velocity u_0. The frequency of the disturbance is $f = 14.0\,\text{Hz}$. The secondary perturbation frequencies are (a) $f_1 = f/2 = 7.0\,\text{Hz}$; (b) $f_1 = 6.5\,\text{Hz}$. The corresponding detuning parameters are (a) $\mu = 0$ and (b) $\mu = 0.0357$. Reprinted with permission from Liu *et al.* [90]. © AIP Publishing.

Reviews and latest developments

The dynamics of traveling free surface waves in gravity-driven film flows over flat inclines were thenceforth the object of interest to several authors. As the present work focuses on films over undulated inclines, please see the reviews by Oron *et al.* [10] and Craster and Matar [12] for a more profound discussion on wave evolution over flat inclines. The author refrains from a detailed discussion of all more recent developments on this topic, e.g., the work of Trifonov [91] who used direct Navier-Stokes computations and Floquet theory to compute the linear stability and the nonlinear wave evolution for gravity-driven two-dimensional films flowing down a vertical plate.

1.4.2. The stability of films over undulated topography

Localized topographies

The stability of gravity-driven free surface thin film flows over flat inclines exhibiting a localized topographical feature was considered by Kalliadasis and Homsy [92] and Bielarz and Kalliadasis [93]. Kalliadasis and Homsy [92] studied thin film flows over a step-down topography, the steady states of which have been examined previously by Kalliadasis *et al.* [16, 17]. The steady-state flow over such a step-down develops a ridge at the free surface right before the entrance to the step (please see Figure 1.1 in Section 1.1.1). Such capillary ridges have been observed in the contact-line motion over a planar substrate and are a key element of the instability of the driven contact line (please see Oron *et al.* [10] and Craster and Matar [12] for an elaborate discussion on moving contact lines). Kalliadasis and Homsy [92] analyzed the linear stability of the ridge with respect to disturbances in the spanwise direction. They showed that the operator of the linearized system has a continuous spectrum for disturbances with wave numbers less than a critical value above which the spectrum is discrete. Their main result was that, unlike the driven contact line problem where an instability grows into well-defined rivulets, the topography-driven ridge was stable for a wide range of pertinent parameters. The reasons for the stability of the ridge were established through an energy analysis. The mechanism responsible for the damping of the perturbations was found to depend on the wave number. At

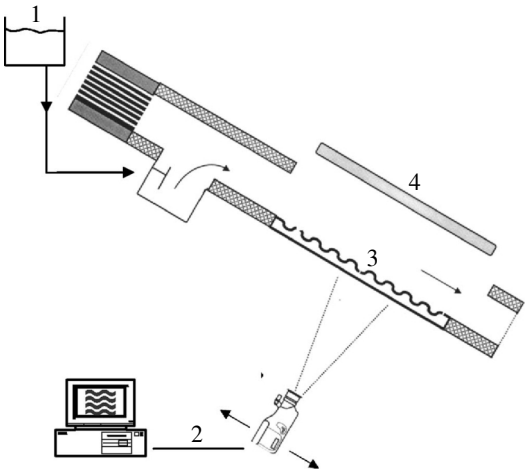

Figure 1.22.: Sketch of the experimental apparatus used by the group of Bontozoglou (e.g., in [53, 54]) to measure the critical Reynolds number for the onset of the primary instability in gravity-driven films over undulated inclines. 1: overflow tank which provides a constant head; 2: image grabbing system; 3: corrugated substrate; 4: UV light source. Modified and reprinted with permission from Argyriadi *et al.* [54]. © AIP Publishing.

small wave numbers, the stability of the capillary ridge was due to a rearrangement of the fluid in the flow direction owing to the net pressure gradient induced by the topography. At moderate to large wave numbers, the stability was due to the surface tension acting in concert with the spanwise curvature. The results by Kalliadasis and Homsy [92] were sustained by the findings of Bielarz and Kalliadasis [93], who numerically solved the lubrication equation for two- and three-dimensional thin film flow over localized topography, i.e., step-down, step-up, trench, and hump. They included the effects of inertia and intermolecular forces and demonstrated that the free surface was remarkably stable against disturbances in the transverse direction and the influence of inertia: the ridge recovered its original shape as soon as the disturbances traveled downstream and trained out of the ridge. A destabilization of the free surface in transverse direction could be achieved by large-amplitude free surface perturbations. Dávalos-Orozco [94] studied instabilities of gravity-driven thin films flowing over substrate deformations distributed in a small space interval. He simulated a sinusoidal topography in a finite interval by smooth functions and based his numerical work on a modified Benney equation [86, 95]. His results indicated that this type of smooth, localized topography can indeed have a stabilizing effect on the flow, i.e., can act as a passive mechanism to filter time-dependent perturbations.

Weak periodical undulations

The free surface stability of films flowing over weak, periodical, rectangular substrate undulations was studied in experiments by Vlachogiannis and Bontozoglou [53] and Argyriadi *et al.* [54]. They used a fluorescence imaging method (Figure 1.22) to capture the evolution of film height in space and time with an accuracy of a few microns. As long as the amplitudes of the traveling disturbances remained small, they were dominated by the statically deformed free surface (please see Section 1.2 for free surface resonance), and manifested only as small oscillations in the amplitude and phase shift of the base pattern. Further downstream, they evolved into large solitary waves and multipeaked humps. The traveling waves exhibited a regular frequency, indicating that the spatial forcing imposed by the periodic corrugations resulted in a selection process. In terms of flow stability, their key finding was a remarkable stabilization of the flow

at high Reynolds numbers, which proceeded through the development of a three-dimensional flow structure and led to both a temporary decrease in film thickness and a recession of solitary waves. Argyriadi *et al.* [54] studied basically the same system and considered the effect of corrugation steepness on steady (Section 1.2) and unsteady film flow. Their experiments showed that the stability threshold, i.e., the critical Reynolds number, increased drastically with the corrugation steepness. This result was anticipated analytically for sinusoidal undulations by Wierschem and Aksel [96]. They performed linear stability analysis of a Newtonian liquid film flowing down an inclined wavy plane of sinusoidal shape. Their theoretical method was based on a long-wave approximation with small perturbation amplitudes. As for the flow over a flat incline, a long-wave type primary instability was found, but the critical Reynolds number for the onset of the traveling free surface waves increased with the waviness and the inclination of the substrate. Their finding that the presence of a long-wave bottom undulation tends to stabilize the flow was confirmed experimentally by Wierschem *et al.* [97] who considered the effect of long undulated substrates on thin gravity-driven films, both experimentally and analytically in the framework of Floquet analysis. They unveiled a stabilizing effect of weakly corrugated substrates, i.e., a shift of the neutral curve (Figure 1.23a) and the critical Reynolds number (Figure 1.23b). General consensus of these early approaches [53, 54, 96, 97] was that a slightly corrugated topography stabilizes the film flow compared to the corresponding Nusselt flow over a flat incline. A minor shift of the critical Reynolds number was reported and the shape of the neutral stability curve (a long-wave type primary instability) was found to remain qualitatively unaffected.

Numerical investigations by Trifonov [98, 99] considered the free surface stability of gravity-driven viscous film flows along weak and moderate sinusoidal undulations over a wide range of Kapitza and Reynolds numbers. His linear stability analysis of integral boundary-layer [98] and full-scale Navier-Stokes approaches (including spectral analysis with Chebyshev polynomials) [99] unveiled that substrate undulations stabilize the flow significantly if they provoke a substantial increase of the average film thickness compared to the corresponding Nusselt flow. Besides, the undulations had a destabilizing effect on the flow if their period 'matched' with the period of the free surface perturbations. For the practically important case of the corrugation's amplitude and the Nusselt film thickness being of about the same size, Trifonov [99] demonstrated that the results given by a simplified integral approach were in good agreement with those obtained by applying the Navier-Stokes equations in their full statement. Dávalos-Orozco [95] modified the Benney equation [86], which is a nonlinear evolution equation in the small wave number approximation, to scrutinize the stability of two-dimensional gravity-driven thin film flows over smoothly deformed substrates, i.e., the same system studied by Wierschem and Aksel [96]. The equation described the film's free surface deformation including the effects of inertia, viscosity, and surface tension and had a forcing term that corresponded to periodic time-dependent perturbations hitting on the free surface. He stated that the stabilizing effect of a sinusoidal substrate can be increased by steepening its undulations.

Deep periodical undulations: surface tension effects on the stability threshold

Heining and Aksel [70, 100] and D'Alessio *et al.* [101] considered the combined effect of surface tension, inertia and topography steepness on the stability of film flows along inclines exhibiting steep sinusoidal undulations. General consensus of these three approaches [70, 100, 101] was that the flow can either be stabilized or destabilized by steep substrate undulations, depending on the amplitude and wavelength of the substrate and the surface tension of the fluid. Heining and Aksel [70] computed both the steady solution and, in an unconventional approach, the linear

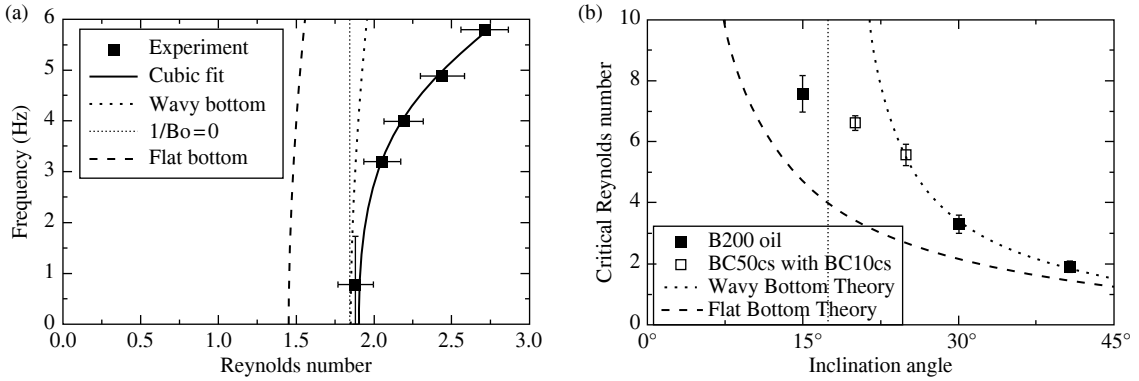

Figure 1.23.: (a) Experimental linear stability curve compared to theoretical predictions for wavy inclines according to Wierschem *et al.* [97] and for a flat incline at the mean inclination angle. The thin dotted line shows the corresponding result without considering the surface tension. In the experiment, the thin film parameter $\delta = 2\pi h/\lambda$ varied between 0.065 and 0.073. The topography steepness was $\zeta = 2\pi a/\lambda = 2\pi \cdot 0.05$, the inclination was $\alpha = 45°$ and the inverse Bond number $1/Bo = 4\pi^2 l_{Ca}^2/(\lambda^2 \sin\alpha) = 0.002$ with the capillary length $l_{Ca} = [\sigma/(\rho g)]^{1/2}$. The topography's amplitude is a and its wavelength is λ. The steady-state film thickness is $h = [3\eta\dot{Q}/(\rho g \sin\alpha)]^{3/2}$ with $\dot{Q}$ being the flow rate. The surface tension of the fluid is σ, its density is ρ and its dynamic viscosity is η. The gravitational acceleration is g. (b) Minimum critical Reynolds number as a function of the inclination angle. The experimental values were obtained from an extrapolation to 0 Hz; the theoretical curve for the wavy substrate is according to Wierschem *et al.* [97]. The topography steepness was $\zeta = 2\pi \cdot 0.05$. Modified and reprinted with permission from Wierschem *et al.* [97]. © Springer Nature.

stability of thin film flow over sinusoidal topography in the context of bottom reconstruction (please see Section 1.3 for the inverse problem). From the solution of the inverse problem they obtained a bottom profile, which itself served as starting point for the stability analysis. Instead of studying the stability of the bottom topography, they computed the corresponding free surface stability. They transferred the stability of the inverse problem to the stability of the direct problem. They applied monodromy theory [102] to the linearized equations and reported that the substrate undulations had, in general, a stabilizing effect on the flow. However, when the surface tension was sufficiently large, a destabilization was observed. The approach by D'Alessio *et al.* [101] was based on an extension of the modified integral boundary-layer equations proposed by Ruyer-Quil and Manneville [103] for flows over even substrates to flows over topography. A linear stability analysis of the steady flow was carried out by taking advantage of Floquet-Bloch theory. Their main conclusion was that, in general, for weak to moderate surface tension (large Weber numbers), bottom topography acts to stabilize the flow. For stronger surface tension (small Weber numbers), bottom topography can destabilize the flow provided that the wavelength of the substrate undulations is sufficiently short. While the stabilizing effect of substrate topography on film flows has previously been reported by Wierschem *et al.* [97] for weak surface tension and Balmforth and Mandre [104] for zero surface tension, D'Alessio *et al.* [101] described the potentially destabilizing combined effect of bottom topography and surface tension in line with the results by Heining and Aksel [70]. Heining and Aksel [100] studied effects of inertia and surface tension on a thin film of a power-law liquid flowing down an inclined wavy plane with sinusoidal topography (power-law index $n = 1$ denotes Newtonian fluid, relevant for the present consideration). Based on the von Kármán-Pohlhausen method [105, 106] an integral boundary-layer model for the film thickness and the flow rate was derived. For weakly undulated substrates, they solved the governing equation analytically by a perturbation approach and found a resonant interaction of the free surface with the wavy incline. A study on the inverse Bond number revealed that surface tension had

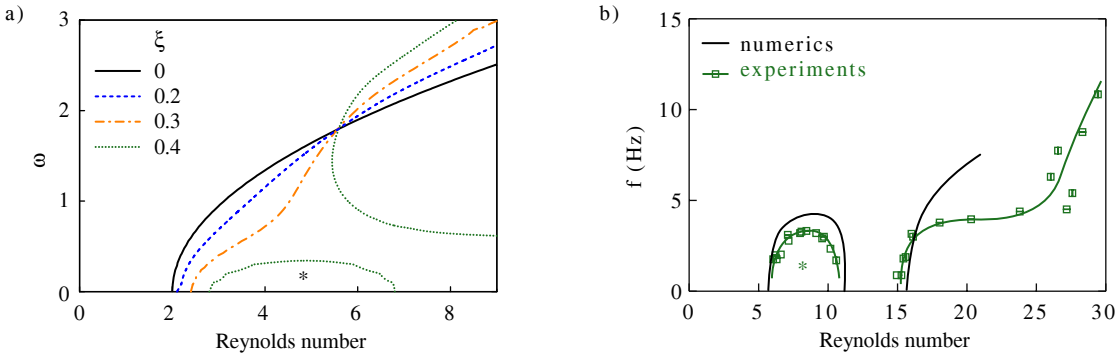

Figure 1.24.: Examples of linear stability charts of gravity-driven Newtonian films flowing over steep sinusoidal corrugations. (a) Dimensionless frequency ω (according to [47]) of the neutral disturbance against the Reynolds number for varying steepness $\xi = a/d$ of the topography. The amplitude of the topography was a and the steady-state film thickness was d. The results correspond to Newtonian fluids with power-law index $n = 1$. The stress tensor was defined as $\tau_{ij} = 2\eta_n(2D_{kl}D_{kl})^{(n-1)/2}D_{ij}$ according to Spurk and Aksel [15]. Data from [100]. (b) Frequency f of the neutral disturbance against the Reynolds number. The graph shows a segmented stability chart with an unstable isle (*). Data from [107, 108]. Modified and reprinted with permission from Schörner and Aksel [114]. © AIP Publishing.

a significant impact on the stability of the film. For the case of Newtonian fluids, small inverse Bond numbers always led to a stabilization, higher inverse Bond numbers to a destabilization of the flow compared to the corresponding Nusselt flow over a flat incline.

Deep periodical undulations: stability chart patterns

Recent research [76, 100, 107–114] reinforced previous findings on flow stabilization and destabilization due to topography effects and reported on severe changes of the entire shape of the linear stability chart of gravity-driven Newtonian films flowing down steep periodical topographies. Patterns of stability charts were described, differing significantly from the classical long-wave type instability valid for free surface flows over flat inclines (Figure 1.24a, topography steepness $\zeta = 0$). Heining and Aksel [100] were the first to report on this phenomenon, i.e., the formation of an unstable isle in the stability chart of a Newtonian film flowing over deep sinusoidal corrugations (Figure 1.24a, $\zeta = 0.4$). As their approach was actually not able to resolve, for example, the formation of the eddies in the troughs of such steep undulations, the authors declared the segmentation of the neutral curve to be an artifact of the linearization. Surprisingly, subsequent measurements [107] and computations [108] provided the evidence that an unstable isle can indeed exist in the stability chart of Newtonian films flowing over strongly sinusoidally corrugated inclines (Figure 1.24b). The experimental work by Pollak and Aksel [107] reported on crucial flow stabilization and multiple instability branches in the linear stability chart of gravity-driven viscous films flowing down a wavy incline of sinusoidal shape. Decreasing the viscosity of the liquid led to a transition from a long-wave to a short-wave type instability. Increasing the viscosity led to a disjoining of the instability branches, i.e., the formation of an unstable isle in the stability chart. Beyond, a destabilization of the flow compared to the corresponding Nusselt flow and a very strong stabilization of the flow up to a factor of two for arbitrary linear disturbances and even up to a factor of four for linear short-wave disturbances was observed when the viscosity was large. They also presented a first approach for a topography shape, based on the shape of the eddy, which was optimized in terms of flow stability – a finding of enormous potential for coating applications. Trifonov [108] performed

direct Navier-Stokes computations and used Floquet theory to consider the free surface stability of a viscous film flowing down steep sinusoidal undulations. His numerical algorithm allowed the computation of both the steady-state solution of the nonlinear equations and the rates of growing or damping in time of the arbitrary two-dimensional disturbances of the solution which were bounded in space. The critical Reynolds number for the onset of the primary instability was found to depend essentially both on the topography parameters and the liquid's physical properties. For different Kapitza numbers, inclination angles, and Reynolds numbers, regions of topography parameters (amplitude and period) were obtained, where all two-dimensional disturbances decayed in time. His numerical study was the first to validate the precedent experimental approach by Pollak and Aksel [107]. Cao *et al.* [109] studied the primary instability of a liquid film flowing along steep periodical substrates of both sinusoidal or rectangular shape. They provided the experimental evidence for a short-wave global mode in film flow along deep periodic corrugations. They found that, with increasing inclination, an abrupt transition in the instability mode is manifested: the classical long-wave instability, which is convective and thus determined by the characteristics of externally imposed excitation, was replaced by a new short, traveling mode, which was highly regular and strongly two-dimensional. The short-wave mode introduced an intrinsic frequency which was insensitive to external excitation and appeared to be a global mode. The exact shape of the corrugations (sinusoidal or rectangular) had a leading-order effect on the inclination at which the new mode appeared and on its wavelength at inception.

Experiments by Schörner *et al.* [76] addressed the question whether a segmented stability chart, in particular the unstable isle found by Pollak and Aksel [107] and Trifonov [108] (see Figure 1.24b), is a unique feature of deep sinusoidal undulations or a more general phenomenon. Intriguing questions concerning the inverse problem (Section 1.3) and the origin of the unstable isle arose. Subsequent experimental work by Schörner *et al.* [110] proved that the unstable isle is a consequence of competing effects of the steady-state flow phenomena. Beyond, they observed a switching between the unstable isle and a stable isle, i.e., the joining and disjoining of instability branches, when the system parameters were changed. Numerics by Trifonov [111] considered viscous liquid film flow down an inclined, sinusoidally corrugated substrate. The calculations were performed using an integral model and the stability of nonlinear steady-state flows to arbitrary perturbations was examined using Floquet theory. He showed that for each type of corrugation there is a critical Reynolds number for which unstable perturbations occur. This value greatly depended on the physical properties of the liquid and the geometric parameters of the flow. In particular, he identified corrugation amplitudes and wavelengths for which the film flow down a wavy substrate was stable to arbitrary perturbations up to moderate Reynolds numbers. Such parameter values existed for all inclination angles he considered. In his subsequent work, Trifonov [112] performed direct Navier-Stokes computations on the linear and nonlinear stability of a gravity-driven film flow down a sinusoidally undulated incline. He showed that the wavelength of the topography is decisive for the switching phenomenon: At small topography wavelengths, an increase of the amplitude to wavelength ratio of the topography provoked the formation of an unstable isle. At larger values of the topography's wavelength a stable isle appeared when the amplitude to wavelength ratio of the substrate was increased. The combined experimental and numerical approach by Schörner *et al.* [113] scrutinized the previously discovered [110] switching between different types of stability isles in films over topography in-depth. Their work gave rise to a fundamental question: Is there a universal principle, being valid to describe the parametric evolution of the linear stability charts of gravity-driven Newtonian films flowing over inclined, periodic topographies for variations of

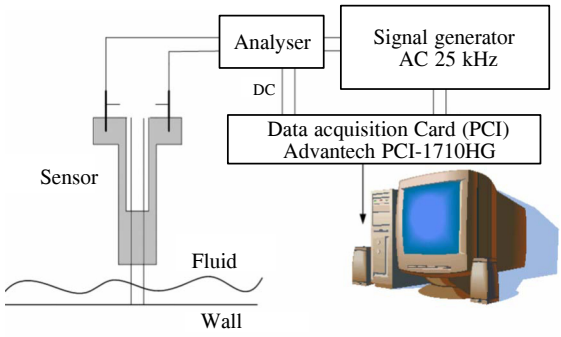

Figure 1.25.: Experimental setup to determine the onset of the free surface instability with a conductivity technique. Modified and reprinted with permission from Vlachogiannis *et al.* [115]. © AIP Publishing.

different system parameters? The characteristic stability chart patterns and the 'stability cycle' identified by Schörner and Aksel [114] provided the answer to this intriguing question.

1.4.3. The stability of films with sidewalls as bounding topography

Until today, the influence of sidewalls on the free surface stability of a gravity-driven open channel flow was only investigated experimentally. The author did not find any publication dealing with the theory of this very demanding topic, i.e., the stability of three-dimensional gravity-driven film flows with bounding sidewalls. Great technical difficulties arise in both theory and experiment when considering this intriguing problem.

The experimental approach by Vlachogiannis *et al.* [115] studied the effect of a finite and variable channel width on the primary instability of a gravity-driven viscous film flowing down a flat incline. They compared the free surface heights at two different streamwise locations by conductivity probes in the small wave number limit to detect the onset of the interfacial instability. Please see Figure 1.25 for the experimental setup they used. When the channel was narrow and not too steep, its finite width was found to have a stabilizing effect on the flow and the deviation from the classical prediction [79, 80] scaled inversely with the product of the channel width and the sine of the inclination angle. Vlachogiannis *et al.* [115] tentatively attributed the stabilizing effect of the sidewalls to their influence on the traveling disturbances, which resulted in the downstream development of curved crestlines and a transverse variation of wave characteristics – findings published shortly after by Leontidis *et al.* [116]. Their experimental paper documented the characteristics of the first waves that were observed beyond the primary instability (convectively unstable but adjacent to the neutral curve) by applying a fluorescence imaging technique. The crests of the waves attained a parabolic shape, which was symmetric with respect to the channel's centerplane. The apex curvature of the parabola varied inversely with the channel width and the Reynolds number. The height of the wave was maximum at the centerplane and decreased to zero at the sidewalls, irrespective of the wetting properties. The subsequent work by Georgantaki *et al.* [117] provided the experimental evidence that the delay in the primary instability of gravity-driven film flows in inclined channels of finite width scales with the ratio of capillary to viscous forces, i.e. the Kapitza number (which depends on the properties of the liquid only). Compared to the corresponding two-dimensional film, the flow in channels bounded by sidewalls was stabilized the more, the higher the Kapitza number was (see Figure 1.26). They emphasized that the delay of the onset of the primary instability correlated very satisfactorily only with the Kapitza number or the capillary number, and not with other dimensionless parameters that are frequently used to

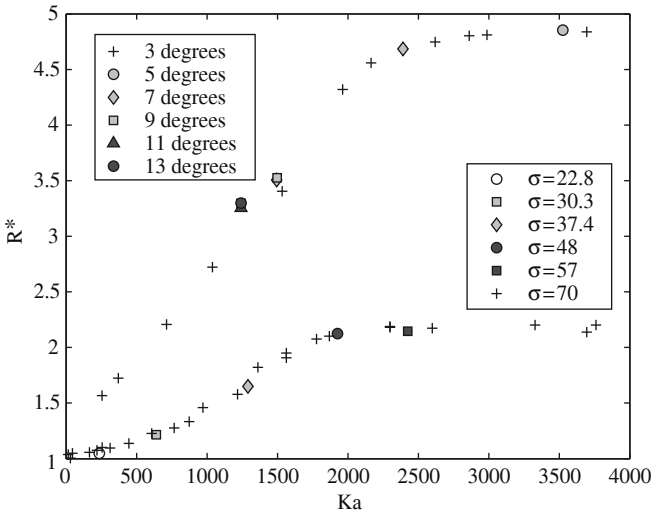

Figure 1.26.: Dependence of the delay $R^\star = Re_c/Re_c^\circ$ of the instability in a flow bounded by sidewalls compared to the corresponding two-dimensional flow as a function of the Kapitza number Ka for different inclination angles, fluids, and channel widths W (upper curve: $W = 100$ mm; lower curve: $W = 250$ mm). The critical Reynolds number for two-dimensional flow is Re_c°, and the measured critical Reynolds number of the flow bounded by sidewalls is Re_c. The Kapitza number was defined as $Ka = \sigma/(\rho g^{1/3}\nu^{4/3})$ with the gravitational acceleration g and the fluid's kinematic viscosity ν, density ρ and surface tension σ (in mN/m). Modified and reprinted with permission from Georgantaki *et al.* [117]. © American Physical Society.

express the effect of surface tension, such as the Weber number or the Bond number. Besides, the delay did not vary with the inclination, at least in the range tested. Experiments by Pollak *et al.* [118] considered the effects of the sidewalls on the primary instability of gravity-driven films flowing over flat inclines of finite width. They measured the neutral stability curves for different sidewall distances (Figure 1.27) and contact angles between the fluid and the sidewall. Both parameters had a remarkable influence on flow stability. The neutral curves in the near vicinity of the sidewall combine both features of the boundary layer (short-wave instability) and the free surface (high sensitivity to perturbations, hence low critical Reynolds number). With increasing sidewall distance a transition from short-wave to long-wave instability takes place. Furthermore, Pollak *et al.* [118] investigated the influence of the capillary elevation and the velocity overshoot near the sidewalls on the stability of the flow. They found that the velocity overshoot tends to destabilize the free surface. Based on the previous studies by Haas *et al.* [67] and Pollak *et al.* [118], Guzanov *et al.* [119] performed experiments to characterize the effects of the sidewalls on the transition from two-dimensional to three-dimensional wave evolution in a film flowing over a vertical plate. The results so obtained allowed to determine the boundaries within which the adequate comparison between modeling and experiments on wave propagation in three-dimensional films is possible.

As in the case of steady inertial flow with sidewalls as bounding topography (Section 1.2.3), the effects of corrugated sidewalls on the linear free surface stability of films flowing down flat or wavy inclines have not yet been addressed. Besides, the author did not find any publication which considered the influence of flat sidewalls on the stability of film flows over undulated inclines. In steady-state flow over steep corrugations, the sidewalls were found to provoke a symmetry break which led to a deformation of the eddies deep in the troughs into a spiral when the free surface was perturbed with time-periodic traveling waves [26] (see Figure 1.17). Penetration depths of the free surface disturbances which are as large as these indicate strong

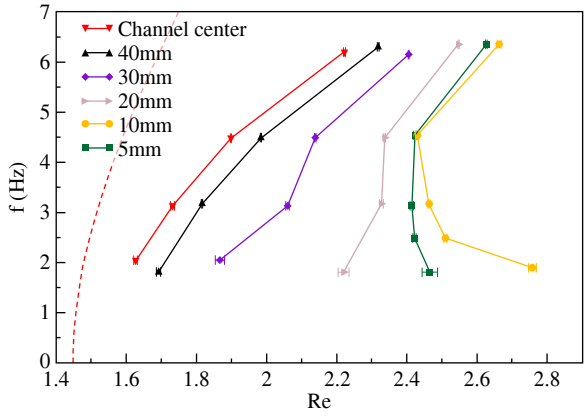

Figure 1.27.: Neutral stability curves for the contact angle 8° between the sidewalls and the liquid. The different measurements correspond to different crosswise distances of the measurement positions from the sidewall. Lines between the measurement points are linear interpolations to guide the eye. The dashed line indicates the neutral stability curve for the plane flow of infinite extend. The channel was inclined by 41° against the horizontal. Modified and reprinted with permission from Pollak *et al.* [118]. © AIP Publishing.

sidewall effects at the free surface of gravity-driven film flows and concomitant on their free surface stability. However, both experimental and theoretical work on this intriguing problem is still waiting for its solution.

2. Scope of this dissertation

The present dissertation deals with the effects of different types of topographies on the free surface stability of gravity-driven viscous films. Comprehensive experiments were combined with all existing analytical, numerical and experimental findings on this complex problem. That way, new flow phenomena were uncovered and attributed to fundamental mechanisms, which determine the flow dynamics. The aim of the present study was to characterize the results so obtained for the sake of unveiling a universally valid principle, being able to describe and unify all findings on the linear stability of viscous films flowing over inclined topographies.

The dissertation is structured as follows: After an introductory summary of the large body of precedent publications on the effects of topography and inertia on gravity-driven film flows in the foregoing Chapter 1, all the experimental systems and setups, which have been used in this study, are presented in Chapter 3. In Chapter 4, new findings on the stability of gravity-driven viscous films are presented. In particular, Section 4.1 considers the question whether the topography's specific shape matters in general for the linear stability of film flows. The parameter study condensed in Section 4.2 describes stability phenomena far beyond the Nusselt flow and identifies a competition between stabilizing and destabilizing flow phenomena. In the subsequent Section 4.3, characteristic stability chart patterns and a universal pathway for the stability of viscous films over inclined topographies are presented. Section 4.4 is devoted to what is beyond the linear stability of the two-dimensional Newtonian films considered in the previous sections of Chapter 4. Summarizing conclusions are presented in Chapter 5 and close the present dissertation.

3. Experimental systems and setups

3.1. Experimental systems

The gravity-driven flow of a viscous liquid film down an inclined open channel with a periodic substrate topography was studied. The liquids, the flow facilities and the topographies characterize the experimental systems.

3.1.1. Liquids

Three silicone oils from *Elbesil* were used as liquids. The oils were denoted as *Elbesil 65*, *Elbesil 100*, and *Elbesil 145* and had different viscosities but almost equal densities and surface tensions. All three silicone oils showed Newtonian behavior within the temperature range and shear rate considered. Their kinematic viscosity ν, density ρ and surface tension σ at the temperature $\theta = (24.0 \pm 0.3)\,^{\circ}\mathrm{C}$, where all experiments on film flows were performed, are listed in Table 3.1.

The dynamic viscosity η and the density ρ were measured to determine the kinematic viscosity $\nu = \eta/\rho$. The measurements of the dynamic viscosity η were performed with an Ubbelohde capillary viscosimeter from *Schott*. Different capillaries type *501* were used, which were plunged into a water bath. During these measurements, the temperature of the liquid was controlled by a thermostat type *CT 52* from *Schott*. The precisions of the capillaries of the viscosimeter were between 0.65 % and 0.80 % and the accuracy of the thermostat was 0.05 °C.

The density ρ was measured with a Mohr Westphal balance from *Kern* with an accuracy of $0.3\,\mathrm{kg/m^3}$. During these measurements, the temperature of the liquid was controlled by a thermostat type *ecoline RE204* from *Lauda*.

The measurements of the surface tension σ were carried out with a ring-tensiometer type *TE1CA-M* from *Lauda* with a resolution of $0.1\,\mathrm{mN/m}$. The temperature of the liquid was controlled by a thermostat type *RC 6 CP* from *Lauda* during these measurements.

The fluctuations of the measurement temperature $\theta = (24.0 \pm 0.3)\,^{\circ}\mathrm{C}$ during one experimental run of the film flow measurements was the main error source for the errors of the liquid properties. Hence, η, ρ and σ were measured in the temperature range from 21.0 °C to 26.0 °C in steps of 1.0 °C to determine their absolute values at $\theta = (24.0 \pm 0.3)\,^{\circ}\mathrm{C}$ and the corresponding errors. Both are listed in Table 3.1.

The ratio of surface tension forces to inertial forces is represented by the Kapitza number [11]

$$Ka = \frac{\sigma}{\rho g^{1/3} \nu^{4/3}}. \tag{3.1}$$

Please see Table 3.1 for the Kapitza numbers of *Elbesil 65*, *Elbesil 100* and *Elbesil 145*.

3.1.2. Flow facilities

The flow facilities and the flow circuit are sketched in Figure 3.1. A pump transported the liquid from a temperature-controlled reservoir via a pipe and tube system with a bypass to a

Notation	ν (mm^2/s)	ρ (kg/m^3)	σ (mN/m)	Ka
Elbesil 65	65.1 ± 1.0	958.5 ± 0.4	19.91 ± 0.04	3.71 ± 0.08
Elbesil 100	100.3 ± 0.6	963.2 ± 0.8	20.07 ± 0.06	2.09 ± 0.02
Elbesil 145	144.2 ± 0.5	964.8 ± 0.4	20.01 ± 0.10	1.28 ± 0.01

Table 3.1.: Liquid properties and Kapitza numbers of the three silicone oils used in the experiments at the main measurement temperature $\theta = (24.0 \pm 0.3)\,^\circ$C.

tank at the inflow of an inclined, open channel. From there, the liquid flowed gravity-driven down the channel and back into the reservoir.

Three different channels were used in the experiments. The channels were all bounded by a flat aluminum bottom and transparent, planar Plexiglas® sidewalls. All channels had the same width $b_c = (170 \pm 1)$ mm in the crosswise y-direction but different overall lengths in the streamwise x-direction. The length was 2.1 m for channel 1, 1.4 m for channel 2, and 2.0 m for channel 3. Each channel was mounted on a vibration isolating table. Exchangeable substrates made of aluminum were mounted on the bottom plate of each channel, close to the inflow. The substrates were at least 860 mm long, as wide as the channel and exhibited different topographies. The inclination angle α of the channels against the horizontal could be adjusted continuously between 0° and 90°. This angle was determined with a *Mitutoyo Pro 360 Digital Protractor 950-315* with a reading precision of 0.1°. In the crosswise y-direction, the channels were leveled with a spirit level type *Pro 360*, also from *Mitutoyo*, which was aligned perpendicular to the sidewalls and had a precision of 0.1 mm/m per scale spacing.

Eccentric screw pumps from *PF Jöhstadt*, type *AFJ 15.1B/2B* for *Elbesil 65* and type *AFJ 40.1B* for *Elbesil 100* and *Elbesil 145* provided a constant volume flux $\dot{V}$ up to 35 l/min with fluctuations of less than ± 3 cm^3/s. The volume flux could be adjusted either in discrete steps by changing the angular frequency of the pumps or, more precisely, by continuously varying the valve of the bypass.

A thermostat type *Thermo Haake TC300*, coupled to a temperature sensor *Almemo 4290-7* via a custom made *LabView* program, maintained the temperature of the liquid at $\theta = (24.0 \pm 0.3)\,^\circ$C during all measurements. The temperature sensor was placed inside the channel close to the outflow.

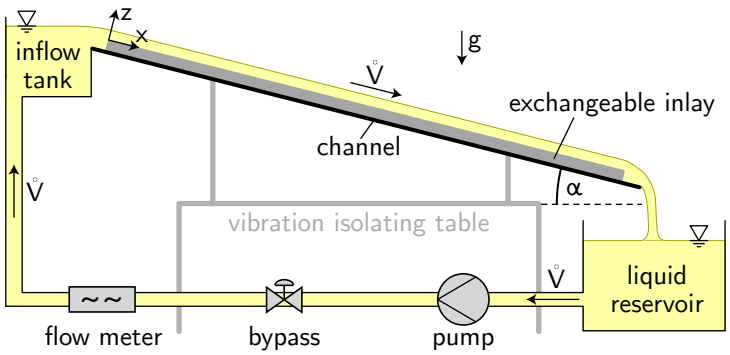

Figure 3.1.: Sketch of the flow facilities and the flow circuit used in the experiments.

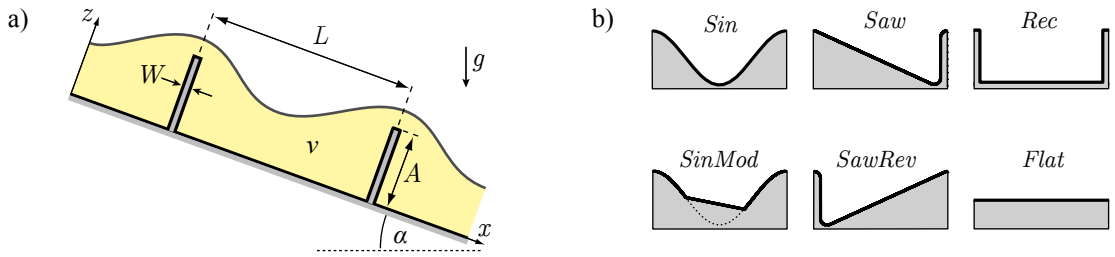

Figure 3.2.: (a) Geometry and notations of the viscous film flow over the inclined topography. (b) Sketch of the specific shapes of the topography, i.e. sinusoidal ($shape = Sin$), modified sinusoidal ($SinMod$), sawtooth-like (Saw), reversely mounted sawtooth-like ($SawRev$), rectangular (Rec) and flat ($Flat$). The main flow direction is from left to right. Modified and reprinted with permission from [114]. © AIP Publishing

3.1.3. Topographies

The substrate inlays placed in the channels as described in Section 3.1.2 exhibited different surface topographies. A schematic view of the inclined topography with a liquid film is illustrated in Figure 3.2a. The topography's parameters are its specific *shape*, inclination α, amplitude A, wavelength L, and tip width W.

The different specific shapes of the topographies are sketched in Figure 3.2b. All topographies were either periodically undulated in the streamwise x-direction or exhibited a flat surface shape ($shape = Flat$). The modified sinusoidal topography ($SinMod$) was obtained by replacing the eddies, which form in the troughs of the sinusoidal topography (Sin) by a solid contour [76, 107]. The non-smooth topography Rec had a rectangular shape and tips of the width W. The topographies Saw and $SawRev$ exhibited identical sawtooth-like shapes, but were oriented differently against the main flow direction. Their edges were rounded and had a radius of 1.0 mm.

In the experiments, the inclination α was varied between 4.1° and 36.7°. For the corrugated substrates, the amplitude A was varied from 2.0 mm to 12.0 mm, the wavelength L was varied from 10 mm to 200 mm, and the tip width W was varied from 1 mm to 100 mm. The flat incline was considered as either the borderline case $A = 0$, $L = 0$, $L = \infty$, or $W = L$ of the periodically undulated topographies.

3.1.4. Tracer particles and dye

The silicone oils were seeded with hollow glass spheres type *80A601* from *Dantec* which served as tracer particles and faithfully followed the flow dynamics. According to the manufacturer the mean particle diameter was $d_p = 10\,\mu$m and the density was $\rho_p = 2230\,\mathrm{kg/m^3}$. Additionally, the volume weighted particle size distribution was measured with a *Mastersizer 2000* laser diffraction particle size analyzer from *Malvern Instruments*. The results are plotted in Figure 3.3a. The median particle size was $d_{V,50} = 9.64\,\mu$m and the grade of dispersity [120] was $\xi_d = (d_{V,84} - d_{V,16})/(2d_{V,50}) \approx 0.45$. The quantities $d_{V,j}$ denote the particle sizes, which were greater than or equal to j% of all particles. According to Happel and Brenner [121], the sedimentation speed $w_{sed} = {d_p}^2 g(\rho_p - \rho)/(18\eta)$ of the spheres in the three silicone oils *Elbesil 65*, *100* and *145*, listed in Table 3.1, was 1.0×10^{-3} mm/s, 6.6×10^{-4} mm/s, and 4.6×10^{-4} mm/s, respectively. These sedimentation velocities were several orders of magnitude smaller than the typical flow velocities in the experiments. The sedimentation distance during one experimental run never exceeded the median particle size.

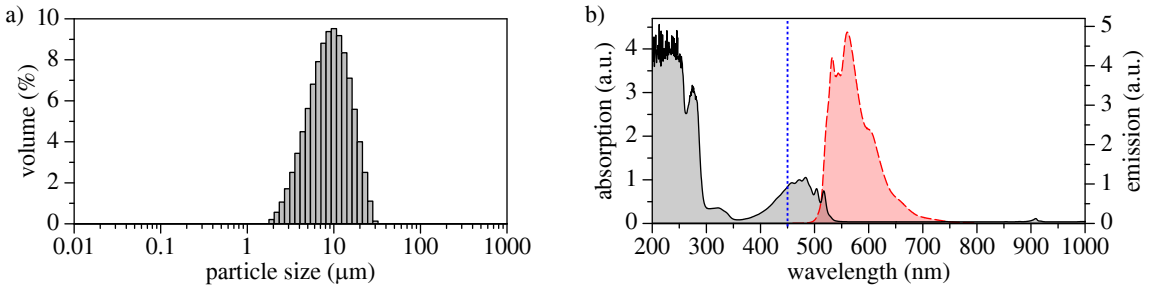

Figure 3.3.: (a) Particle size distribution of the tracer particles. (b) Photophysical properties of *Quinizarin*, which was dissolved in *Elbesil* oil. Black solid line: absorption spectrum. Red dashed line: emission spectrum for excitation at 450 nm (blue dotted line).

The fluorescent dye *Quinizarin* from *Sigma-Aldrich* was dissolved in the *Elbesil* oils. *Quinizarin* is an organic compound derived from *Anthroquinone* and frequently used to color, e.g., gasoline and heating oils. Both the absorption spectrum of the *Quinizarin* as well as its emission spectrum for the excitation at 450 nm, which is the only excitation wavelength used throughout the present study, are plotted in Figure 3.3b. The absorption spectrum was recorded with a *Lambda 750 UV/Vis/NIR* spectrophotometer from *PerkinElmer*. The emission spectrum was measured with a *Cary Eclipse* fluorescence spectrophotometer from *Agilent*. The data of both spectra were recorded in steps of 0.5 nm.

3.2. Experimental setups

3.2.1. Flow rate

The overall volume flux $\dot{V}$ of the flow was measured by an ultrasonic flow meter type *Deltawave C* from *Systec controls* with a maximum error of 0.2 l/min. The flow meter was mounted on the pipe between the bypass and the inflow tank as illustrated in Figure 3.1. The measurements of the ultrasonic flow meter were spot-checked with an analog flow meter type *RW-RD 40* from *Aqua Metro*, which was temporarily installed at the outflow of the channel.

The three-dimensional flow rate $\dot{V}$ was measured to determine the Reynolds number [15]

$$Re = \frac{h_n u_{s,n}}{\nu} = \frac{3\dot{V}}{2\nu b_c} \tag{3.2}$$

of the corresponding Nusselt flow [13] with the parabolic velocity profile $\vec{u}(z)$, the film thickness h_n and the free surface velocity $u_{s,n}$ given as

$$\vec{u}(z) = \frac{g\sin\alpha}{2\nu}(2h_n - z)z\vec{e}_x, \qquad h_n = \sqrt[3]{\frac{3\nu\dot{V}}{g{b_c}\sin\alpha}}, \qquad u_{s,n} = \sqrt[3]{\frac{9\dot{V}^2 g\sin\alpha}{8\nu {b_c}^2}}. \tag{3.3}$$

The definition (3.2) of the Reynolds number is only valid for the film flow over a flat incline without sidewalls, where the two-dimensional flow rate $\dot{q} = \dot{V}/b_c$ is independent of the spanwise y-coordinate and the characteristic length and velocity can be calculated analytically from the Navier-Stokes equations as given in equation (3.3).

When sidewalls or undulated topographies are present, multiple length scales and velocities are involved. For films over flat inclines which are bounded by sidewalls, the no-slip condition at the sidewalls gives rise to a variation of the flow's velocity in the crosswise y-direction. Please

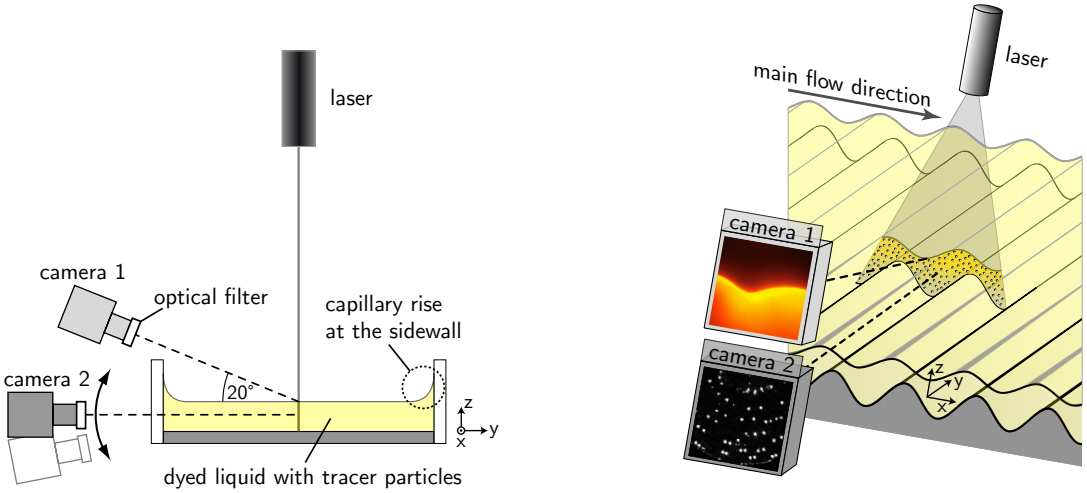

Figure 3.4.: Experimental setups for the measurements of the free surface shape (Section 3.2.2) and the flow field structure (Section 3.2.3) of the film flow. The free surface was illuminated by a blue diode laser and recorded by camera 1. The streamlines were visualized by a red diode laser and recorded by camera 2. The velocity field was measured by particle image velocimetry (PIV). The PIV system consisted of a pulsed Nd:YAG laser and camera 2. For the single particle tracking measurements a red diode laser illuminated the tracer particles in the fluid, which where then recorded by camera 2. The inclination of camera 2 against the y-direction was adaptable. Modified and reprinted with permission from [110]. © AIP Publishing

see Figure 1.16 and Haas *et al.* [67] for the influence of the sidewalls on the flow rate and the cross-sectional velocity field in films over flat inclines. For films flowing down undulated topographies, the local film thickness $h_0(x)$ and the local free surface velocity $u_s(x)$ of the steady-state flow vary in x-direction and, if sidewalls are present, additionally in y-direction. To the author's knowledge, there are no studies similar to [67] for films flowing over undulated topography. Hence, due to the lack of a better definition of the Reynolds number, which is globally valid for both film flow over flat and undulated inclines, the Reynolds number defined in equation (3.2) was used throughout this study to characterize the ratio of inertial forces to viscous forces.

3.2.2. Free surface shape

The description of the experimental techniques presented in this section relies on the publications by Schörner *et al.* [76, 110] and Dauth *et al.* [122].

Steady-state flow

The free surface $h_0(x)$ of the steady-state flow was detected with the experimental setup sketched in Figure 3.4. To portray $h_0(x)$, the fluorescent dye *Quinizarin* was dissolved in the *Elbesil* oils. Please see Section 3.1.1 for the liquids and Section 3.1.4 for the dye properties. The *Quinizarin* was excited in the x-z-plane at the center of the channel in y-direction by a blue line laser type *FP-L-450-40P-10-F210* from *Laser Components*. In order to obtain a narrow laser line of the width[1] 0.3 mm and a length of 44 mm at the free surface of the flow, the laser

[1] All line lasers used for the present thesis exhibited a Gaussian intensity distribution in y-direction. The full width at half maximum of this intensity distribution was taken as a measure to quantify the line width.

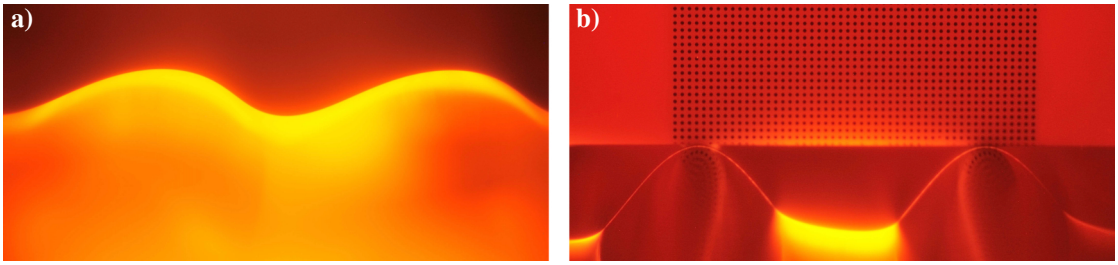

Figure 3.5.: (a) Exemplary image of the steady-state free surface of the flow over a sinusoidal topography. The example corresponds to *Elbesil 65*, *Sin*, $A = 8\,\mathrm{mm}$, $L = 20\,\mathrm{mm}$, $\alpha = 8°$ and $Re = 20$. (b) The ceramic calibration plate that was used to correct the perspective distortion of the recorded images.

was mounted 25 cm above the free surface. The output power of the continuous laser emission was 40 mW at the central wavelength 450 nm.

A *Nikon D700* camera with a spatial resolution of 11 μm/pixel recorded the fluorescing fluid and the dark air above (camera 1 in Figure 3.4). An optical longpass filter with a 50% cut-off wavelength of 550 nm was mounted to the *D700* to block the laser light scattered at the substrate. Please find an exemplary image of the free surface recorded for the flow over a sinusoidal topography in Figure 3.5a. The *D700* was inclined with respect to the y-axis by 20° to circumvent the capillary rise at the sidewalls. The calibration plate shown in Figure 3.5b was recorded with the same camera and served as a reference to correct the resulting perspective distortion for each acquired image of the free surface.

An edge-detection algorithm provided by *Labview* localized the interface between the bright fluid and the dark air, which is the free surface $h_0(x)$, i.e. the upper boundary of the flowing domain. The detection of $h_0(x)$ was similar to precedent approaches, e.g., Schörner *et al.* [76]: The recorded images were converted to gray scale and a Gaussian filter was applied to each image to eliminate high frequency noise (Figure 3.6a). For each pixel column of the resulting image, the brightness distribution was read out as shown exemplarily in Figure 3.6b and its first derivative was calculated (see Figure 3.6c). The pixel coordinate of the maximum of the brightness distribution was allocated to the corresponding position in the real-world x-z-coordinate system with the help of the above-mentioned calibration plate type *59-210/00037* from *Max Levy* (see Figure 3.5b). This position was defined as the location of the free surface $h_0(x)$ of the steady-state flow. Subsequently, a Fast Fourier Transformation was performed to

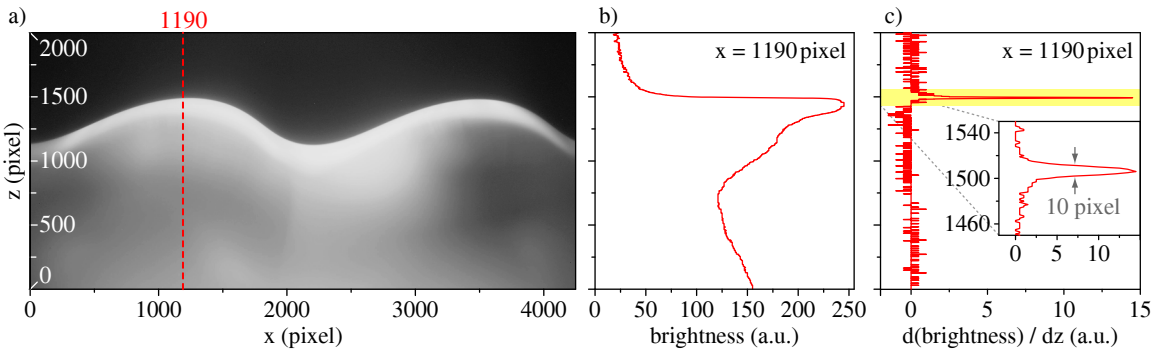

Figure 3.6.: Localization of the steady-state free surface of the flow. For the pixel column highlighted by a red vertical line in the exemplary image (a), the brightness distribution and its first derivative are plotted in (b) and (c). The maximum of the brightness distribution was defined as the location of the steady-state free surface $h_0(x)$.

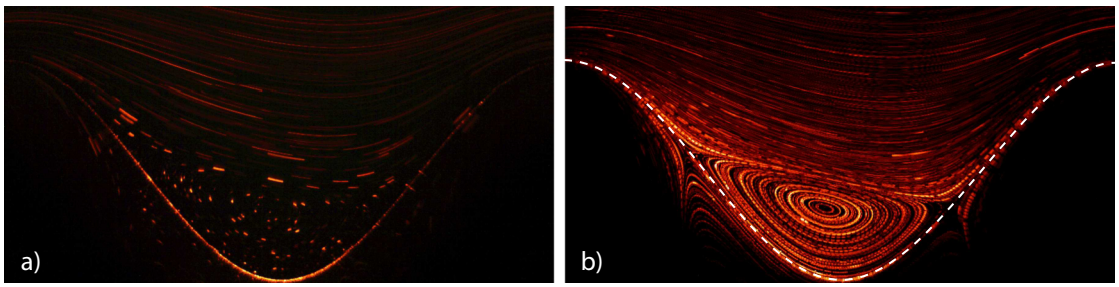

Figure 3.7.: Illustration of the method used to reconstruct the streamline patterns. About 50 individual images (a) were superimposed to yield the streamline pattern (b). The lower bright sinusoidal line in (a) and the dashed line in (b) correspond to the bottom contour. The dots and lines below the bottom contour are reflections of the particles at the bottom. The example corresponds to *Elbesil 145*, *Sin*, $A = 8$ mm, $L = 20$ mm, $\alpha = 10°$ and $Re = 14$.

receive the average film thickness h_{av} as well as the first and the second harmonic amplitudes a_1 and a_2 of the steady-state free surface.

Time-dependent flow

To record the time-dependent free surface $h(x,t)$ the experimental setup for the detection of the steady-state free surface $h_0(x)$ was slightly modified by exchanging the camera and the laser. All other components of the setup and the post processing of the acquired images remained unchanged. The *Nikon D700* was replaced by a high-speed camera type *CR600x2* from *Optronis*, which was mounted in exactly the same way. The frame rate was set to 200 frames per second and the spatial resolution in the x-z-plane at the channel's center, where all measurements were performed, was about 20 μm/pixel. Besides, the *FP-L-450-40P-10-F210* line laser was replaced by two brighter *FP-MVmicro-450-70-10* line lasers, also from *Laser Components*, which each provided a continuous laser emission of 70 mW at the central wavelength 450 nm. The two laser lines were overlaid to obtain a higher fluorescence intensity of the *Quinizarin*, necessary due to the short exposure times of the *CR600x2* high-speed camera.

3.2.3. Flow field structure

The description of the experimental techniques presented in this section relies on the publications by Schörner *et al.* [76, 110] and Dauth *et al.* [122].

Streamlines

The streamlines of the steady-state flow were visualized by portraying the scattering light of tracer particles in the fluid. Please see Section 3.1.4 for the properties of the tracer particles. The particles were illuminated by a red line laser from *Laser Components* type *FP-L-635-30P-10-F210*, whose laser sheet was aligned parallel to the x-z-plane at the channel's center. In order to obtain a narrow laser line of the width 0.3 mm and a length of at least 44 mm within the film, the laser was mounted 25 cm above the free surface of the flow. A CMOS camera type *DBK 61BUC02* from *IC Imaging* with a spatial resolution of 22 μm/pixel was mounted parallel to the y-axis and collected the light scattered at the particles (camera 2 in Figure 3.4). To obtain the streamline pattern, about 50 individual pictures (Figure 3.7a) à 0.1 s exposure time were superimposed (Figure 3.7b). Spatial calibration of the images was achieved with a calibration plate as described in Section 3.2.2 for the free surface measurements. With the streamlines so

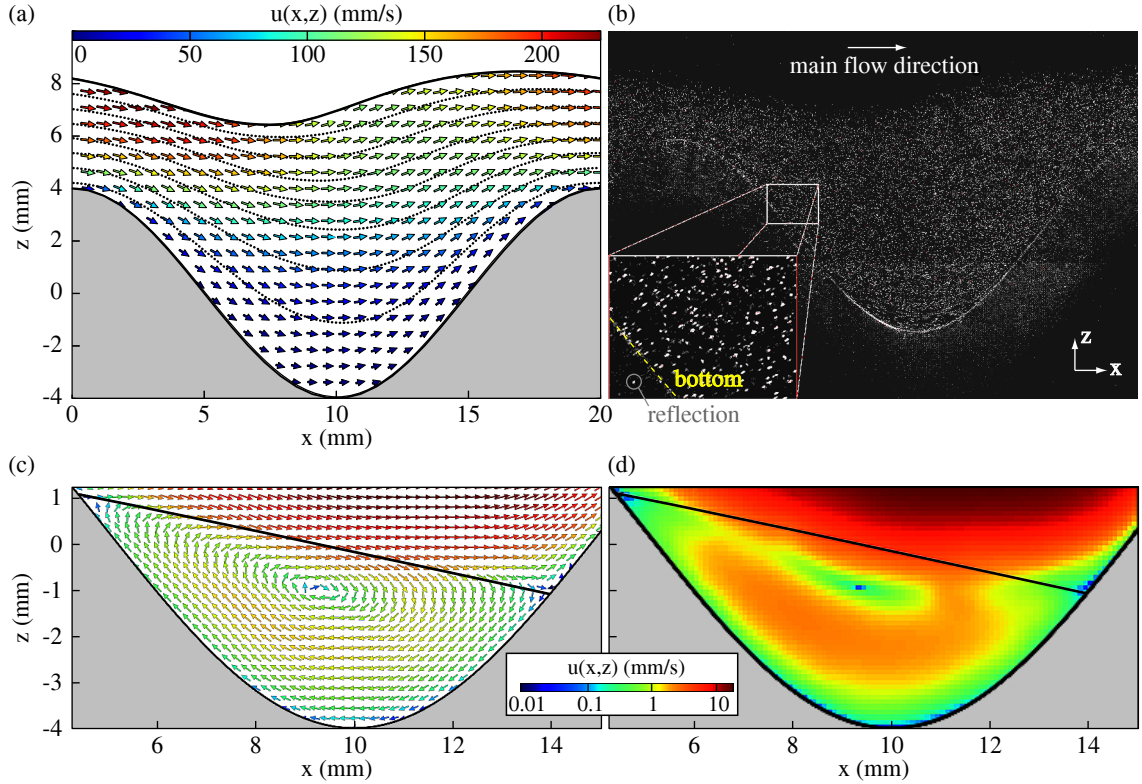

Figure 3.8.: (a) Example of the steady-state velocity field of the main flow, revealed by particle image velocimetry (PIV) and reduced to about 4 vectors/mm^2 for clarity. The dotted black lines indicate the streamlines. (b) Exemplary image of the raw data of (a) with bright tracer particles. In the inlay, the bottom contour of the topography (yellow dashed line) and the reflection of a tracer particle at this contour are highlighted. (c), (d) Example of the steady-state velocity field in the troughs, revealed by PIV. The bold black line is the separatrix between the eddy and the overlying main flow, determined from the streamline pattern. While (c) shows the vector field, reduced to about 30 vectors/mm^2 for clarity, (d) illustrates the absolute value of the steady-state velocity $u(x, z)$. The examples correspond to *Elbesil 145*, *Sin*, $A = 8\,\text{mm}$, $L = 20\,\text{mm}$, $\alpha = 10°$, and $Re = 7$ in (a) and (b), and $Re = 14$ in (c) and (d).

obtained, the separatrix between the recirculating areas in the topography's troughs and the flowing domain above could be determined by visual judgment with an accuracy of $\pm 0.1\,\text{mm}$. Together, the separatrix and the solid substrate constitute the lower boundary $f_0(x)$ of the flowing domain of the steady-state flow.

Velocity field

The steady-state velocity field $\vec{u}(x, z)$ at the channel's centerplane was revealed by particle image velocimetry (PIV). The PIV system consisted of a pulsed laser, a camera and an *Arduino* microcontroller, which synchronized both. The Nd:YAG line laser of type *Solo II-15* from *New Wave* was aligned in the x-z-plane at the center of the channel in y-direction and illuminated the fluid with the entrained tracer particles. Please see Section 3.1.4 for the properties of the tracer particles. The monochrome CCD camera type *DMK 41BU02/72BUC02* from *The Imaging Source* recorded the light scattered at the particles with a spatial resolution of $10\,\mu\text{m/pixel}$ (camera 2 in Figure 3.4). The camera could be inclined slightly against the y-direction to circumvent the distortions near to the free surface, provoked by the capillary rise at the sidewalls. The recorded frames were split into interrogation windows, which overlapped each other. A displacement vector was calculated for each window, either with an autocorrelation technique

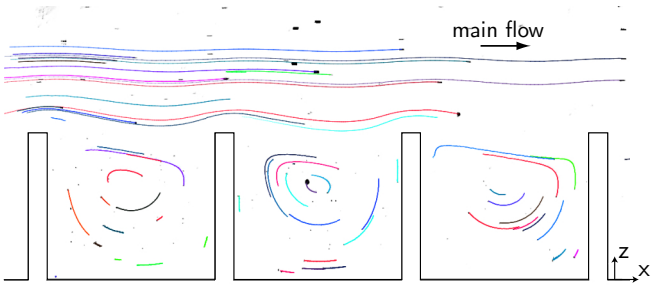

Figure 3.9.: Example image with tracer particles (black dots), overlaid with particle trajectories (colored lines). The contour of the rectangular topography with $A = 8\,\mathrm{mm}$, $L = 10\,\mathrm{mm}$, $W = 1\,\mathrm{mm}$, $\alpha = 10°$ is shown as a black line. The liquid was *Elbesil 100*. Reprinted with permission from [122]. © AIP Publishing.

for the flowing film or a cross-correlation technique for the recirculating areas in the troughs of the topography. The vector field so obtained had a density of at least $100\,\mathrm{vectors/mm^2}$. Please see Figure 3.8a for an example of the measured steady-state velocity field and Figure 3.8b for an exemplary image of the corresponding raw data.

When the steady-state velocity fields of the eddies in the troughs were measured, the distance between the camera and the channel was reduced and both the spatial resolution and the density of the vector field increased. Please see Figure 3.8c for an example of the measured steady-state velocity field $\vec{u}(x, z)$ when an eddy is present and Figure 3.8d for the corresponding absolute value $u(x, z) = |\vec{u}(x, z)|$.

Spatial calibration of the acquired data was carried out with the calibration plate described in Section 3.2.2. The accuracy of the measured velocity field $\vec{u}(x, z)$ of each steady-state flow configuration was improved by averaging the results over at least 400 experimental runs. With these data in the fold, the local free surface velocity of the steady-state flow $u_s(x) = |\vec{u}(x, h_0(x))|$ and, by averaging along one period of the topography's wavelength, the corresponding mean free surface velocity $\bar{u}_s$ could be determined.

Single particle tracking

Besides detecting the streamlines as described previously, the flow pattern in the x-z-plane at the center of the channel was also visualized by single particle tracking (SPT) measurements. Both the steady-state flow and the flow that was perturbed by traveling free surface waves were considered with this experimental technique. The respective setup is shown schematically in Figure 3.4. An *Optronis CR600x2* high-speed camera (camera 2 in Figure 3.4), a 110 mW laser light sheet created by *FP-L-635* line lasers from *Laser Components* and the nearly neutrally buoyant tracer particles described in Section 3.1.4 were used. The central emission wavelength of the laser was 635 nm. The light sheet had a width of about 0.5 mm in y-direction and lay in the x-z-plane at the center of the channel to illuminate the entrained particles there. The camera was aligned parallel to the y-axis and collected the light scattered at the particles through the transparent sidewalls. At each experimental run, 5000 images with a resolution of at least $40\,\mu\mathrm{m/pixel}$ were recorded. The frame rate was set to 900 frames per second.

The acquired data were post-processed with a SPT technique based on the widely used Crocker-Grier algorithm [123], implemented and extended according to *Python Trackpy* [124]. In a nutshell, the individual particles were first localized with sub-pixel accuracy in each image and then the particle coordinates of subsequent images were linked to a trajectory. Finally, the spatial calibration in real-world coordinates was achieved with the help of the ceramic

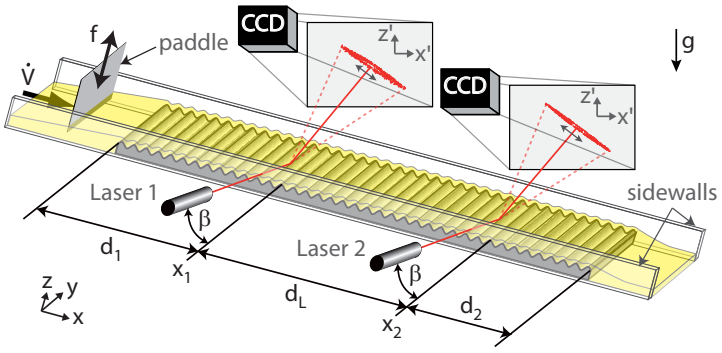

Figure 3.10.: Experimental setup for the measurements of the convective free surface instability. Modified and reprinted with permission from [76]. © AIP Publishing.

calibration plate shown in Figure 3.5b. An example image with tracer particles and their trajectories is shown in Figure 3.9 for the steady-state flow over a rectangular topography.

3.2.4. Linear stability

The linear convective free surface instability of the film flow was carefully analyzed with an experimental technique related to previous approaches, e.g., [87,97,107,118]. The measurements were carried out in all three channels (see Section 3.1.2) with the setup shown in Figure 3.10. A paddle was mounted close to the inflow of the channel, upstream of the topography. The paddle was tight-fitting concerning the channel's width and permanently dipped into the liquid. The paddle oscillated continuously in the z-direction with an amplitude of $A_e = 0.5\,\mathrm{mm}$ or below, either driven by a stepping motor type *DC BCI 52.60* from *EBM Papst* or by a *E1250-IP-UC/V1RE* linear motor device from *LinMot*. That way, the volume flux $\dot{V}$ of the steady-state channel flow was periodically varied and small, time-periodic, traveling free surface waves of a frequency between $0.9\,\mathrm{Hz} \leq f \leq 15.0\,\mathrm{Hz}$ and an amplitude $a < 0.1\,\mathrm{mm}$ [122, 125] were imposed to the free surface of the flow. In good approximation, these waves can be considered as linear free surface disturbances [114, 122, 125].

In order to determine whether the disturbances were amplified or damped on their way downstream, the resulting time-dependent free surface amplitude of the traveling wave was probed at the two different positions x_1 and x_2 in streamwise direction (see Figure 3.10). Either two He-Ne lasers type *1507-0* from *JDS Uniphase* or two diode lasers type *FP-D-635-5-C-F* from *Laser Components* were used. The lasers were aligned parallel to each other in the y-z-plane with an inclination of $\beta = (20 \pm 2)°$ against the y-axis. The laser beams hit the free surface at the center of the channel over the middle of a crest of the topography with an accuracy of $\pm 0.5\,\mathrm{mm}$. Both laser beams were reflected at the free surface and reached a screen after an optical path length of at least 3 m. Whenever a traveling free surface wave passed the reflection points, the laser spots oscillated on the screen with an amplitude proportional to the amplitude of the traveling linear free surface wave at the respective position in streamwise direction. More precisely, the oscillation amplitude of a laser spot on the screen was proportional to the maximum slope $2\pi a/\lambda$ of the free surface contour of the traveling wave at the respective position x_i. Hence, the oscillation amplitude on the screen can be taken as a measure for the amplitude a of a linear, traveling free surface wave of the wavelength λ [118].

A CCD camera type *DMK 31BU03* from *IC Imaging* recorded 512 images of each laser spot on the screen at a frame rate of 30.0 Hz. A Gaussian filter was applied to each picture to reduce

image noise and the threshold was set to 80% of the brightest pixel of each image to obtain a sharp-edged spot. The center of the area of each oscillating sharp-edged spot was determined and calibrated in space to ensure that the results were not affected by the perspective distortion of the views of the cameras or a slightly differing distance of the two cameras to the screen. In the coordinate system x'-z' of the screen (indicated in the inlays in Figure 3.10) the laser spot positions were denoted as

$$\mathbf{p}_i(t) = (p_{x',i}(t), p_{z',i}(t)), \quad i = \{1, 2\}. \tag{3.4}$$

Please see Figure 3.11a for a typical example of the recorded pathlines $\mathbf{p}_i(t)$ and Figure 3.11b for an excerpt of the x'- and z'-components of the time-dependent laser spot positions. Subsequently, the Fourier transformed signals

$$\hat{\mathbf{p}}_i(f') = \left(\hat{p}_{x',i}(f'), \hat{p}_{z',i}(f')\right) = \left(\mathcal{F}(p_{x',i}(t)), \mathcal{F}(p_{z',i}(t))\right) \tag{3.5}$$

and their absolute values

$$\hat{p}_i(f') = \sqrt{\hat{p}_{x',i}{}^2(f') + \hat{p}_{z',i}{}^2(f')} \tag{3.6}$$

were calculated as described by Pollak *et al.* [118]. Please see Figure 3.11c for an example of the absolute values $\hat{p}_i(f')$ of the two-dimensional Fourier transformed signals $\hat{\mathbf{p}}_i(f')$. The dominant peak corresponds to the fundamental excitation frequency f of the paddle. The peaks due to higher harmonics or external noise sources are about two orders of magnitude smaller than the dominant peak. Hence, the shape of the traveling free surface wave was mainly sinusoidal with the fundamental frequency f of the paddle.

A Gaussian fit was applied to the main peak of the Fourier transformed signals $\hat{p}_i(f')$ and the amplitudes B_i of the Gaussian fits were extracted. The amplitudes B_i were proportional to the amplitudes of the traveling free surface waves at the positions x_i in streamwise direction. In the experiments, the whole Reynolds number and frequency range considered was scanned with small steps of both Re and f. At each measurement point (Re, f), the free surface amplitudes a of the traveling waves, i.e. the amplitudes B_i of the respective Gaussian fits, were evaluated. In the present and in previous studies (e.g. [118]), the difference $\Delta B = B_2 - B_1$ was used to compare the wave amplitudes at the positions x_i. If a wave was amplified in streamwise direction ($\Delta B > 0$), the flow of the Reynolds number Re was denoted as convectively unstable against the free surface perturbation of the respective frequency f. In the opposite case, when the wave was damped in streamwise direction, the flow was denoted as stable ($\Delta B < 0$). Stable and unstable regimes in the stability chart are separated by the neutral curve, where $\Delta B = 0$. As an experiment only hit a neutral point by fortuity, the neutral curve was determined by a linear interpolation of the neighboring measurement points: either f was kept fixed and Re was varied or vice versa. That way, the neutral points were determined with a precision of ± 0.2 Hz and $\pm 0.5 Re$.

Besides the binary information on the stability of the flow provided by the above-mentioned experiments, the grade of the flow's (in)stability deep inside the stable and unstable flow regimes was determined in order to unveil the inner topology of the stability charts [110]. This approach was based on the results of precedent studies which showed that linear free surface waves, propagating along flat [87] or wavy inclines [125], grow exponentially in streamwise direction. The exponential growth rate b of the amplitude of a linear free surface wave was defined as

$$b = \frac{1}{x_2 - x_1} \ln \frac{B_2}{B_1}. \tag{3.7}$$

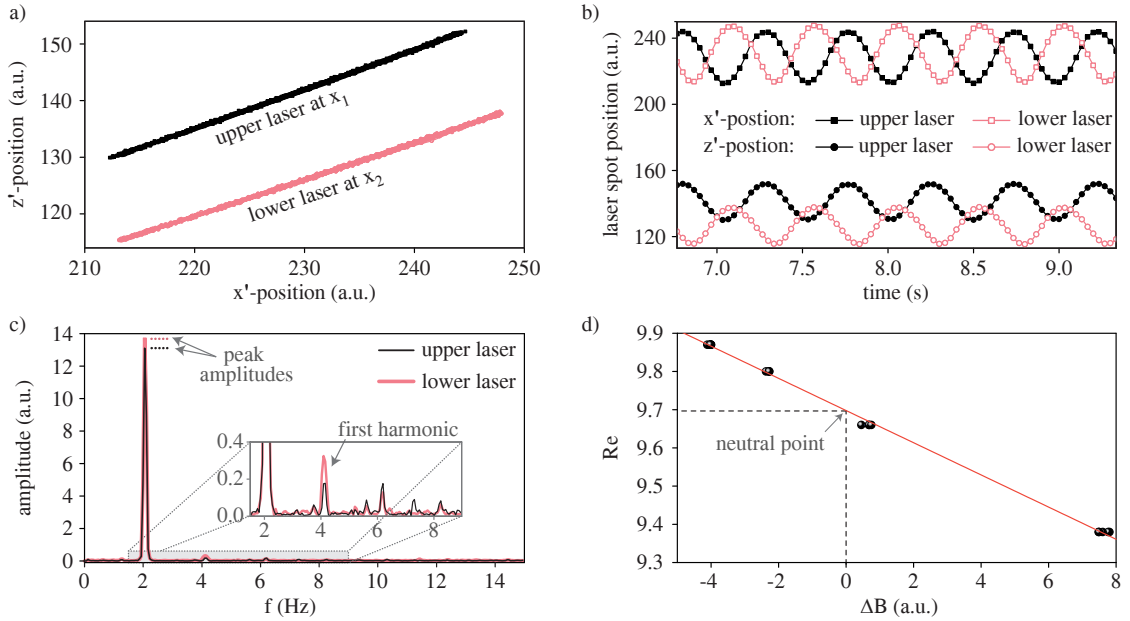

Figure 3.11.: (a) Positions of the spots of the upper laser (black) and the lower laser (rose) on the screen. (b) Excerpt of the x'- and z'-components of the time-dependent positions (a) of the laser spots. (c) Absolute values of the Fourier transformed signals of the laser spots of the measurement shown in (a) and (b). (d) Dependence of the amplitude difference ΔB on the Reynolds number. The example shown in (a) - (d) corresponds to *Elbesil 145*, *Rec*, $A = 8\,\mathrm{mm}$, $L = 20\,\mathrm{mm}$, $W = 1\,\mathrm{mm}$ and $\alpha = 21°$. In (a) - (c), $Re = 9.66$ and $f = 2.05\,\mathrm{Hz}$. In (d), the Reynolds number was varied while $f = 2.05\,\mathrm{Hz}$ and all other system parameters were kept constant.

The neutral curve is represented by $b = 0$ in this notation. A two-dimensional linear interpolation of the measured growth rates connected the densely settled measurement points in the Re-f-plane.

The distances d_1 and d_2 (see Figure 3.10) were chosen according to preliminary experiments [107] to exclude inflow and outflow effects. During all measurements, only small traveling waves with a ratio $\kappa = a/\lambda$ of the perturbation's amplitude a to its wavelength λ smaller than $\kappa = 0.01$ were considered [118]. Additionally, the wave's amplitude never exceeded 2% of the steady-state flow's local film thickness. For measurements which were performed deep inside the unstable flow regime, the distance d_L between the two lasers was gradually decreased until the criterion $\kappa \leq 0.01$ was fulfilled. The results so obtained were counter-checked to ensure that the measurements were not corrupted by an insufficient distance d_L. Yet $\kappa \leq 0.01$, all physical experiments deal with perturbations of non-vanishing amplitude $a \neq 0$. This constitutes a fundamental difference to the theory of linear disturbances with $a = 0$ in the computations [113] and gives rise to a slight disparity of the numerical and the experimental neutral curves [113, 125]. Besides, due to the significantly differing topologies of the stability charts, the exact value of a varied slightly between different experiments, even though $\kappa \leq 0.01$.

The effect of the sidewalls on the primary instability of the flow at the center of the channel can be neglected in the present study according to the findings by Georgantaki *et al.* [117] (see Figure 1.26), as the Kapitza numbers of the liquids used in the experiments were sufficiently small ($Ka < 3.8$, see Table 3.1).

4. Results and discussion

4.1. Does the topography shape matter in general for flow stability?

Controversial findings were published on the effect of the topography's specific shape on the linear stability of gravity-driven film flows over undulated inclines. On the one hand, Cao *et al.* [109] observed that the critical Reynolds number for the onset of the primary instability of film flows over a sinusoidal topography differs from the critical Reynolds number of the flow over a rectangular topography of the same amplitude and wavelength. On the other hand, Pollak and Aksel [107] found a similar stability behavior of liquid films flowing over two topographies of different specific shape, but equal corrugation amplitude and wavelength. At the specific Reynolds number $Re = 13$, they measured the flow's linear stability for both a sinusoidal topography (Figure 4.1a) and the same sinusoidal topography, modified by replacing the eddies, which formed in the troughs at $Re = 13$, by a solid contour (Figure 4.1b). Surprisingly, the flow over the two different topographies showed the same stability characteristics at this particular Reynolds number.

The above-mentioned controversial findings triggered a fundamental question, considered in the present Section 4.1: does the topography's specific shape matter in general for the linear stability of gravity-driven film flows? In order to understand this complex problem, the topography's specific shape was varied while all other parameters of the system were retained as described in Section 4.1.1. Experiments on the flow's linear stability were carried out (Section 4.1.2) and related to measurements of the flow field and the free surface contour of the basic flow (Section 4.1.3). That way, insights into how the topography's specific shape can manipulate both the linear stability and the basic flow of gravity-driven films were obtained (Section 4.1.4).

The present Section 4.1 relies on the publication *"Does the topography's specific shape matter in general for the stability of film flows?"* from Schörner *et al.* [76].

4.1.1. Measured parameter space

The experiments have been carried out with the liquid *Elbesil 145* flowing over undulated substrates placed in channel 1, which was inclined by $\alpha = 10°$ against the horizontal. Please

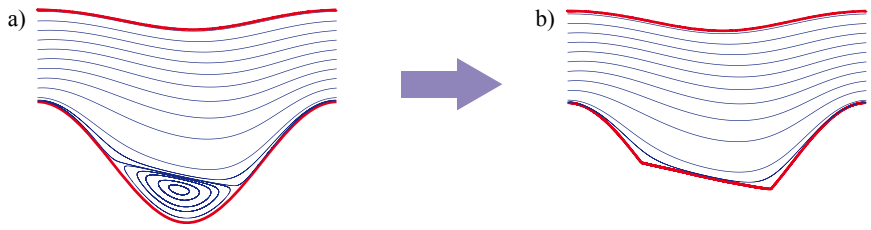

Figure 4.1.: (a) Sinusoidal topography and (b) the same topography, modified by replacing the eddy in the trough by a solid contour. The streamlines correspond to $Ka = 1.279$ and $Re = 13$. Reprinted with permission from [107]. © AIP Publishing.

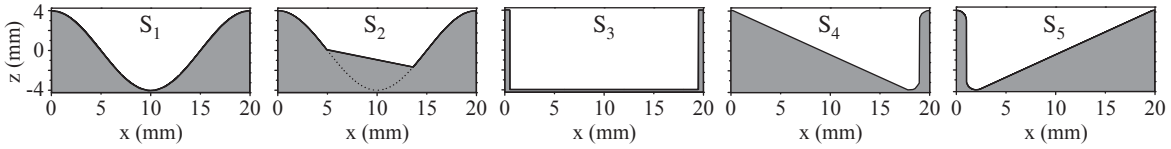

Figure 4.2.: Topographies S_1 - S_5. Modified and reprinted with permission from [76]. © AIP Publishing.

see Section 3.1.1 for the physical properties of the liquid, Section 3.1.2 for a description of the flow facilities including channel 1, and Section 3.1.3 for remarks on the substrate topographies. In order to unveil whether the topography's specific shape matters in general for the stability of film flows five differently shaped substrates were used in the experiments. All substrates were periodically corrugated in streamwise direction with the amplitude $A = 8.0\,\mathrm{mm}$ and the wavelength $L = 20.0\,\mathrm{mm}$. Concerning the specific *shape* of the substrates' topography, the set of five different systems $S_1 - S_5$ shown in Figure 4.2 was used. The sinusoidal topography S_1 ($shape = Sin$) with its previously studied stability behavior [107, 108] was chosen as reference. The modified sinusoidal ($SinMod$) topography S_2 was obtained by replacing the eddies, which form in the troughs of S_1 at the Reynolds number $Re = 13$, by a solid contour. The non-smooth topography S_3 had a rectangular (Rec) shape and narrow tips of the width $W = 1.0\,\mathrm{mm}$. The topographies S_4 and S_5 exhibited identical sawtooth-like shapes, but were oriented differently against the main flow direction (S_4: Saw; S_5: $SawRev$). In contrast to S_2, the topographies $S_3 - S_5$ cannot be obtained by eddy configurations from any original topography. Hence, including the reference S_1, the above-given set consists of five arbitrary topographies.

4.1.2. Stability and basic flow measurements

Stability measurements

Recent experimental [107] and numerical [108] studies unveiled the stability characteristics of gravity-driven films flowing down the sinusoidally corrugated topography S_1 (see Figure 4.3, solid black line). The present study went beyond this first approach by measuring the linear stability charts of *Elbesil 145* flowing over the five strongly differing topographies $S_1 - S_5$ at $\alpha = 10°$. The results are shown in Figure 4.3. Surprisingly, all charts were equal, aside from small deviations. For all five topographies, a destabilization of the flow compared to the critical Reynolds number $Re_c \approx 7.1$ [79, 80] of the corresponding Nusselt flow was measured. At low

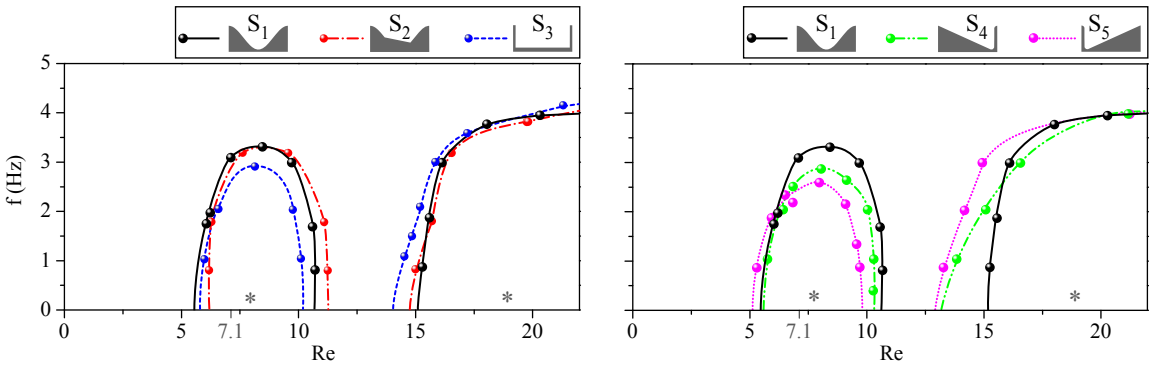

Figure 4.3.: Stability charts of the *Elbesil 145* oil for the flow over the five topographies $S_1 - S_5$ and $\alpha = 10°$. Stars indicate convectively unstable regimes. Modified and reprinted with permission from [76]. © AIP Publishing.

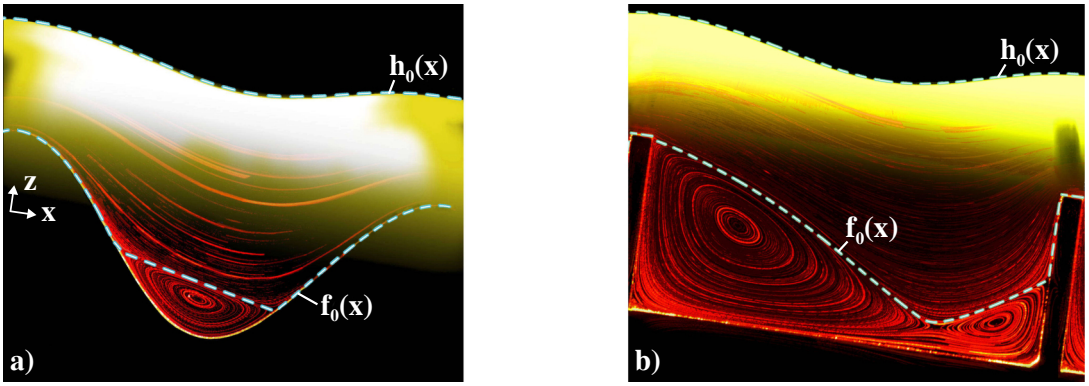

Figure 4.4.: Free surface and streamlines of the steady-state film flow of *Elbesil 145* at $Re = 12.7$ and $\alpha = 10°$ for (a) the sinusoidal topography S_1 and (b) the rectangular topography S_3. The boundaries $h_0(x)$ and $f_0(x)$ of the flowing domain are highlighted by dashed lines. Modified and reprinted with permission from [76]. © AIP Publishing.

Reynolds numbers between $Re \approx 5.0$ and $Re \approx 11.5$, a separate long-wave instability isle appeared. This unstable isle was accompanied by a long-wave type instability beyond $Re \approx 14$. The two unstable flow regimes were separated by a flow configuration, which was stable against small free surface perturbations of $0.9\,\mathrm{Hz} \leq f \leq 15.0\,\mathrm{Hz}$.

Basic flow measurements

In order to understand why the specific shape of the topography has no major impact on flow stability, the upper boundary $h_0(x)$ and the lower boundary $f_0(x)$ of the flowing domain were measured for all five topographies $S_1 - S_5$ at $4.5 \leq Re \leq 22.5$. The upper boundary $h_0(x)$ corresponds to the free surface of the steady-state flow and was measured as described in Section 3.2.2. The lower boundary $f_0(x)$ consists of the solid substrate and the separatrix between the eddies in the troughs and the flowing domain above (see Figure 4.4). The lower boundary $f_0(x)$ was determined with the help of the streamline pattern as described in Section 3.2.3.

Examples of the boundaries $h_0(x)$ and $f_0(x)$ are given in Figure 4.5 for four Reynolds numbers. The five lower boundaries $f_0(S_i, x)$ of the flowing domain vary considerably for all five topographies S_i ($i = \{1, 2, 3, 4, 5\}$). This is a consequence of the dissimilar substrate shapes as well as of the eddies, which form in the troughs of the topographies. On the other hand, the five upper boundaries $h_0(S_i, x)$ of the flowing domain are, at equal Reynolds number, very similar for all steady-state flows over the strongly differing topographies $S_1 - S_5$.

4.1.3. Physical interpretation and discussion

The deviation of the free surfaces $h_0(S_i, x)$ and the lower boundaries of the flowing domains $f_0(S_i, x)$ from those of the chosen reference S_1 was evaluated. The cross-correlation of $f_0(S_i, x)$ and $f_0(S_1, x)$ was calculated as

$$K\left(f_0(S_i, x), m\right) = \frac{\sum_{x=0}^{L} f_0(S_1, x) f_0(S_i, x - m)}{\sum_{x=0}^{L} f_0(S_1, x) f_0(S_1, x)}, \tag{4.1}$$

and its maximum as

$$K_{f_0}(S_i) = max\left[K\left(f_0(S_i, x), m\right)\right]. \tag{4.2}$$

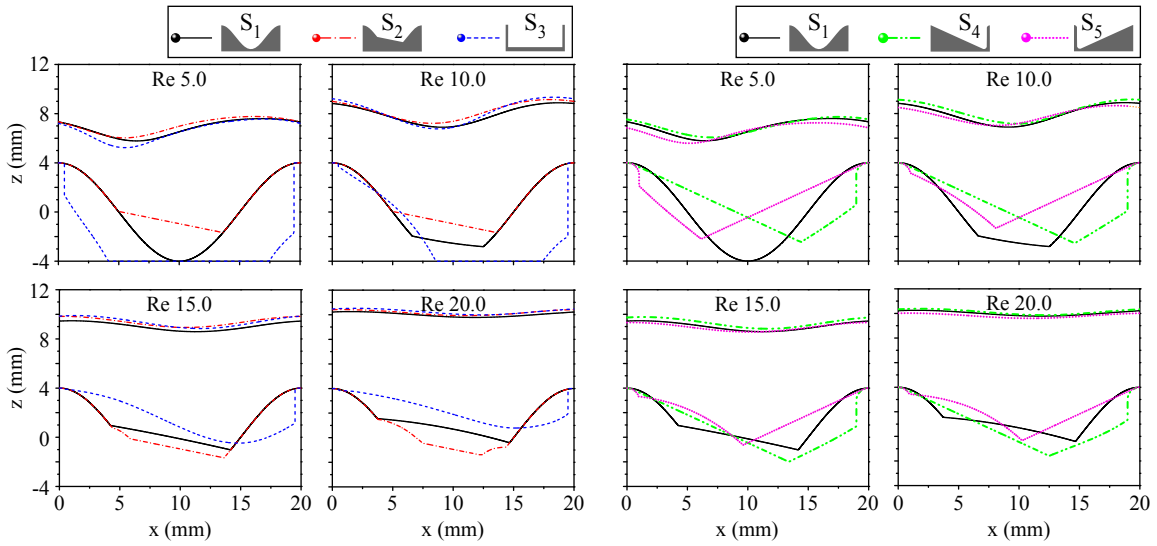

Figure 4.5.: Boundaries $h_0(x)$ and $f_0(x)$ of the flowing domains for the flow of *Elbesil 145* over the topographies $S_1 - S_5$ at four Reynolds numbers and $\alpha = 10°$. Modified and reprinted with permission from [76]. © AIP Publishing.

The deviation

$$D_{f_0}(S_i) = 1 - K_{f_0}(S_i) \tag{4.3}$$

was taken as a measure to quantify the difference between the lower boundaries $f_0(S_i, x)$ and the lower boundary $f_0(S_1, x)$ of the flow over the sinusoidal reference S_1. The deviation $D_{h_0}(S_i)$ of the upper boundaries was defined analogously. Both $D_{f_0}(S_i)$ and $D_{h_0}(S_i)$ are shown in Figure 4.6 for all five topographies $S_1 - S_5$ at Reynolds numbers $4.5 \leq Re \leq 22.5$.

The deviations $D_{h_0}(S_i)$ $(i = \{2, 3, 4, 5\})$ of the upper boundaries were found to be three orders of magnitude smaller than the deviations $D_{f_0}(S_i)$ of the lower boundaries of the flowing domain. Hence, severe changes of the topography's specific shape provoke strong variations of $f_0(x)$ but induce only modest changes to the flow's free surface $h_0(x)$ (Figure 4.5). Since we face a free surface instability, the experimental evidence for these highly similar free surfaces explains the

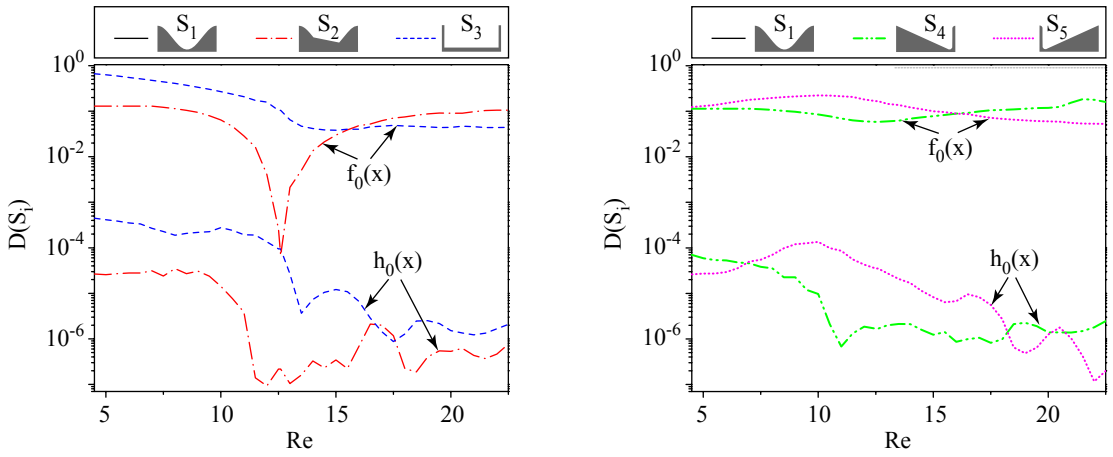

Figure 4.6.: Deviation $D(S_i)$ of the boundaries of the flowing domains over $S_1 - S_5$ of the reference flow over S_1 for *Elbesil 145* and $\alpha = 10°$. $D(S_1) \equiv 0$. Modified and reprinted with permission from [76]. © AIP Publishing.

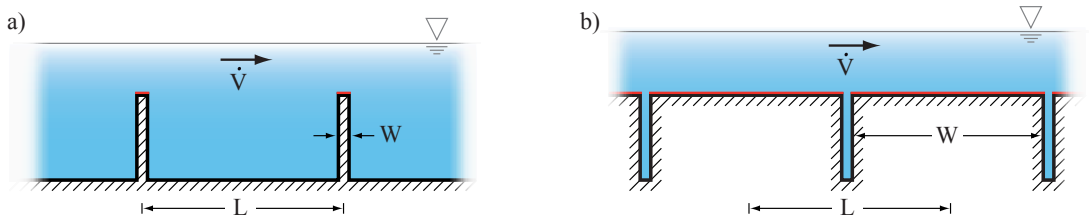

Figure 4.7.: Schematic illustration of a liquid film flowing over rectangular topographies of equal amplitude and wavelength with (a) narrow and (b) broad tips.

almost equal stability charts (Figure 4.3) despite the significantly differing topography shapes (Figure 4.2).

4.1.4. Conclusions

The stability behavior of gravity-driven films flowing over five differently shaped topographies, which shared the same amplitude and wavelength, was measured while the fluid and the inclination angle were retained. Surprisingly, all stability charts were equal, aside from small deviations (see Figure 4.3). In order to understand this astonishing finding, the upper boundary of the flowing domain, constituted by the free surface $h_0(x)$, as well as the lower boundary $f_0(x)$ of the flowing domain, defined by the substrate and the eddies in its troughs, were determined (Figures 4.4 and 4.5). The lower boundaries of the flowing domain differed decidedly for the highly diverse topographies $S_1 - S_5$. Despite this severe disparity of the lower boundaries $f_0(x)$, the free surface $h_0(x)$ and concomitant the free surface instability remained unaffected.

Are the above-mentioned findings globally valid for all topographies of equal amplitude and wavelength? Let us conduct a gedankenexperiment: for films flowing over rectangularly undulated inclines, we retain the corrugation's wavelength L and vary the tip's width W as shown schematically in Figure 4.7. For the system shown in Figure 4.7a, the no-slip condition induces high shear rates only along the narrow tips, where the local film thickness is small. Between the tips, the flow has enough space to attune freely. In contrast to this, the respective constraints imposed to the flow by the system shown in Figure 4.7b are much stricter. The no-slip condition gives rise to high shear rates within the whole flowing domain. The flow resembles to the flow over a flat incline, which features a long-wave instability beyond a critical Reynolds number. With their narrow crests, the topographies considered in the present Section 4.1 (see Figure 4.2) resemble to the system shown in Figure 4.7a. We speculate that an increase of the tip's width changes the flow's free surface and concomitant the flow's free surface stability. First indications supporting this educated guess were reported by Cao *et al.* [109] who found that for rather large tips of the width $L/2$, the critical Reynolds number differs decidedly from the one of the flow over the corresponding sinusoidal topography. A more detailed consideration of the effect of the tip width W on the linear stability of gravity-driven films is given in the following Section 4.2 and reinforces this point of view.

Notwithstanding the above, the study presented in the present Section 4.1 provides the experimental evidence that the free surface instability of gravity-driven films cannot be manipulated in general by even strong variations of the topography's specific shape. This result is of imperative importance for a wide range of technical applications like, e.g., curtain coating, where the topography's specific shape cannot be modified freely.

4.2. Stability phenomena far beyond the Nusselt flow

The stability of gravity-driven viscous films over inclined topographies was found to feature various nontrivial phenomena, which do not equally appear in the corresponding Nusselt flow over a flat incline. For example, an unstable isle can form in the flow's linear stability chart (Section 4.1). Yet, an explanation how undulated topographies provoke these phenomena was still lacking. The scope of the present Section 4.2 is to illuminate these findings and to identify their underlying effects. For this sake, the well-known Nusselt flow was asymptotically left by gradually steepening the topography, i.e. increasing the amplitude of sinusoidal undulations or decreasing the tip width of rectangular corrugations. Variations of the inclination of the channel, the viscosity of the liquid, and the wavelength of the topography followed as described in Section 4.2.1. That way, nontrivial stability charts and phenomena far beyond the limits of the Nusselt regime were revealed (Section 4.2.2). In order to understand these phenomena, the steady-state free surfaces and velocity fields of the respective flows were measured (Section 4.2.3). This comprehensive approach provided detailed experimental data on how topographies can provoke the complex shape which linear stability charts of film flows over inclined topographies can have – far beyond the Nusselt regime.

The present Section 4.2 relies on the publication *"Stability phenomena far beyond the Nusselt flow – Revealed by experimental asymptotics"* from Schörner *et al.* [110].

4.2.1. Measured parameter space

All experiments have been carried out with the liquids *Elbesil 65*, *100* and *145* flowing over undulated substrates placed in the channels 1, 2 and 3. Please see Section 3.1.1 for the physical properties of the liquids, Section 3.1.2 for an elaborate description of the channels and Section 3.1.3 for remarks on the substrate topographies.

The well-known Nusselt flow over a flat incline served as the starting point for the experiments. The flat substrate was defined either as the borderline case $A = 0$ for the sinusoidal (harmonic) topographies or as $W = L$ for the rectangular (non-harmonic) topographies. The Nusselt case was asymptotically left by either increasing the amplitude A of the sinusoidal undulations or by decreasing the tip width W of the rectangular corrugations step by step as illustrated in Figure 4.8. For the steepest topographies, variations of the inclination angle α, the liquid viscosity ν and the topography wavelength L followed. For convenience, Figure 4.8 also displays the variation of the topography's specific *shape*, considered in Section 4.1.

4.2.2. Stability measurements

Linear stability at different corrugation amplitudes

The starting point for the experiments was a film of *Elbesil 145* which flowed over an incline of $\alpha = 10\,°$. The liquid, the inclination and the wavelength $L = 20\,\mathrm{mm}$ of the sinusoidal topography were kept constant while the topography's amplitude was gradually increased from $A = 0\,\mathrm{mm}$ (flat substrate) to $A = 8\,\mathrm{mm}$ (see Figure 4.8). For each corrugation steepness, the Reynolds number was varied between $3 \leq Re \leq 22$ and the stability of the basic flow against linear free surface perturbations with $0.9\,\mathrm{Hz} \leq f \leq 8.0\,\mathrm{Hz}$ was probed. The stability charts measured at $A = \{0, 2, 4, 8\}\,\mathrm{mm}$ are shown in Figure 4.9.

In good agreement with theoretical predictions [79, 80], a long-wave type instability was found for the flow over the flat incline. The higher the topography amplitude A was, the more the

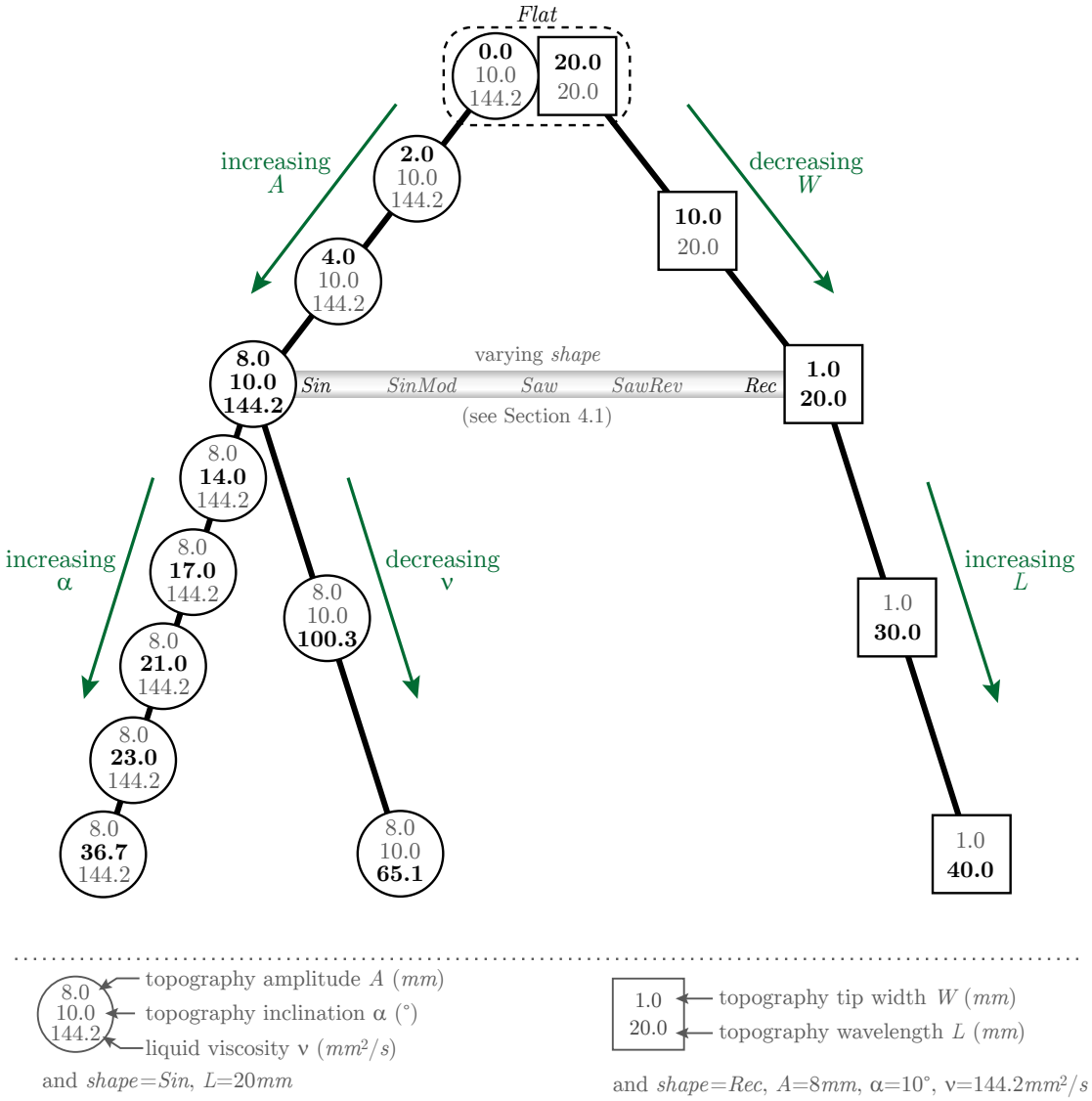

Figure 4.8.: The parameter space (A, L, W, α, ν, *shape*) that was covered by the experiments.

flow with a Reynolds number between $Re \approx 6$ and $Re \approx 11$ was destabilized against long-wave disturbances up to $f \approx 3\,\mathrm{Hz}$. Concomitant, the critical Reynolds number was reduced to $Re \approx 6$ which corresponds to a significant destabilization of the flow compared to the corresponding Nusselt flow with the critical Reynolds number $Re_c \approx 7.1$. On the other hand, the substrate corrugations stabilized the flow over the steep topographies with $A \geq 4\,\mathrm{mm}$ at Reynolds numbers between $Re \approx 11$ and $Re \approx 15$. There, the flow was stabilized the more, the steeper the corrugations were. Both the destabilizing and the stabilizing effects can clearly be attributed to the topography as they were the more pronounced, the higher the amplitude A was. Yet, it seems as if a threshold for A has to be exceeded to provoke the significant stabilization of the flow between $Re \approx 11$ and $Re \approx 15$ and the segmentation of the respective instability branch. Together, the destabilizing and the stabilizing influence of the topography give rise to the formation of the unstable isle at $A \geq 4\,\mathrm{mm}$ between $Re \approx 6$ and $Re \approx 11$, which was found previously [107, 108]. The less wavy topography with $A = 2\,\mathrm{mm}$ induced

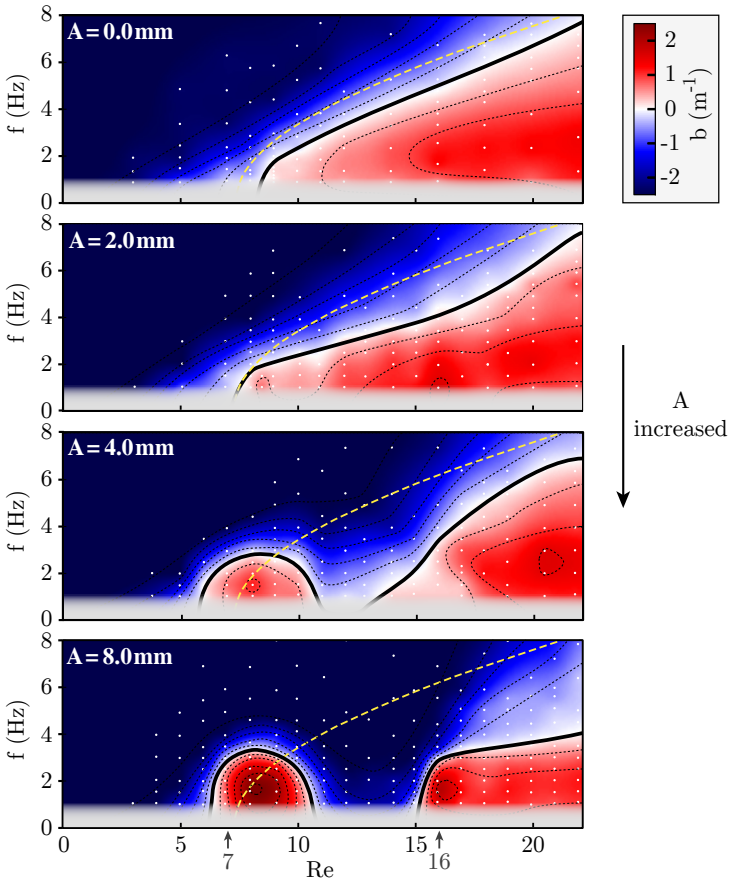

Figure 4.9.: Evolution of the linear stability chart of the *Elbesil 145* oil for $shape = Sin$, $\alpha = 10\,^{\circ}$, $L = 20\,\mathrm{mm}$ and increasing amplitude A of the topography. Measurement points are shown as white dots. Bold black lines represent the measured neutral stability curves. The yellow dashed lines indicate the theoretical neutral curve of the corresponding Nusselt flow according to a numerical solution of the Orr-Sommerfeld equation [110]. The color code visualizes the growth rates b of the free surface perturbations and the dotted contour lines are shown in steps of $0.5\,\mathrm{m}^{-1}$. Only growth rates $|b| > 2.5\,\mathrm{m}^{-1}$ were not precisely quantifiable and set to the respective values. Modified and reprinted with permission from [110]. © AIP Publishing.

only a precursor of the unstable isle without a segmentation of the stability chart: The narrow domain around $Re \approx 8$ and $f \approx 1\,\mathrm{Hz}$ has a higher growth rate b than, e.g., $Re \approx 10$, $f \approx 1\,\mathrm{Hz}$.

Linear stability at different inclination angles

Increasing the inclination α at constant liquid viscosity $\nu = 144.2\,\mathrm{mm}^2/\mathrm{s}$ (*Elbesil 145*) and fixed amplitude $A = 8\,\mathrm{mm}$ and wavelength $L = 20\,\mathrm{mm}$ of the sinusoidal topography (see Figure 4.8) provoked a dramatic change of the entire shape of the linear stability chart (see Figure 4.10). For the smallest measured inclination $\alpha = 10\,^{\circ}$, as mentioned above and reported previously [107, 108], a long-wave instability isle ranging from $Re \approx 6$ to $Re \approx 11$ appeared which was accompanied by a stable flow region from $Re \approx 11$ to $Re \approx 15$ and a long-wave instability beyond $Re \approx 15$.

Steepening α led to a growth and distortion of the unstable isle with a short-wave instability nose forming at $\alpha = 17\,^{\circ}$ and Reynolds numbers between $Re \approx 12$ and $Re \approx 15$. A further increase of α from $17\,^{\circ}$ to $21\,^{\circ}$ induced a merging of the unstable isle with the instability region

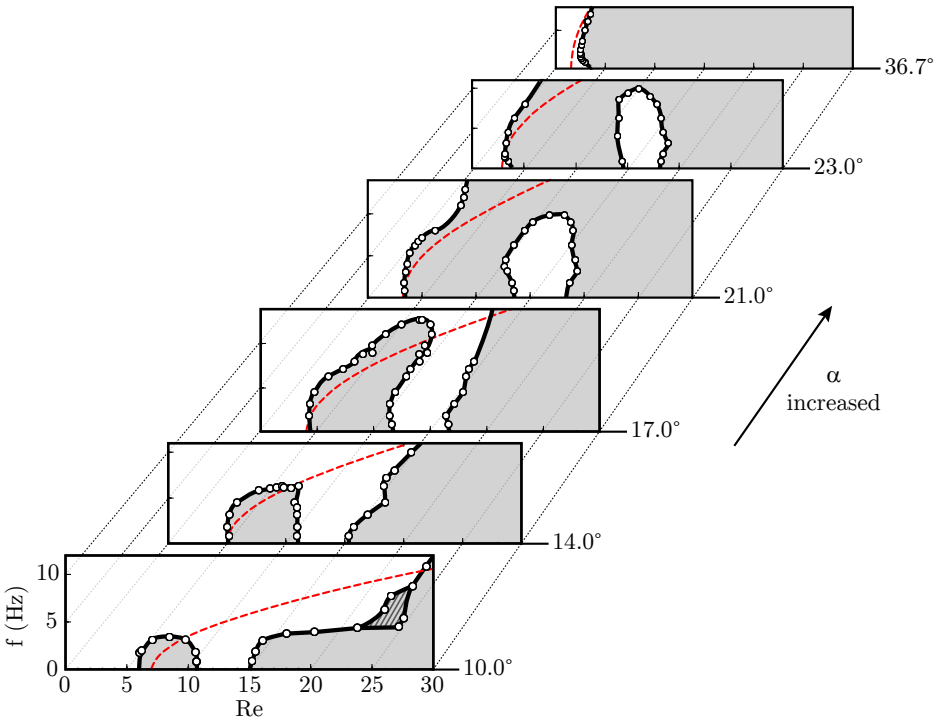

Figure 4.10.: Evolution of the linear stability chart of the *Elbesil 145* oil for *Sin*, $A = 8\,\mathrm{mm}$, $L = 20\,\mathrm{mm}$ and increasing inclination α. Convectively unstable regions are shaded. The bold black lines indicate the measured neutral curves. Hatched markings denote measurement uncertainties. The red dashed lines represent the neutral curve of the corresponding Nusselt flow according to a numerical solution of the Orr-Sommerfeld equation [110]. Modified and reprinted with permission from [110]. © AIP Publishing.

at higher Reynolds numbers. Thereby, a stable isle formed which shrank when α continued to grow and finally had disappeared at $\alpha = 36.7\,^\circ$. With regard to technical applications of film flows, the narrow Reynolds number regime between $Re \approx 15$ and $Re \approx 16$ at $\alpha = 17\,^\circ$ has to be highlighted. There, the substrate's corrugations provoke a small process window where all kinds of linear free surface perturbations are damped despite the Reynolds number being up to four times higher than $Re_c = (5/4)\cot\alpha$. A steeper inclination α led not only to a dramatic change of the entire shape of the stability chart as reported above, but also gave rise to a transition of the onset of the primary instability from long-wave type at $\alpha = 10\,^\circ$ to clearly short-wave type at $\alpha = 23\,^\circ$ and beyond. A similar phenomenon was observed by Cao *et al.* [109] for more weakly, both rectangularly and sinusoidally, undulated inclines and for a more than ten times less viscous liquid.

Linear stability at different viscosities

Figure 4.11 shows the measured evolution of the linear stability chart when the viscosity ν was decreased in two steps while the amplitude, the wavelength, and the inclination of the sinusoidal topography were retained as illustrated in Figure 4.8. As reported previously by Pollak and Aksel [107], the onset of the primary instability changes from long-wave to short-wave type with decreasing viscosity. In addition, an unstable isle was found for *Elbesil 100* and *145* and a short-wave instability nose for *Elbesil 100* above $Re \approx 15$. However, measurements beyond $Re \approx 15$ for *Elbesil 100* and $Re \approx 11$ for *Elbesil 65* were error-prone or not possible at that time.

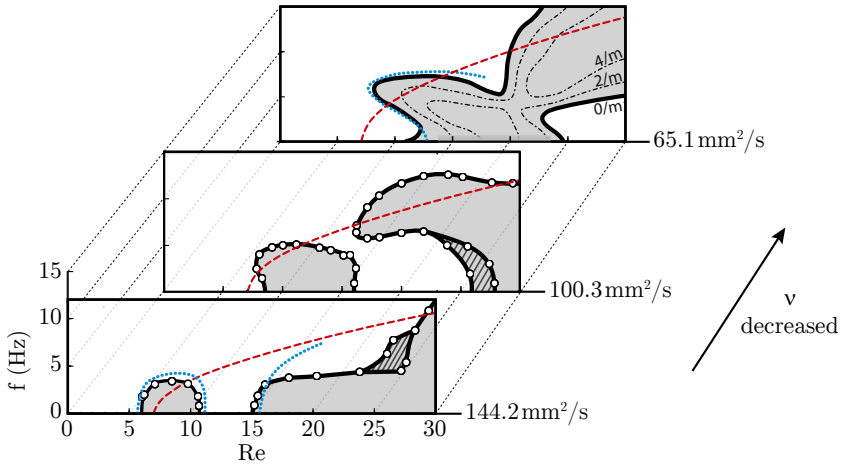

Figure 4.11.: Evolution of the linear stability chart for *Sin*, $\alpha = 10\,°$, $A = 8\,\mathrm{mm}$, $L = 20\,\mathrm{mm}$ and decreasing viscosity ν. Convectively unstable regions are shaded. The bold black lines indicate the measured neutral curves. Hatched markings denote measurement uncertainties. The red dashed lines represent the neutral curve of the corresponding Nusselt flow according to a numerical solution of the Orr-Sommerfeld equation [110]. The blue dotted lines represent numerical results by Trifonov [108]. The stability chart of the *Elbesil 65* oil contains the contour lines of the experimentally determined growth rate b of the free surface disturbances with steps of $2\,\mathrm{m}^{-1}$. Modified and reprinted with permission from [110]. © AIP Publishing.

Compared to Pollak and Aksel [107], the experimental setup was improved in the present study and allowed measurements of the flow's stability at higher Reynolds numbers and perturbation frequencies. The results so obtained provided the experimental evidence that the unstable isle indeed exists at all three viscosities $\nu = \{65.1, 100.3, 144.2\}\,\mathrm{mm}^2/\mathrm{s}$. The measurements proved that the short-wave instability nose found for the *Elbesil 100* oil can merge with the unstable isle by a further decrease of the viscosity to *Elbesil 65*. The contour lines of the measured growth rates b of the linear free surface disturbances confirm this statement (see Figure 4.11). The junction of the two instability branches led to the formation of a stable isle in the stability chart of *Elbesil 65*, where long-wave perturbations are damped far beyond the critical Reynolds number of the corresponding Nusselt flow.

Linear stability at different corrugation tip widths

As described in Section 4.2.1, the Nusselt case was asymptotically left by either increasing the amplitude of the sinusoidal undulations or decreasing the tip width of the rectangular corrugations. Now, the latter alternative is discussed. Beginning with $W = L = 20\,\mathrm{mm}$ (flat substrate) the tip width was gradually decreased to $W = 1\,\mathrm{mm}$ while the inclination $\alpha = 10°$, the amplitude $A = 8\,\mathrm{mm}$ and the wavelength $L = 20\,\mathrm{mm}$ of the rectangular topography as well as the liquid viscosity $\nu = 144.2\,\mathrm{mm}^2/\mathrm{s}$ were kept unchanged as illustrated in Figure 4.8.

The measured evolution of the linear stability chart with decreasing tip width W is shown in Figure 4.12 and resembles to the chart's evolution when the topography amplitude a is increased (please compare the Figures 4.9 and 4.12). The smaller the tip width W was, the more the flow with a Reynolds number between $Re \approx 6$ and $Re \approx 11$ was destabilized against long-wave disturbances up to $f \approx 3\,\mathrm{Hz}$. Concomitant, the critical Reynolds number was reduced to $Re \approx 6$, which corresponds to a significant destabilization of the flow compared to the corresponding Nusselt flow. On the other hand, between $Re \approx 11$ and $Re \approx 15$, the flow was stabilized the more, the sharper the tips were. Both the destabilizing and the stabilizing effects

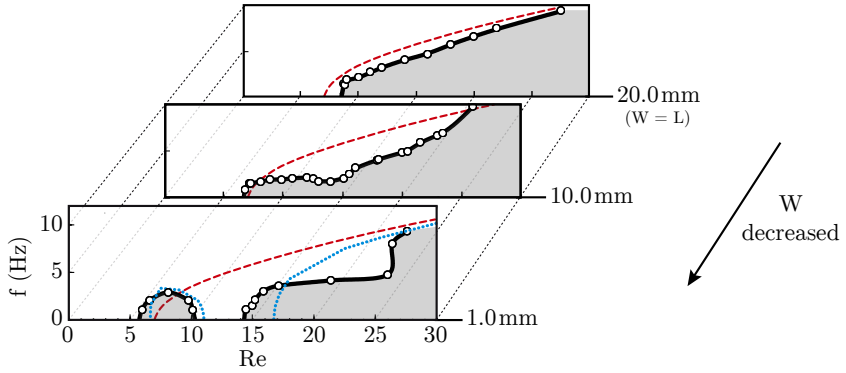

Figure 4.12.: Evolution of the linear stability chart of the *Elbesil 145* oil for Re_c, $\alpha = 10\,°$, $A = 8\,\mathrm{mm}$, $L = 20\,\mathrm{mm}$ and decreasing tip width W. Convectively unstable regions are shaded. The bold black lines indicate the measured neutral curves. The red dashed lines represent the neutral curve of the corresponding Nusselt flow according to a numerical solution of the Orr-Sommerfeld equation [110]. The blue dotted lines represent numerical results [113]. Modified and reprinted with permission from [110]. © AIP Publishing.

can clearly be attributed to the steepness of the topography as they were the more pronounced, the smaller the tip width W was. Yet, it seems as if a threshold for W has to be undershot to provoke the global stabilization of the flow between $Re \approx 11$ and $Re \approx 15$ and the segmentation of the respective instability branch. The tips with $W = 10\,\mathrm{mm}$ provoked only a 'dip' in the neutral curve at $11 \leq Re \leq 15$. This dip can be interpreted as a precursor of the unstable isle, similar to the precursor of the unstable isle which appeared in the stability chart of the moderately undulated sinusoidal topography with $A = 2\,\mathrm{mm}$ shown in Figure 4.9.

Linear stability at different corrugation wavelengths

The scheme shown in Figure 4.8 will now be completed by increasing the wavelength L of the rectangular topography at constant inclination $\alpha = 10\,°$, amplitude $A = 8\,\mathrm{mm}$, tip width $W = 1\,\mathrm{mm}$ and viscosity $\nu = 144.2\,\mathrm{mm}^2/\mathrm{s}$. The measured evolution of the linear stability chart is shown in Figure 4.13. When the topography wavelength was increased, the primary instability changed from long-wave to short-wave type. In addition, an unstable isle was found

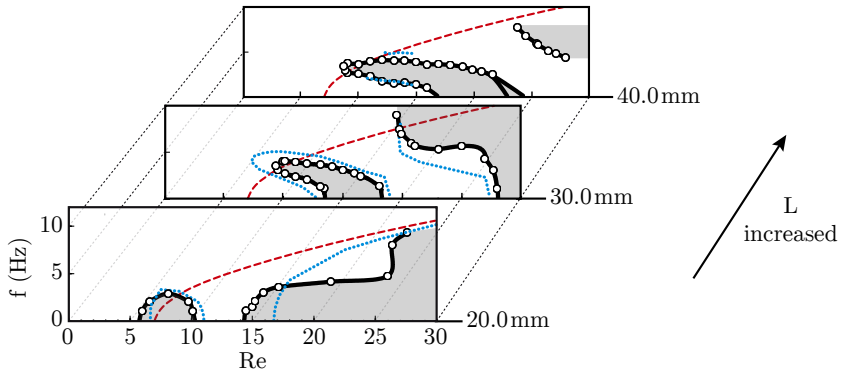

Figure 4.13.: Evolution of the linear stability chart of the *Elbesil 145* oil for Re_c, $\alpha = 10\,°$, $A = 8\,\mathrm{mm}$, $W = 1\,\mathrm{mm}$ and increasing wavelength L of the topography. Convectively unstable regions are shaded. The bold black lines indicate the measured neutral curves. The red dashed lines represent the neutral curve of the corresponding Nusselt flow according to a numerical solution of the Orr-Sommerfeld equation [110]. The blue dotted lines represent numerical results [113]. Modified and reprinted with permission from [110]. © AIP Publishing.

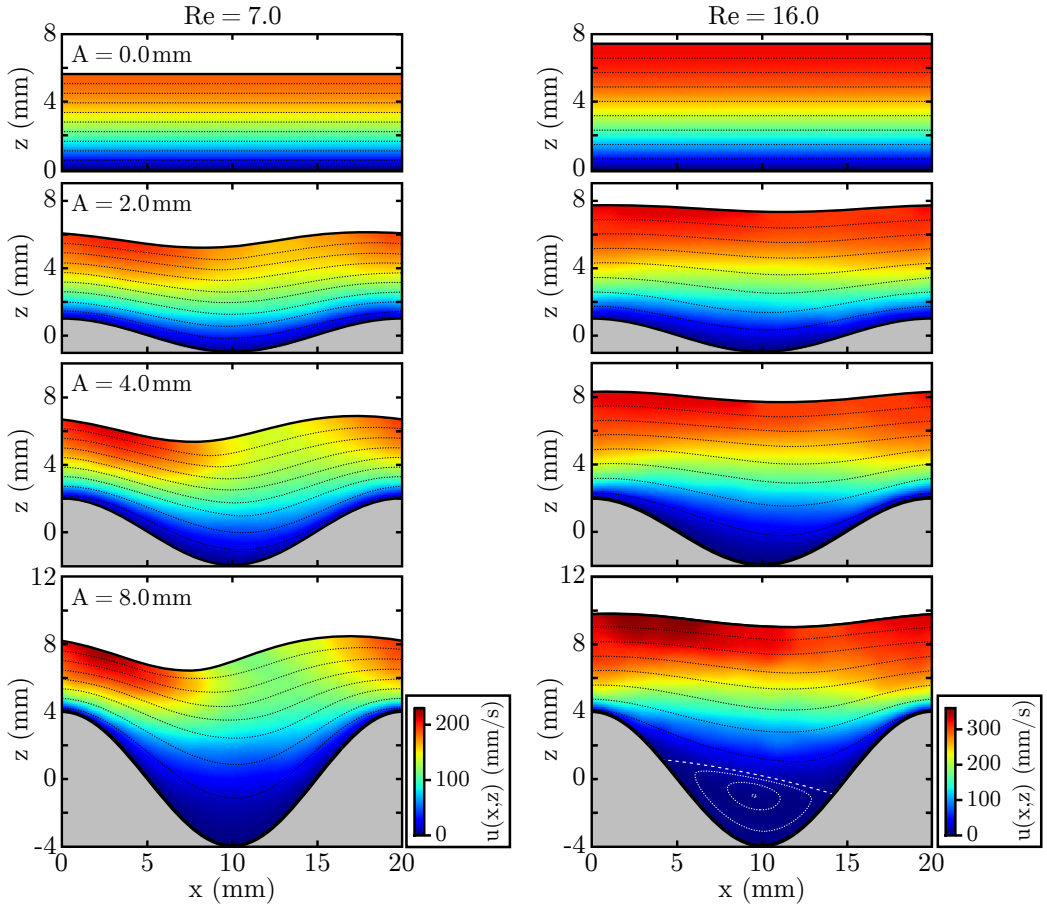

Figure 4.14.: Examples of the steady-state free surface and the velocity field of films of *Elbesil 145* flowing over four sinusoidal topographies of different amplitudes A but equal wavelength $L = 20\,\mathrm{mm}$ and inclination $\alpha = 10\,^\circ$. Left: $Re = 7.0$. Right: $Re = 16.0$. The solid black lines indicate $h_0(x)$. The local flow velocity $u(x, z)$ is color coded. The dotted lines indicate streamlines (black: main flow; white: eddy). The white dashed line corresponds to the separatrix of the eddy at $Re = 16.0$ and $A = 8\,\mathrm{mm}$. Modified and reprinted with permission from [110]. © AIP Publishing.

at all three topography wavelengths $L = \{20, 30, 40\}\,\mathrm{mm}$ and a short-wave instability nose appeared for $L \geq 30\,\mathrm{mm}$ above $Re \approx 20$. In contrast to the variations of the liquid's viscosity (see Figure 4.11), which also provoked a short-wave instability nose, no merging of the nose with the unstable isle could be observed when L was changed. It remained an open question whether the merging appears when L is increased further.

4.2.3. Identifying stabilizing and destabilizing flow phenomena

Figures 4.9 - 4.13 comprise astonishing new experimental results on the linear stability of films flowing over sinusoidally undulated inclines. The stability charts shown there exhibit a high complexity, which grew hand in hand with the amplitude of the topography (see Figure 4.9). Consequently, the first topic to be addressed is how substrate undulations of growing depth affect the stability of film flows. For this sake, the free surface $h_0(x)$ and the velocity field $\vec{u}(x, z)$ of the steady-state flow of *Elbesil 145* along the four sinusoidal topographies of increasing amplitude $A = \{0, 2, 4, 8\}\,\mathrm{mm}$ but equal wavelength $L = 20\,\mathrm{mm}$ and inclination $\alpha = 10\,^\circ$ were measured. Examples of the detected steady-state free surfaces and velocity fields are given in Figure 4.14. The more the amplitude A grew, the more the flow field differed from the strictly

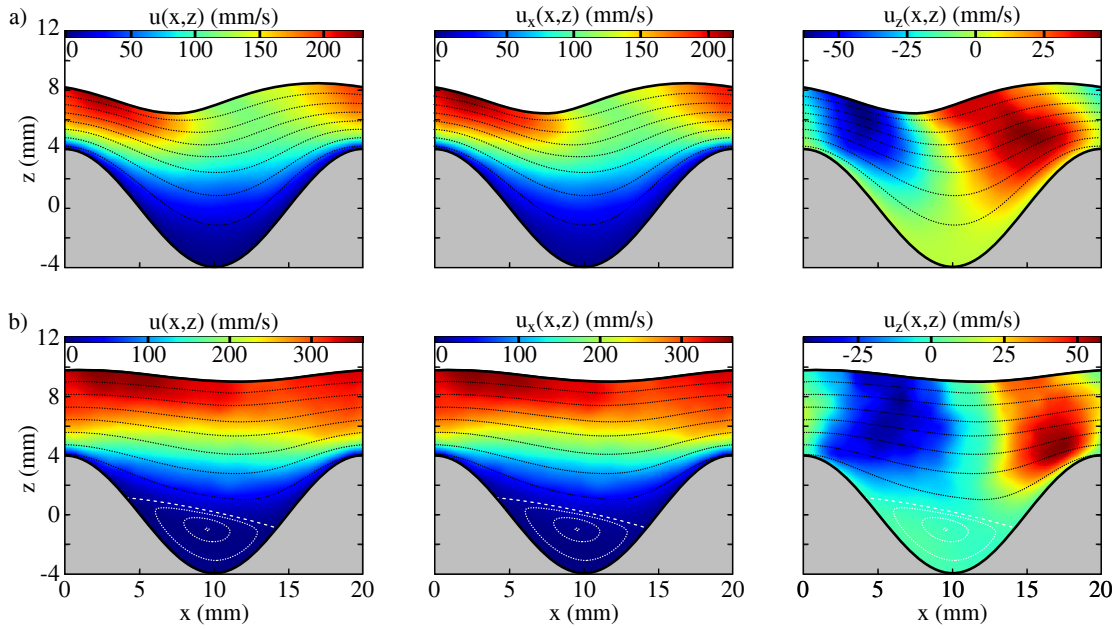

Figure 4.15.: Steady-state velocity field of films of *Elbesil 145* flowing over the sinusoidal topography with $A = 8\,\mathrm{mm}$, $L = 20\,\mathrm{mm}$ and $\alpha = 10^\circ$ at (a) $Re = 7.0$ and (b) $Re = 16.0$. The color code visualizes $u(x, z)$ (left), $u_x(x, z)$ (middle), $u_z(x, z)$ (right). The solid black lines indicate the free surface $h_0(x)$. The dotted lines indicate the streamlines (black: main flow; white: eddy). The white dashed lines in (b) correspond to the separatrix of the eddy. The figures showing $u(x, z)$ in (a) and (b) were modified and reprinted with permission from [110]. © AIP Publishing.

unidirectional Nusselt flow $\vec{u}(z) = u_x(z)\vec{e}_x$ defined in equation (3.3) and the stronger the local flow velocity $\vec{u}(x, z)$ changed within one period of the substrate's wavelength. Examples of the variation of $\vec{u}(x, z)$, including its x-component $u_x(x, z)$ and z-component $u_z(x, z)$, are given in Figure 4.15 for demonstration purpose.

In Section 4.1 the free surface, not the flow field or the topography's specific shape far below the free surface, was identified to be decisive for the linear stability of film flows (please also see Schörner *et al.* [76]). Hence, the steady-state free surface $h_0(x)$ and the steady-state free surface velocity $u_s(x)$ were evaluated as described in the Sections 3.2.2 and 3.2.3. Figure 4.16a shows that the mean film thickness h_{av} grew with increasing Reynolds number and amplitude A of the topography. For deep corrugations with $A \geq 4\,\mathrm{mm}$, h_{av} was significantly higher than the corresponding Nusselt film thickness h_n. Figure 4.16b demonstrates that the amplitude a_1 of the first free surface harmonic featured a maximum at $Re \approx 8$. This maximum of a_1 was the more pronounced, the higher the amplitude of the topography was. Above $Re \approx 11$, a_1 had significantly decreased compared to the respective maximum value. The amplitude a_2 of the second free surface harmonic versus the Reynolds number is plotted in Figure 4.16c. Increasing A led to a growth of a_2 at Reynolds numbers below $Re \approx 11$. Beyond $Re \approx 11$ the flow exhibited a harmonic free surface shape as $a_2 \to 0$ within the limits of the accuracy of the measurements. Both a_1 and a_2 quantify the size of the resonant standing waves [47, 49] which appeared in the steady-state flows over the uneven substrates. Altogether, it can be said that the deeper the undulations were, the thicker the film was and the bigger the resonant standing wave was.

The above-mentioned influence of the topography on the free surface $h_0(x)$ did not remain without consequences for the steady-state free surface velocity $u_s(x)$. Examples of $u_s(x)$ are given in Figure 4.17a. They show that the deviations of $u_s(x)$ from the corresponding Nusselt

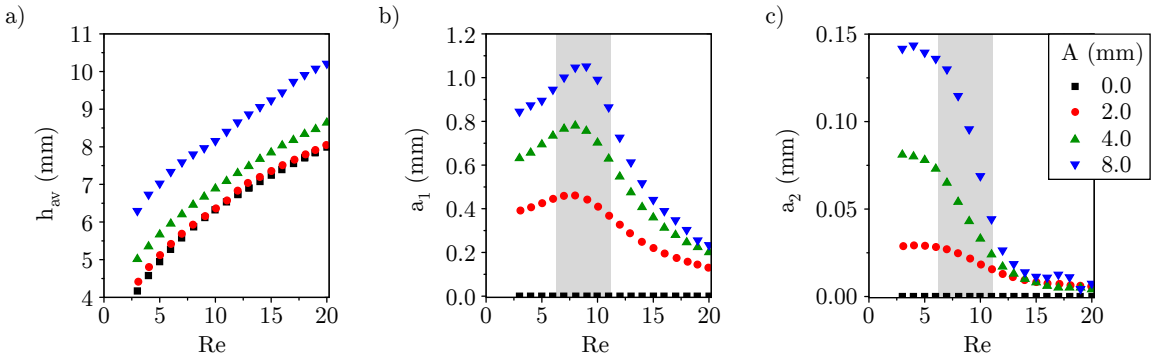

Figure 4.16.: Measurements of the steady-state free surface of films of *Elbesil 145* at $\alpha = 10\,^\circ$ flowing over the four sinusoidal topographies of different amplitudes A but equal wavelength $L = 20$ mm shown in Figure 4.14. (a) Mean film thickness h_{av}, (b) first free surface harmonic amplitude a_1 and (c) second free surface harmonic amplitude a_2, each versus the Reynolds number. The shaded area indicates the unstable isle in the flow's stability chart for $A = 8$ mm (see Figure 4.9). Modified and reprinted with permission from [110]. © AIP Publishing.

velocity $u_{s,n}$ grew hand in hand with the amplitude A of the topography. Compared to the corresponding Nusselt case, a reduced mean velocity $\bar{u}_s$ at the free surface of the flow was measured (Figure 4.17b), which can be attributed to the increased film thickness h_{av} mentioned above. Low Reynolds numbers and deep corrugations intensify the decrease of $\bar{u}_s$. Besides, the changes of $u_s(x)$ over the course of the substrate's wavelength were carefully considered. To quantify these variations, the free surface velocity gradient ∇u_s was defined as

$$\nabla u_s = \frac{u_{s,max} - u_{s,min}}{x(u_{s,min}) - x(u_{s,max})}, \tag{4.4}$$

with $u_{s,max} = \max[u_s(x)]$ and $u_{s,min} = \min[u_s(x)]$. Figure 4.17c shows how the Reynolds number and the undulation's amplitude affect ∇u_s. The deeper the corrugations were, the stronger $u_s(x)$ varied within one period of the topography and the higher ∇u_s was. The biggest resonant standing waves appeared below $Re \approx 11$. Hence, ∇u_s reached its maximum there.

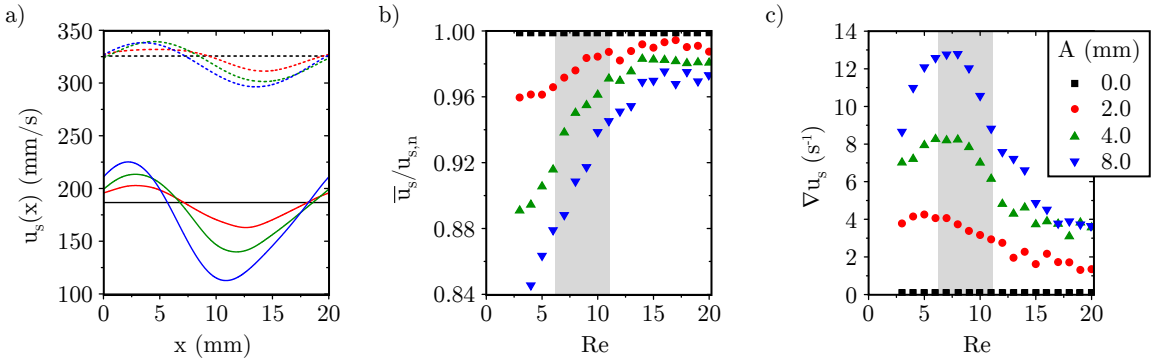

Figure 4.17.: Measurements of the steady-state free surface velocity of films of *Elbesil 145* at $\alpha = 10\,^\circ$ flowing over the four sinusoidal topographies of different amplitudes A but equal wavelength $L = 20$ mm shown in Figure 4.14. (a) Local free surface velocity $u_s(x)$, exemplarily shown for $Re = 7.0$ (solid lines) and $Re = 16.0$ (dashed lines). (b) Ratio $\bar{u}_s/u_{s,n}$ of the mean free surface velocity $\bar{u}_s$ and the free surface velocity $u_{s,n}$ of the corresponding Nusselt flow. (c) Free surface velocity gradient ∇u_s. The shaded area indicates the unstable isle in the flow's stability chart for $A = 8$ mm (see Figure 4.9). Modified and reprinted with permission from [110]. © AIP Publishing.

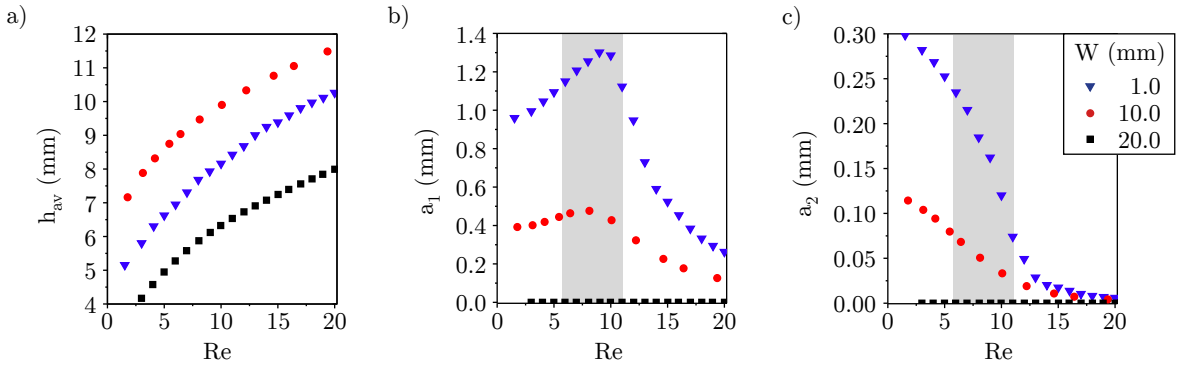

Figure 4.18.: Measurements of the steady-state free surface of films of *Elbesil 145* at $\alpha = 10\,^\circ$ flowing over the three rectangular topographies of different tip widths W but equal amplitude $A = 8\,\text{mm}$ and wavelength $L = 20\,\text{mm}$. (a) Mean film thickness h_{av}, (b) first free surface harmonic amplitude a_1 and (c) second free surface harmonic amplitude a_2, each versus the Reynolds number. The shaded area indicates the unstable isle in the flow's stability chart for $W = 1\,\text{mm}$ (see Figure 4.12).

The complexity of the linear stability charts shown in the Figures 4.9 - 4.13 can only be explained by the presence of stabilizing as well as destabilizing effects which do not equally appear in the corresponding Nusselt flows. Those are the above-mentioned increased mean film thickness (Figure 4.16a), the curved steady-state free surface (Figures 4.16b, 4.16c), and as a consequence of both, the modified free surface velocity of the flow (Figure 4.17).

The mean film thickness h_{av} was shown to increase hand in hand with the amplitude A of the topography. This led to a decreased flow velocity $\bar{u}_s$, which is reported to have a stabilizing effect [99]. If the flow over wavy inclines is stabilized due to $h_{av} > h_n$, why is there nevertheless an unstable isle at low Reynolds numbers which provokes a global destabilization of the flow, e.g., in Figure 4.9? The present study unveiled that resonant standing waves give rise to the unstable isle. For films of *Elbesil 145* flowing along a sinusoidally undulated incline with $\alpha = 10\,^\circ$, $A \geq 4\,\text{mm}$ and $L = 20\,\text{mm}$, the unstable isle appeared at exactly the same Reynolds numbers where the free surface curvature, quantified by a_1 and a_2, reached its maximum. The more the topography's amplitude A grew, the stronger the resonance was and the more pronounced the formation of the unstable isle was (please compare the Figures 4.9 and 4.16). This is not a coincidence, but can be attributed to strong velocity gradients ∇u_s at the free surface of the flow (see Figure 4.17c) which have a destabilizing effect, similar to weak hydraulic jumps [55]. For the less undulated topography with $A = 2\,\text{mm}$, the resonance was weaker and provoked only a precursor of the unstable isle around $Re \approx 8$ and $f \approx 1\,\text{Hz}$ (see Figure 4.9).

Besides increasing the topography's amplitude beginning with $A = 0$ as described above, the topography's tip width was decreased in the experimental asymptotics from $W = L = 20\,\text{mm}$ to $W = 1\,\text{mm}$ while all other system parameters were kept constant (see Figure 4.8). The measured stability charts exhibited a high complexity (Figure 4.12), which grew when the tip width was reduced, i.e. the flow had more space to attune freely (please see the gedankenexperiment in Section 4.1.4). The overall evolution of the stability charts was found to be similar when either A was increased or W was decreased (please compare the Figures 4.9 and 4.12). As discussed in Section 4.1, the steady-state free surface $h_0(x)$ is decisive for the shape of the stability chart. Hence, in order the unveil whether the same stabilizing (h_{av} increased) and destabilizing (free surface resonance) effects are present when either A or W is varied, the steady-state free surface $h_0(x)$ was measured for the three tip widths $W = \{1, 10, 20\}\,\text{mm}$. The results are plotted in Figure 4.18. Indeed, decreasing W and increasing A had basically the same effect on the

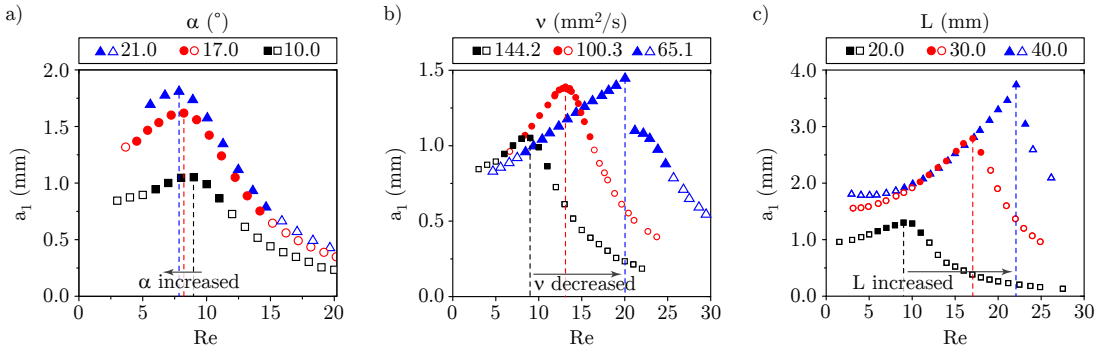

Figure 4.19.: First free surface harmonic amplitude a_1 of the steady-state film flows over corrugations with $A = 8\,\text{mm}$ versus the Reynolds number. Filled symbols indicate the core of the unstable isle in the stability chart of the respective flow. (a) Dependence on the inclination α of the topography at fixed viscosity $\nu = 144.2\,\text{mm}^2/\text{s}$ and wavelength $L = 20\,\text{mm}$ of the sinusoidal topography. (b) Dependence on the viscosity ν at fixed inclination $\alpha = 10°$ and wavelength $L = 20\,\text{mm}$ of the sinusoidal topography. (c) Dependence on the wavelength L of the rectangular topography at fixed viscosity $\nu = 144.2\,\text{mm}^2/\text{s}$, inclination $\alpha = 10°$ and tip width $W = 1\,\text{mm}$. The dashed lines highlight the maxima of a_1. (a), (b) Modified and reprinted with permission from [110]. © AIP Publishing.

steady-state free surface as a comparison of the Figures 4.16 and 4.18 shows. In both cases, the mean film thickness h_{av} was increased at all Reynolds numbers compared to the corresponding Nusselt flow. Besides, a maximum of the first free surface harmonic amplitude a_1 appeared at $Re \approx 8$, where the core of the unstable isle of the corresponding stability charts (Figures 4.9 and 4.12) is located. Moreover, the second free surface harmonic amplitude $a_2 \to 0$ above $Re \approx 11$, i.e. at Reynolds numbers beyond the unstable isle. Hence, the stabilizing (increased mean film thickness) and destabilizing (free surface resonance) effects provoked by variations of the corrugation parameters A and W appear to be the same. The sharper the tips were, the stronger the resonance was and the more pronounced the formation of the unstable isle was (see Figure 4.12). At $W = 10\,\text{mm}$ the resonance was weak (see Figure 4.18b) and only a precursor of the unstable isle appeared in the stability chart around $Re \approx 8$ (see Figure 4.12).

As long as the inclination, the viscosity and the topography wavelength were not changed, the maximum of resonance of the steady-state free surface and, hence, the unstable isle stayed at Reynolds numbers between $Re \approx 6$ and $Re \approx 11$ (Figures 4.9, 4.12, 4.16, 4.18). Variations of the inclination (Figure 4.10), the viscosity (Figure 4.11) or the topography wavelength (Figure 4.13) led to a shift of the maximum of the first free surface harmonic amplitude a_1 and thus of the unstable isle as indicated in Figure 4.19.

4.2.4. Conclusions

The stability charts of gravity-driven film flows over corrugated inclines were found to exhibit a high complexity, which grows hand in hand with increasing amplitude or decreasing tip width of the topography (Figures 4.9 and 4.12) and depends in a nontrivial way on the inclination angle, the liquid's viscosity and the topography's wavelength (Figures 4.10, 4.11 and 4.13). Measurements of the steady-state free surfaces and velocity fields attributed the complex shape of the measured stability charts to the simultaneous presence of stabilizing as well as destabilizing effects provoked by the topography. The stabilization of the flow due to an increased mean film thickness and the destabilization of the flow due to resonance of the steady-state free surface were shown to be competing effects. For films of *Elbesil 145* flowing over moderately inclined topographies ($\alpha = 10°$, $L = 20\,\text{mm}$) which exhibited either steep sinusoidal undula-

tions ($A \geq 4\,\mathrm{mm}$) or sharp rectangular corrugations ($W = 1\,\mathrm{mm}$, $A = 8\,\mathrm{mm}$) the resonance phenomenon dominated. This reduced the critical Reynolds number compared to the corresponding Nusselt flow and provoked an unstable isle in the linear stability chart. Decreasing the inclination or the viscosity, or increasing the topography wavelength shifted the resonance maximum and thus the unstable isle to higher Reynolds numbers. That way, the stabilizing effect of the increased film thickness dominated at low Reynolds numbers and the flows were more stable against long-wave perturbations than the corresponding Nusselt flows. Hence, the interplay between the topography's amplitude, wavelength, inclination and tip width as well as the liquid's viscosity determines whether the stabilizing or the destabilizing effect prevails.

The above-mentioned interaction between competing effects cannot be approximated properly by the well-known Nusselt solution: reducing a film flow over deep corrugations to a Nusselt flow would disregard the significantly differing steady-state flow phenomena which govern the flow's stability – far beyond the limits of Nusselt's theory.

4.3. Patterns and universal pathway of the linear stability

The thematic priority of precedent work on the linear stability of gravity-driven viscous films flowing down corrugated inclines was to unveil and scrutinize specific stability phenomena, provoked by the interplay of the fluid and the topography (please see the Sections 4.1, 4.2 and the References [76, 107, 108, 110, 112, 113, 122]). For a plenty of very different individual systems the specific *shape*, inclination α, amplitude A, wavelength L and tip width W of the topography as well as the viscosity ν of the liquid were varied and the linear stability of the flow was scrutinized in both theory and experiment. Similarities were observed, e.g., an increase of α or a decrease of ν had a similar effect on the stability chart (please see the Figures 4.10 and 4.11 in Section 4.2). Moreover, a switching between different types of stability isles was observed when α, ν, L, A or W were varied [110, 113]. However, no universal principle was found behind the changes, being valid to describe the evolution of the flow's stability chart for variations of all the parameters α, ν, L, A, W and *shape*. This lack of information constituted a problem for, e.g., technical applications of film flows. There was no possibility to predict how a system reacts on a change of one of the above-mentioned parameters unless the stability chart of the specific system was measured or calculated.

The scope of the study presented in the present Section 4.3 is to provide a universal guide on how to tune the linear stability of a gravity-driven Newtonian film flowing over an inclined topography in a way which is desired or required. In other words, the fundamental question "Is there a universal principle, being valid to describe the parametric evolution of the flow's stability chart for variations of different system parameters?" was considered. For this sake, in a first step, all corresponding stability charts available in the literature [76, 107, 108, 110, 112, 113, 122] were screened. In a second step, experiments were performed to fill the gaps which remained after the parameter spaces of the independent investigations were combined. That way, a set of six characteristic patterns of stability charts was identified to be sufficient to describe and unify all previous results on the linear stability of Newtonian films flowing over undulated inclines. Finally, a universal pathway – the stability cycle – was unveiled along which the linear stability charts of all considered Newtonian films flowing down periodically corrugated inclines evolved when the fluid or the topography was changed.

The present Section 4.3 relies on the publication *"The stability cycle – A universal pathway for the stability of films over topography"* from Schörner and Aksel [114].

4.3.1. Parameter space and methodology

The study presented in Section 4.3 condenses all linear stability charts of Newtonian films flowing over inclined topographies available in the literature [76, 107, 108, 110, 112, 113, 122]. New experiments [114] were carried out only to fill the gaps in the combined parameter space of all precedent work on this topic. That way, parallel strains of step-by-step variations of each considered parameter of the system were obtained while all other parameters were kept constant. The system parameters are the specific *shape*, inclination α, amplitude A, wavelength L and tip width W of the topography as well as the kinematic viscosity ν of the liquid (see Figure 3.2a). The three silicone oils *Elbesil 65*, *100* and *145*, used by previous authors [76, 107, 108, 110, 112, 113, 122] and described in Section 3.1.1, were chosen as liquids. Their kinematic viscosities ν ranged from $65\,\mathrm{mm^2/s}$ to $144\,\mathrm{mm^2/s}$ (see Table 3.1). The different specific shapes of the topography, i.e. *Sin*, *SinMod*, *Saw*, *SawRev*, *Rec* and *Flat*, are illustrated in Figure 3.2b. The inclination α was varied between $4.1\,^\circ$ and $36.7\,^\circ$. For the corrugated substrates the amplitude A was varied from $0.4\,\mathrm{mm}$ to $14.4\,\mathrm{mm}$, the wavelength L from $10\,\mathrm{mm}$ to $200\,\mathrm{mm}$, and

the tip width W from 1 mm to 100 mm. The flat incline was considered as either the borderline case $A = 0$, $L = 0$, $L = \infty$ or $W = L$. A detailed list of all parallel strains of the variations of α, ν, L, A, W and *shape* is given in the respective tables in Appendix A. Please see Table A.1 for the variations of α, Table A.2 for ν, Table A.3 for L, Table A.4 for A, Table A.5 for W and Table A.6 for *shape*.

The experimental methodology to measure the flow's linear stability was introduced in Section 3.2.4. The numerical method of the steady-state solution's computation and the stability analysis used by previous authors was described in detail in the literature [44,98,99,108,112,113]. In a nutshell, their theoretical analysis was based on the Navier-Stokes equations in their full statement without asymptotic approximations. The computed neutral curves were given either as $Q(Re)$ or $f(Re)$, with Q being the Floquet parameter and f being the frequency of the disturbance. The Floquet parameter Q describes the exponent in the ansatz for the solution of a periodical system. Please see, e.g. Trifonov [99, 108], for details on Q and Schörner *et al.* [113] for the relation between Q and f. In the present work, the computed neutral curves $Q(Re)$ of [108, 112] are shown only if the corresponding curve $f(Re)$ has not been published. Even though the respective axes of Q and f slightly differ, the overall pattern of the stability chart remains the same in both representations. Please see [108, 113] for details and examples.

4.3.2. Characteristic patterns of stability charts

The present approach condenses all experimental and numerical linear stability charts of Newtonian film flows over undulated inclines available in the literature [76, 107, 108, 110, 112–114, 122]. The respective data are summarized in the Appendices A.1 - A.6. This holistic approach made it possible to identify the six characteristic patterns of stability charts sketched and described by key-words in Figure 4.20. All available stability charts can be assigned to one of these six patterns, as described below.

Pattern I represents the classical long-wave type primary instability of the flow over a flat incline [11,80]. Pattern II is a long-wave type primary instability with a dip. Pattern III exhibits two disjoined long-wave instability branches. The unstable isle at low Reynolds numbers and the long-wave instability at higher Reynolds numbers are separated by a stable flow regime where all disturbances are damped. Pattern IV has two disjoined instability branches with a short-wave type instability nose as illustrated in Figure 4.20. Pattern V is a short-wave type primary instability with an unstable bridge above the stable isle. Pattern VI characterizes the short-wave type primary instability.

This set of the six characteristic stability chart patterns, defined in Figure 4.20, was found to be sufficient and powerful enough to uniformly describe all available linear stability charts of Newtonian films flowing over corrugated inclines. No counterexample was found which did not fit to one of these six patterns.

4.3.3. Transitions between different patterns of stability charts

In Figure 4.21, all available linear stability charts were assigned to the six characteristic stability chart patterns I - VI defined in Figure 4.20. The data were grouped in a way to obtain parallel strains of step-by-step variations of single fluid or topography parameters. Hereby, one parameter was varied while the others were kept fixed. The arrows represent the transitions between different patterns of stability charts which appeared when the inclination α, the viscosity ν, the wavelength L, the amplitude A or the tip width W were increased. Hence, each one of the vertical strains in Figure 4.21 illustrates schematically how the stability chart of

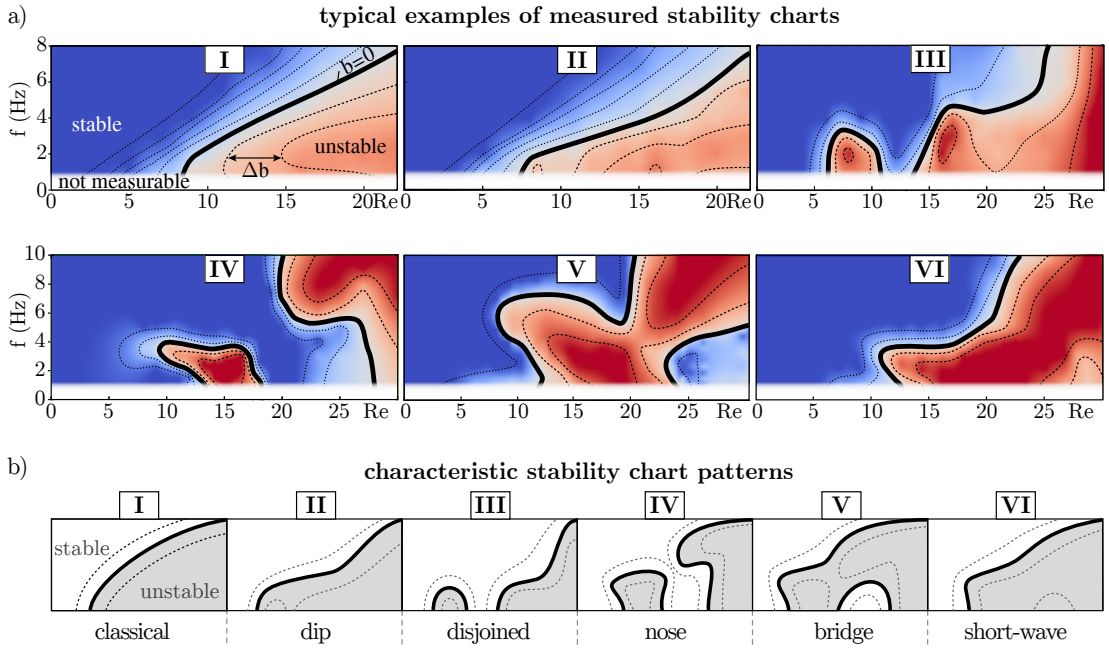

Figure 4.20.: (a) Typical examples of measured stability charts. The bold black line is the neutral curve. The growth rate b of the linear free surface disturbances is color-coded (red: unstable, blue: stable) and the contour lines are shown as dashed lines in steps of Δb. The exemplary measurements correspond to $\alpha = 10\,^{\circ}$ and I: *Flat*, $\nu = 144\,\mathrm{mm^2/s}$, $\Delta b = 0.5\,\mathrm{m^{-1}}$; II: *Sin*, $\nu = 144\,\mathrm{mm^2/s}$, $A = 2\,\mathrm{mm}$, $L = 20\,\mathrm{mm}$, $\Delta b = 0.5\,\mathrm{m^{-1}}$; III: *Sin*, $\nu = 144\,\mathrm{mm^2/s}$, $A = 12\,\mathrm{mm}$, $L = 20\,\mathrm{mm}$, $\Delta b = 1.0\,\mathrm{m^{-1}}$; IV: *Rec*, $\nu = 144\,\mathrm{mm^2/s}$, $A = 8\,\mathrm{mm}$, $L = 30\,\mathrm{mm}$, $W = 1\,\mathrm{mm}$, $\Delta b = 1.0\,\mathrm{m^{-1}}$; V: *Sin*, $\nu = 65\,\mathrm{mm^2/s}$, $A = 8\,\mathrm{mm}$, $L = 20\,\mathrm{mm}$, $\Delta b = 2.0\,\mathrm{m^{-1}}$ and VI: *Rec*, $\nu = 100\,\mathrm{mm^2/s}$, $A = 8\,\mathrm{mm}$, $L = 40\,\mathrm{mm}$, $W = 20\,\mathrm{mm}$, $\Delta b = 1.0\,\mathrm{m^{-1}}$. Data of the example of I, II and V taken from Schörner *et al.* [110]. (b) Characteristic stability chart patterns I - VI. Modified and reprinted with permission from [114]. © AIP Publishing.

the respective system, labeled by the Arabical numeral i, evolves with an increase of one of the parameters α, ν, L, A, W while all others were kept constant. The parameter space and the raw data are given in the Appendices A.1 - A.6. For example, data on the increase of the inclination α were available for five different systems, labeled by the Arabical numerals 1 - 5 in Figure 4.21, listed in Appendix A.1.1 and plotted as raw data in Appendix A.1.2. If no arrow is shown, e.g., for system number 5 in the variations of α, changes of the respective parameter did not lead to a different stability pattern. Furthermore, modifications of the specific *shape* of the topography were found to have only a minor effect on the stability chart if the free surface remained unchanged [76]. Additional findings for varying *shape* of the topography were not explicitly included in Figure 4.21, yet summarized in Appendix A.6 for convenience and completeness.

Variations of α, ν, L, A or W provoked transitions between the different stability chart patterns either along the pathway I $\rightarrow$ II $\rightarrow$ III $\rightarrow$ IV $\rightarrow$ V $\rightarrow$ VI $\rightarrow$ II $\rightarrow$ I or reverse. The direction of the transitions between two specific stability patterns, represented by the arrows in Figure 4.21, was the same for all systems $\{shape, \alpha, \nu, L, A, W\}$ as long as only one specific parameter was modified.

Changes of α and ν never provoked a transition between pattern I and II (see Figure 4.21). This transition is not possible as pattern I was defined as the classical long-wave type instability of films flowing over flat inclines, valid for all viscosities ν and inclinations $0 < \alpha < \pi/2$. Moreover, changes of A and W never resulted in a transition between pattern III and IV (see Figure 4.21). Concerning the tip width W, pattern III or IV corresponds to the minimal tip

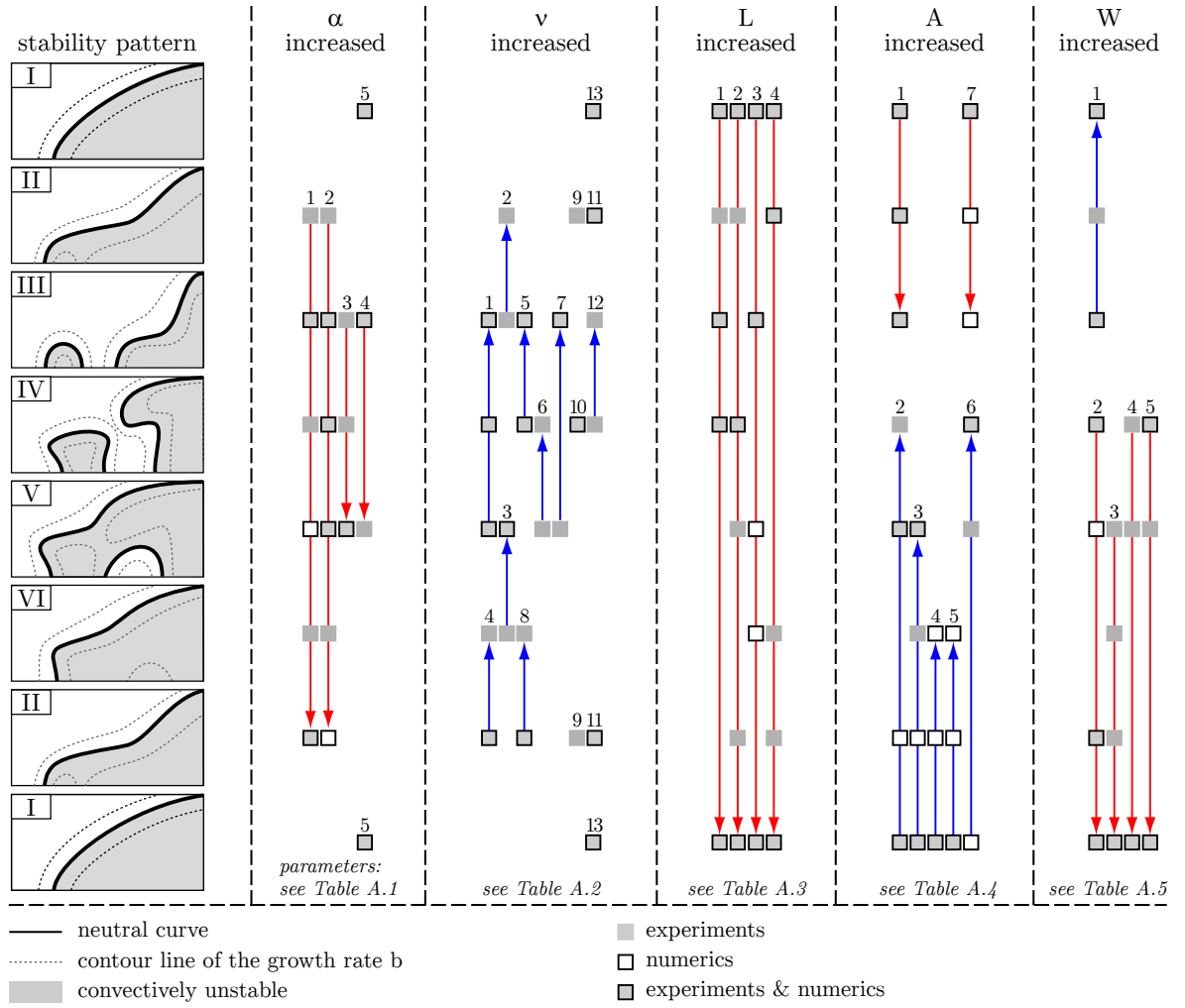

Figure 4.21.: Schematic evolution of the linear stability chart of film flows when α, ν, L, A or W are increased in the direction of the arrows (red: top → down; blue: bottom → up). The illustration comprises all precedent work [76, 107, 108, 110, 112, 113, 122] and the new measurements from [114]. The parameter configurations {*shape*, α, ν, L, A, W} are specified in the respective Tables A.1 - A.5 in Appendix A. The Arabical numeral i denotes the system and corresponds to the same number in the respective table. All corresponding stability charts are given in the Appendices A.1 - A.5. Modified and reprinted with permission from [114]. © AIP Publishing.

width. A further reduction beyond the geometric constraint $W \to 0$ is impossible. The tip always remains as an obstacle with $W \neq 0$. Concerning the amplitude A, there is no geometric constraint prohibiting $A \to \infty$. It remains an open question why variations of A never induced transitions between pattern III and IV.

4.3.4. The stability cycle – A universal pathway for the linear stability

The results in Figure 4.21 and the pathway I → II → III → IV → V → VI → II → I can be formed to a circle which will be called the 'stability cycle'. For convenience, it is separated in three cycles as illustrated in Figure 4.22.

A certain degree of symmetry is visible in Figure 4.22. In an antagonistic way, α and ν are decisive for the influence of the inertia on the film flow. That way, both parameters provoke the same transitions along the pathway with either being increased or decreased. The same is valid

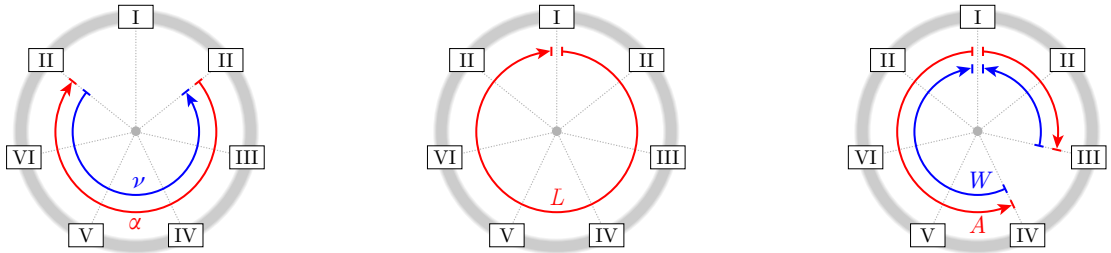

Figure 4.22.: The stability cycle. The direction of the arrows is color-coded as in Figure 4.21 and corresponds to the pathway of the transitions between different patterns of stability charts, when one of the parameters α, ν, L, A or W is increased. Modified and reprinted with permission from [114]. © AIP Publishing.

for A and W which are decisive for the curvature of the steady-state free surface [40, 110] and, hence, the segmentation of the stability chart [110] (please see Section 4.2.3). No counterpart appeared for the wavelength L. On grounds of L being a geometric length the counterpart should be an intrinsic length, namely the capillary length. This hypothesis could not be proven in the present approach since the surface tension was not changed in the experiments.

The stability cycle shown in Figure 4.22 can be considered as a universal pathway for the stability, describing the parametric evolution of the linear stability charts of Newtonian films. All experimental and numerical findings can be assigned to the six characteristic stability chart patterns and all reported transitions between these patterns fit to the pathway. No contradicting observations are reported, falsifying this interpretation. It does not matter which specific shape, amplitude or wavelength the corrugations have, how viscous the Newtonian fluid or how steep the inclination is. One of the six patterns described above characterizes the stability chart of each system $\{shape, \alpha, \nu, L, A, W\}$. Taking the respective stability pattern as a starting point, the stability cycle predicts how the pattern changes when one of the parameters of the system is modified. In other words, it tells the reader how to adapt the system to obtain, for example, pattern III with a stable flow regime at Reynolds numbers far beyond $Re_c = (5/4)\cot\alpha$.

4.3.5. Conclusions

Is there a universal principle, being valid to describe the parametric evolution of the flow's linear stability chart for variations of different system parameters? In search of an answer to this fundamental question, all experimental and numerical stability charts available in the literature were screened. In a second step, experiments were performed to fill the gaps which remained after the parameter spaces of the independent, precedent investigations were combined (Appendix A). That way, the set of six characteristic stability chart patterns shown in Figure 4.20 was identified to be sufficient to describe and unify all previous results on the linear stability of Newtonian films flowing over undulated inclines. Variations of the fluid's viscosity or the topography's specific shape, amplitude, wavelength, tip width or inclination led to transitions between these six patterns. These pattern transitions shift unstable and stable flow regimes and can provoke crucial flow stabilization at high Reynolds numbers, important in physical and technical applications. By considering the whole set of transitions (Figure 4.21) a universal pathway – the stability cycle – was unveiled, along which the linear stability charts of all considered Newtonian films flowing down periodically corrugated inclines evolved when the above-mentioned system parameters were changed (Figure 4.22). The stability cycle can be interpreted as a universal guide on how to tune the linear stability of two-dimensional gravity-driven Newtonian films flowing over inclined topographies in a way which is desired or required.

4.4. Beyond the linear stability of two-dimensional Newtonian films

The characteristic stability chart patterns and the stability cycle presented in Section 4.3 were found to be valid for all two-dimensional Newtonian film flows, which are perturbed by linear free surface waves and flowing down periodically undulated inclines [114]. No contradicting observations are reported. However, it remained an open question whether similar phenomena can also be found beyond the linear stability of two-dimensional Newtonian films. Are the characteristic stability chart patterns and the stability cycle still valid for, e.g., non-Newtonian fluids (Section 4.4.1), nonlinear waves (Section 4.4.2) and three-dimensional channel flow with sidewalls (Section 4.4.3)?

4.4.1. Non-Newtonian fluids

For the practical issue of flow stabilization in engineering-technological applications the intriguing question arises whether the characteristic stability chart patterns and the stability cycle, both described in Section 4.3 for films of Newtonian fluids, are still valid for films of non-Newtonian fluids. To the author's knowledge, the only work to mention in this context is the numerical study by Heining and Aksel [100], who calculated linear stability charts of power-law liquids flowing down sinusoidal topographies of different steepnesses $\xi = A/h_n$. Figure 4.23a shows the stability charts for $\xi = 0.4$ and power-law index $n = 0.8$ (shear-thinning), $n = 1.0$ (Newtonian) and $n = 1.2$ (shear-thickening). Please see the caption of Figure 1.24 for the definition of the stress tensor including the power-law index n.

The linear stability charts of the non-Newtonian fluids shown in Figure 4.23a can be attributed to the same stability patterns which also describe the stability of Newtonian fluids (see Figure 4.20), but the pathway of the transitions exhibits a turning point at $n = 1.0$ (see Figure 4.23b). Clearly, more experiments and computations on the linear stability of non-Newtonian films flowing down periodically undulated topographies are required to shed light on this complex problem. It will be interesting to see if the linear stability charts of non-Newtonian films match to the characteristic stability chart patterns of Newtonian films in general.

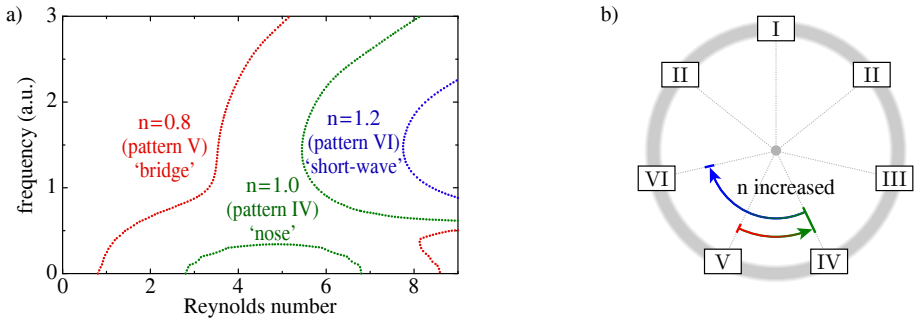

Figure 4.23.: (a) Linear stability charts of two-dimensional films of power-law liquids flowing down a sinusoidally undulated incline of the steepness $\xi = 0.4$. The stability charts of the shear-thinning (power-law index $n = 0.8$) and the shear-thickening ($n = 1.2$) fluid can be attributed to the same stability patterns defined on grounds of the Newtonian films ($n = 1.0$; see Section 4.3.2). Data taken from Heining and Aksel [100]. (b) In contrast to the parameters α, ν, L, A, W studied in Section 4.3, the pathway of the transitions between the stability chart patterns exhibits a turning point at $n = 1.0$, when n is increased. This turning point can be considered as a new feature, which did not appear at any parameter variation in the pathway of the stability of Newtonian film flows (please compare to Figure 4.22).

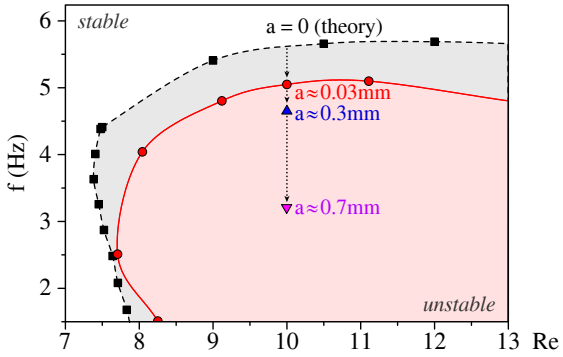

Figure 4.24.: Computed ($a = 0$; black dashed line) and measured ($a \approx 0.03$ mm; red solid line) linear stability chart for *Elbesil 100*, *Sin*, $\alpha = 10°$, $A = 8$ mm and $L = 20$ mm. Data taken from [113]. The experimental neutral points at $Re = 10$ were determined from Reck and Aksel [125] and correspond to the different perturbation amplitudes $a \approx 0.03$ mm, 0.3 mm and 0.7 mm. The vertical arrows indicate the shift of the neutral point at $Re = 10$ with the perturbation amplitude a being increased, i.e. with a transition from linear to nonlinear waves [125].

4.4.2. Nonlinear disturbances

How nonlinear disturbances affect the stability of two-dimensional Newtonian films flowing over inclined topographies is still an open question of imperative importance for real-world applications of film flows, where the traveling waves are usually not linear. What happens when the disturbances are not strictly linear but weakly or even strongly nonlinear with their free surface amplitude a not being small compared to the film thickness? Are the characteristic stability chart patterns and the stability cycle (see Section 4.3) still valid for nonlinear free surface perturbations?

The scope of this section is to briefly discuss the qualitative effects of nonlinear disturbances on the neutral curves of films over topographies and to highlight specific flow phenomena for demonstration purpose, without claiming universality and completeness. For this sake, we begin with a discussion on the term 'linear free surface disturbance' and its different meaning in theoretical and experimental approaches. Subsequently, the free surface amplitude and the nonlinear character of the traveling free surface wave is gradually increased. Both weakly and strongly nonlinear disturbances are considered and their impact on the flow's stability chart is briefly outlined.

From linear to weakly nonlinear disturbances

All real-world systems and all physical experiments deal with perturbations of non-vanishing amplitude $a \neq 0$. This constitutes a fundamental difference to the theory of linear disturbances with $a = 0$ in the computations and gives rise to a slight disparity of the numerical and the experimental neutral curves [113]. For traveling free surface waves with $a \neq 0$ and $a \to 0$ in the experimental limit, which are denoted as 'linear disturbances' in the experiments, the unstable regimes in the flow's stability chart slightly shrink compared to the corresponding computational results [113]. Please see the example given in Figure 4.24 for $a = 0$ (theory; black color) and $a \approx 0.03$ mm (linear stability measurements; red color), where the neutral points shift to lower perturbation frequencies f with a being increased. According to the experimental findings by Reck and Aksel [125], this shift is the more pronounced, the larger a is (please see Figure 4.24 at $Re = 10$). Beyond, Reck and Aksel [125] evaluated the wave number spectra at $Re = 10$ and $a \approx 0.03$ mm, 0.3 mm and 0.7 mm. At $a \approx 0.03$ mm, which is

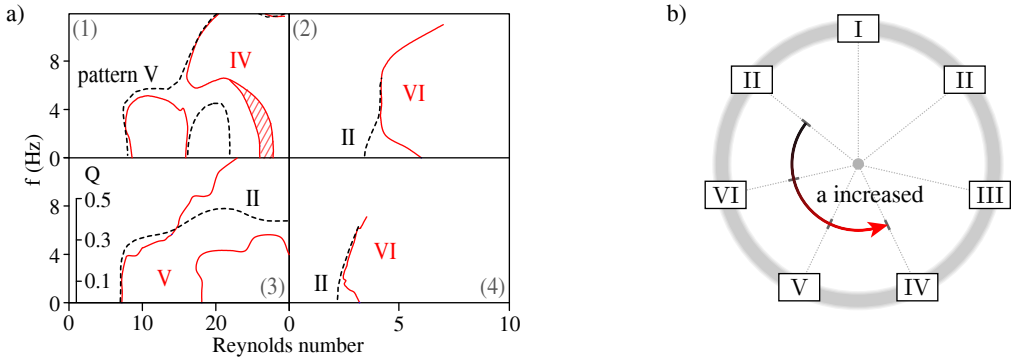

Figure 4.25.: (a) Stability charts of the four systems which exhibit a different stability pattern in theory ($a = 0$; black dashed lines) and experiment ($a \approx 0.03$ mm; red solid lines). Hatched markings denote measurement uncertainties. The computed neutral curve in (3) is shown as $Q(Re)$ as no relation between the Floquet parameter Q and the perturbation frequency f was published (see Section 4.3.1). The examples correspond to *Sin*, $L = 20$ mm and (1) *Elbesil 100*, $\alpha = 10.0°$, $A = 8$ mm; (2) *Elbesil 100*, $\alpha = 24.9°$, $A = 8$ mm; (3) *Elbesil 100*, $\alpha = 10.0°$, $A = 4$ mm; (4) *Elbesil 145*, $\alpha = 36.7°$, $A = 8$ mm. (b) The pattern transitions II $\rightarrow$ VI $\rightarrow$ V $\rightarrow$ IV, which appear in (a) when the amplitude a of the free surface perturbation is slightly increased, fit to the stability cycle defined in Section 4.3.4.

the same perturbation amplitude used for the linear stability measurements shown in Figure 4.24, one dominant peak appeared at the fundamental wave number of the excitation and they denoted these waves as 'linear waves', in line with the nomenclature used in this thesis. Despite this notation, their results showed that the traveling free surface waves in real-world experiments are intrinsically not strictly linear but weakly nonlinear, as external noise sources and non-vanishing amplitudes of higher harmonics are always present (see Section 3.2.4 and Figure 3.11c). In other words, the difference between the computed and the measured neutral curves can be interpreted as a first indication of how a stability chart changes when not strictly linear but weakly nonlinear disturbances are imposed to the flow.

As described above, the perturbation amplitudes $a \approx 0.03$ mm in the linear stability measurements were very small compared to the film thickness. For the vast majority of the systems considered in the present study, the measured and computed neutral curves were in good agreement (see Appendix A). Only four out of a total of over 70 systems exhibited a clearly different stability pattern in theory and experiment (see Figure 4.25a). For all other systems the difference in a between theory and experiment was too small to provoke a pattern transition. To the author's knowledge, no other comparable stability charts $f(Re)$ of gravity-driven films over inclined topographies, perturbed by nonlinear waves, are published. Hence, the results shown in Figure 4.25a can be interpreted as the first indications of how the stability patterns of viscous film flows over inclined topographies can change when weakly nonlinear disturbances are imposed to the flow. Indeed, when the perturbation amplitude a is increased and weakly nonlinear effects appear, all observed transitions between different stability chart patterns still follow the 'stability cycle' (see Figure 4.25b). Clearly, this statement is based on a small sample and cannot claim universality. Further work on the evolution of nonlinear waves over inclined topographies is needed to shed light on this complex problem. For technical applications of film flows, it will be interesting to see if the stability charts for weakly nonlinear disturbances, faced in the real world of engineering, match to the characteristic stability patterns and the 'stability cycle' in general.

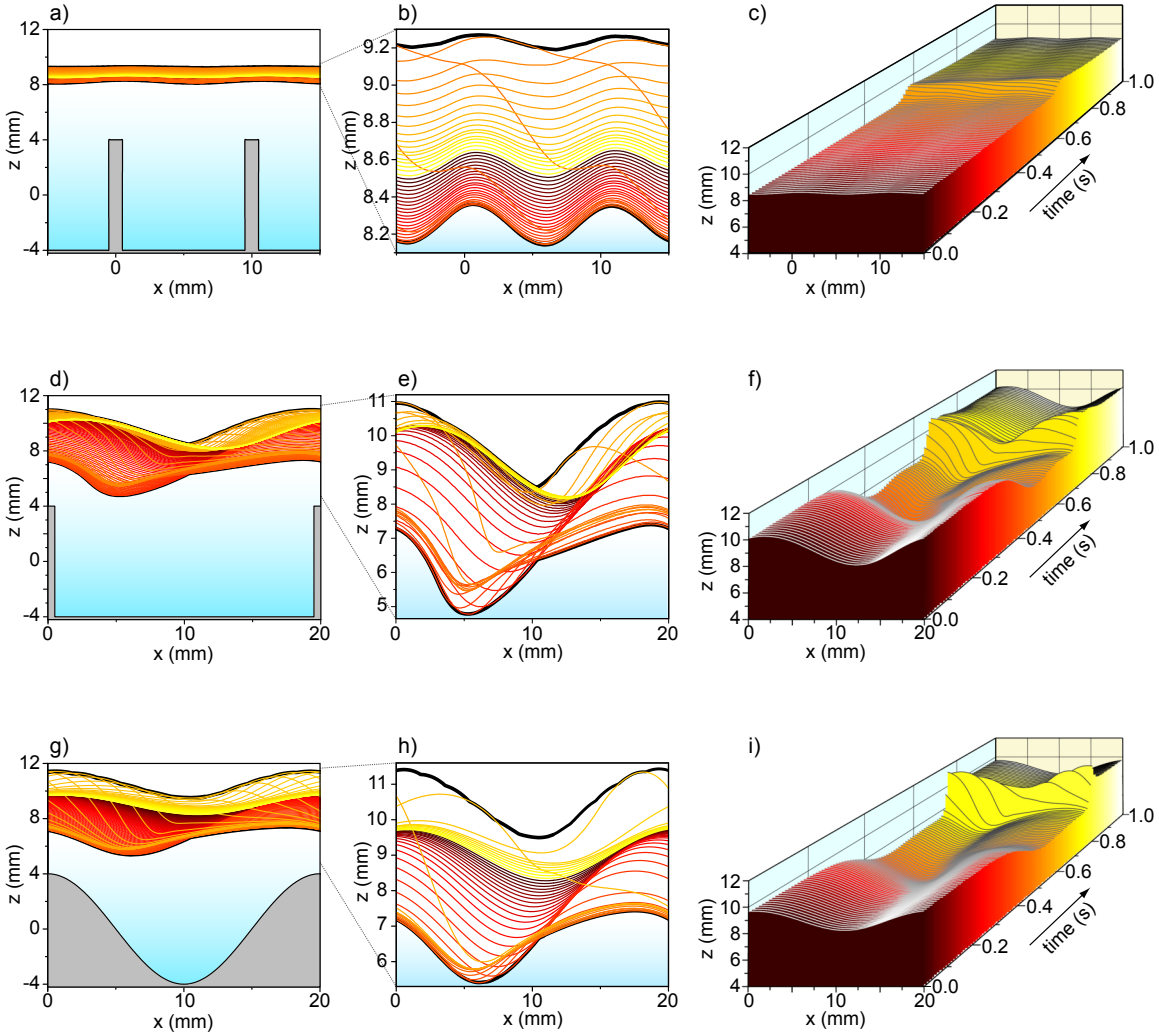

Figure 4.26.: Variation of the free surface during one period of the traveling wave ($A_e = 8\,\text{mm}$, $f = 1.0\,\text{Hz}$). (a) - (c): rectangular substrate with $L = 10\,\text{mm}$. (d) - (f): rectangular substrate with $L = 20\,\text{mm}$. (g) - (i): sinusoidal substrate with $L = 20\,\text{mm}$. The other system parameters are: $A = 8\,\text{mm}$, $\alpha = 10\,^\circ$, $\nu = 100.3\,\text{mm}^2/\text{s}$ and for (a) - (f) $W = 1\,\text{mm}$. (a), (d) and (g): The free surfaces are plotted for one recorded second with 200 frames per second. This leads to a band which represents the maximum and the minimum local height of the free surface. (b), (e) and (h) show the free surface enlarged for every fifth time step. (c), (f) and (i) show the evolution of the free surface for the same excerpt over time for each second time step. (f) and (i) show the depletion region in front of the wave crest. Modified and reprinted with permission from [122]. © AIP Publishing.

Strongly nonlinear disturbances

For strongly nonlinear traveling free surface waves, the linear stability chart is no longer adequate to describe the wave dynamics as large shifts of the neutral points appear (see Figure 4.24, $a \approx 0.7\,\text{mm}$). In particular, for traveling free surface waves of large free surface amplitudes, i.e. $a > 1\,\text{mm}$ in the present study, the disturbances couple to the underlying flow field and give rise to new flow phenomena, as recently outlined in the publication *"What makes the free surface waves over topography convex or concave? A study with Fourier analysis and particle tracking"* [122]. The present discussion on how strongly nonlinear disturbances can affect the stability of film flows relies on this publication.

Figure 4.26 shows how the free surface of the flow of *Elbesil 100* varied over time at a fixed position in streamwise direction when a saturated wave ($A_e = 8.0\,\text{mm}$, $f = 1.0\,\text{Hz}$) passed. Please see Section 3.2.2 for the experimental setup used for the time-dependent measurements of the free surface of the flow. The inclination angle and the topography amplitude were set to $\alpha = 10°$ and $A = 8\,\text{mm}$ respectively. The Figures 4.26a - 4.26c correspond to the rectangular substrate with $L = 10\,\text{mm}$ and $W = 1\,\text{mm}$, the Figures 4.26d - 4.26f correspond to the rectangular substrate with $L = 20\,\text{mm}$ and $W = 1\,\text{mm}$, and the Figures 4.26g - 4.26i correspond to the sinusoidal substrate with $L = 20\,\text{mm}$. One period of the traveling wave corresponds to 200 time steps. The time is color coded. The bold black contour lines in the Figures 4.26a, 4.26b, 4.26d, 4.26e, 4.26g and 4.26h highlight the local maximal and the local minimal height of the free surface during one period of the traveling wave. The width and the shape of the resulting band indicate how large the traveling wave was compared to the whole film and how uniform the local film thickness changed within one period of the corrugation while the wave passed.

The rectangular substrate with $L = 10\,\text{mm}$ shows a narrow and flat band. Hence, the penetration depth of the disturbance, i.e. the traveling wave, is small. For the rectangular substrate with $L = 20\,\text{mm}$, the free surface is heavily disturbed by the traveling wave. A similarly strong disturbance is visible for the sinusoidal substrate. Moreover, for the two substrates with $L = 20\,\text{mm}$, a depletion region in front of the wave is visible [125]. The rectangular substrate with $L = 10\,\text{mm}$ does not show a depletion region.

In order to show the aforementioned interaction between the traveling nonlinear surface wave and the underlying flow field single particle tracking measurements were carried out as described in Section 3.2.3. The pathlines of tracer particles were compared for the steady-state flow as well as for the flow perturbed by linear ($a < 0.1\,\text{mm}$, $f = 1.0\,\text{Hz}$) and strongly nonlinear ($a > 1.0\,\text{mm}$, $f = 1.0\,\text{Hz}$) traveling free surface waves. The experiments were performed for the three different substrates shown in Figure 4.26: the sinusoidal one with $L = 20\,\text{mm}$ and the two rectangular ones with $L = 10\,\text{mm}$ and $20\,\text{mm}$.

Figure 4.27 shows the measured pathlines and free surfaces of the flows over the three topographies shown in Figure 4.26. Both the steady-state flow (Figures 4.27a - 4.27c) and the strongly perturbed flow (Figures 4.27d - 4.27f) are shown. The results obtained when linear free surface perturbations ($a < 0.1\,\text{mm}$) were imposed to the flow are not shown separately, as they differ too little from the steady-state configuration to be distinguishable with the eye: no variation of the structure of the flow pattern was visible and the changes of the free surface amplitude over time were smaller than the width of the bold black line which represents the steady-state free surface in the Figures 4.27a - 4.27c. Hence, the Figures 4.27a - 4.27c represent both the steady-state flow and the flow perturbed by small, linear free surface disturbances.

In the Figures 4.27d - 4.27f, nonlinear free surface perturbations of large amplitudes a were imposed to the flow ($a > 1.0\,\text{mm}$, $f = 1.0\,\text{Hz}$). Hardly any interaction of the traveling wave with the stationary flow is visible in Figure 4.27d for the flow over the rectangular topography with $L = 10\,\text{mm}$. In contrast to this, the rectangular substrate with $L = 20\,\text{mm}$ showed strong interaction for the case of nonlinear disturbances, which can be seen in Figure 4.27e. The steady-state eddy, shown in Figure 4.27b, broke up when the traveling wave passed and mixed with the fluid of the traveling wave. Hence, the disturbance is not restricted to the free surface, as it is the case for small, linear waves. The penetration depth is large and the whole film flow is heavily disturbed by the wave traveling over the substrate. For the sinusoidal substrate, the strength of the interaction between the large traveling surface wave and the underlying flow field lies qualitatively between one of the two rectangular topographies (see Figure 4.27f).

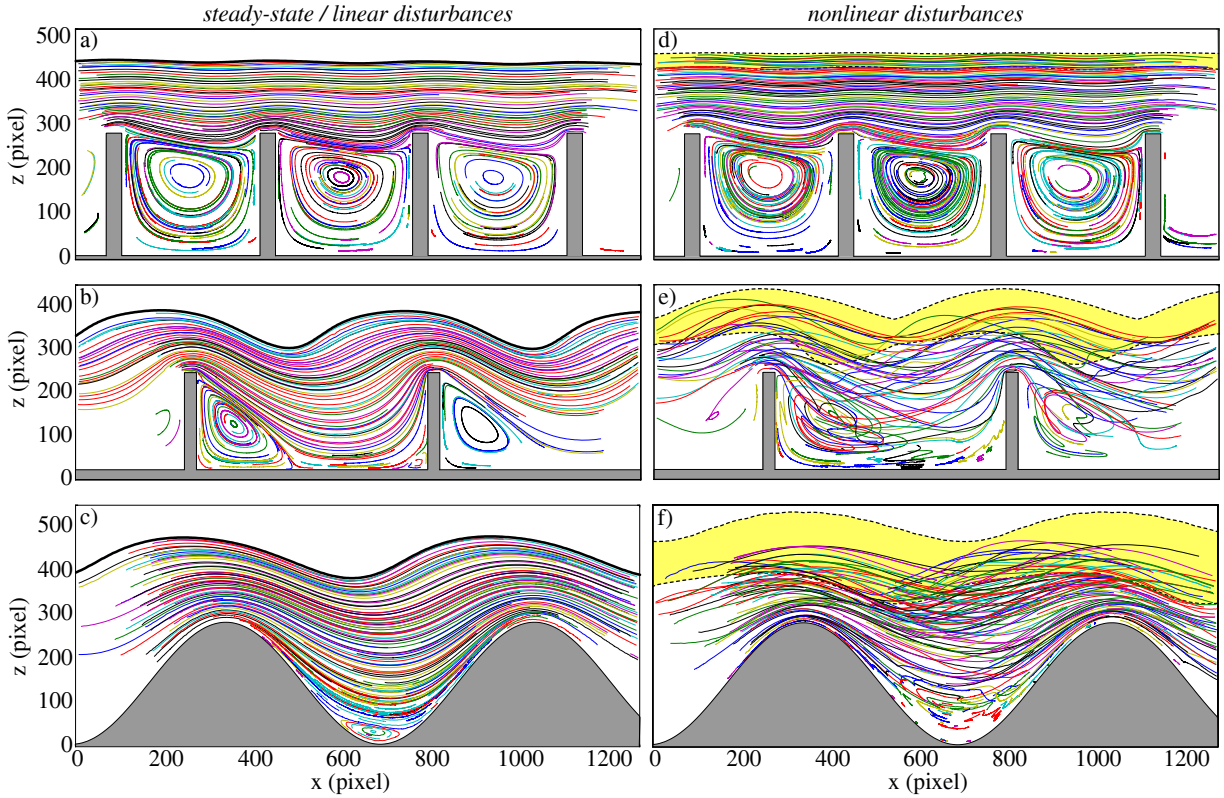

Figure 4.27.: (a) - (c) Particle tracking images for the steady-state flow over three different topographies. With the eye, the steady-state free surface and flow pattern are indistinguishable from the results obtained when linear disturbances ($A_e = 0.5\,\text{mm}$, $a < 0.1\,\text{mm}$, $f = 1.0\,\text{Hz}$) were imposed to the flow. For convenience, only the steady-state results are shown. (d) - (f) Particle tracking images for the flow perturbed by nonlinear disturbances ($A_e = 8.0\,\text{mm}$, $a > 1\,\text{mm}$, $f = 1.0\,\text{Hz}$). The yellow band indicates the variation of the free surface during one period of the traveling wave according to Figure 4.26. The main flow direction is from left to right. (a), (d) Rectangular substrate with $L = 10\,\text{mm}$. (b), (e) Rectangular substrate with $L = 20\,\text{mm}$. (c), (f) Sinusoidal substrate with $L = 20\,\text{mm}$. The other system parameters are: $A = 8\,\text{mm}$, $\alpha = 10\,°$, $\nu = 100.3\,\text{mm}^2/\text{s}$ and for (a), (b), (d), (e) $W = 1\,\text{mm}$. Modified by adding new measurement data and reprinted with permission from [122]. © AIP Publishing.

A comparison of the flow patterns and the free surface contours shown in the Figures 4.27a - 4.27c (steady-state flow & linear disturbances) and in the Figures 4.27d - 4.27f (nonlinear disturbances) illustrates that there are large differences. Dependent on the topography's specific shape, new phenomena arise when nonlinear waves perturb the flow. An eddy breakup is visible and the mixing provokes a drag force by flinging particles from the underlying steady-state flow into the traveling wave (Figures 4.27e, 4.27f). This mixing was found to be strongly dependent on the specific shape of the topographies (at equal topography amplitude and wavelength), resulting in a different shape and propagation of the traveling wave [122]. This constitutes a fundamental difference to the evolution of the linear free surface waves considered in the experiments on the flow's linear stability (Sections 4.1 - 4.3). For linear disturbances, the specific shape of the topography did not matter in general for wave propagation, i.e. flow stability (see Section 4.1).

The above-described finding that the topography's specific shape is decisive for the evolution of large-amplitude nonlinear waves crucially affects the validity of the stability cycle for nonlinear waves. First, the stability cycle was based on the method of the parallel strains of the variations of only the parameters α, ν, L, A and W (see Section 4.3.3, Figure 4.21). This method cannot

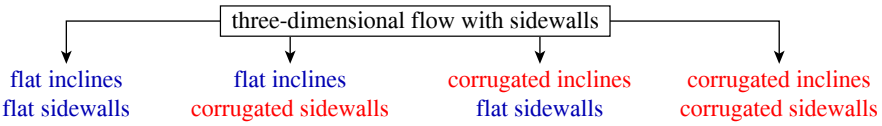

Figure 4.28.: Problem statements for the three-dimensional flow with sidewalls.

be equally applied when also the topography's specific shape is decisive for wave propagation. Second, it remains an open question if the flows' stability charts still match to the characteristic stability chart patterns defined in Section 4.3.2 when large-amplitude nonlinear free surface waves perturb the flow. Hence, the characteristic stability chart patterns and the stability cycle presented in Section 4.3 are not universally valid for film flows which are perturbed by strongly nonlinear large-amplitude traveling free surface waves.

The evolution of nonlinear traveling waves over inclined topographies is a highly demanding problem and has only been addressed sparsely, yet. As outlined above, this problem is inseparably coupled to the material exchange between the eddy and the flowing film above. Both issues remain challenging questions.

4.4.3. Three-dimensional flow with sidewalls

Real-world film flows always deal with channels of finite width, i.e. channels bounded by sidewalls. However, as the computational costs are high and the experiments are demanding, the effects of the sidewalls on both the steady-state channel flow as well as its stability were discussed only sparsely in the literature (please see the Sections 1.2.3 and 1.4.3). The intriguing question arises whether the characteristic stability chart patterns and the stability cycle (see Section 4.3), valid for two-dimensional flow over inclined topography, change when sidewalls are added to the system. Are the stabilizing and the destabilizing effects (Section 4.2) still the same in the vicinity of the sidewalls? Does the topography's specific shape (Section 4.1) still not matter in general for the flow's stability in the vicinity of the sidewalls?

In order to answer these intriguing questions, four different problem statements have to be distinguished when sidewalls are added to the system, as both the bottom of the channel and the sidewalls can be either flat or corrugated (see Figure 4.28). Although an all-embracing study of this great diversity of systems is beyond the scope of the present consideration, some examples are given below in order to outline the nontrivial effects which sidewalls can have on the steady-state channel flow and its linear stability.

Flat inclines & flat sidewalls

For two-dimensional gravity-driven flow, the linear stability of a viscous film flowing over a flat incline is represented by the classical long-wave type instability, i.e. the stability pattern I. Please see Figure 4.20 for the classification of the stability patterns. As long as the incline remains flat and infinitely extended, no pattern transitions are possible for the two-dimensional flow [11, 80].

When flat sidewalls are added to the system, the situation changes drastically as the symmetry is broken and two different cases have to be distinguished. On the one hand, as long as the Kapitza numbers are small [117] and the distance to the sidewalls is large compared to the intrinsic length scales [67], the effects of flat sidewalls on the linear stability of films flowing down flat inclines can be neglected, i.e. the flows can be considered as two-dimensional at the

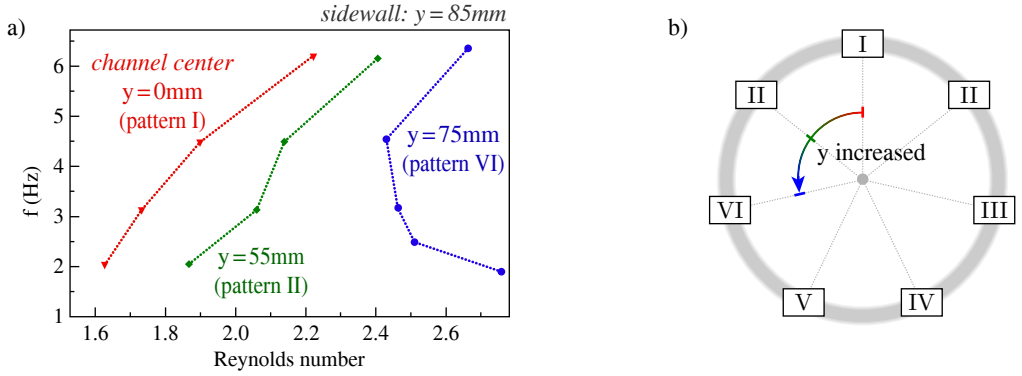

Figure 4.29.: (a) Linear stability charts for a Newtonian film flowing down a flat channel, inclined by 41° against the horizontal and bounded by flat sidewalls. The measurements were performed at the channel's center ($y = 0$) and at the off-center positions $y = 55$ mm and $y = 75$ mm (near to the sidewall). Data taken from [118]. (b) According to the classification presented in Figure 4.20 the pathway of the transitions between the different patterns is I → II → VI and fits to the stability cycle of two-dimensional film flows defined in Section 4.3.4.

channel's center. On the other hand, when the distance to the sidewall is reduced, a transition from a long-wave to a short-wave instability was reported by Pollak *et al.* [118] (please see Figure 4.29a). Indeed, their observations correspond to the pattern transitions I → II → VI along the stability cycle (please see Figure 4.29b).

The physical significance of this finding is its relevance for technical applications of film flows: at an adequate volume flux, the resulting short-wave type instability (pattern VI) corresponds to a band-pass, filtering long-wave and short-wave disturbances. This filtering can be achieved by simply narrowing a flat channel without the need to mount an undulated bottom. That way, the manufacturing of undulated substrates can be avoided and there are no troughs in which, for example, the fluid of biomedical flows can be trapped in recirculation zones for a long time until it finally degenerates.

Corrugated inclines & flat sidewalls

The effects of flat sidewalls on the linear stability of films flowing down corrugated inclines have not been addressed by any publication. It remains an open question if small Kapitza numbers are still sufficient to neglect the influence of the sidewalls on the flow's stability at the channel's center in general, as it is the case for the flow over a flat incline [117]. Moreover, in contrast to the flow over a flat incline, a curved contact line between the fluid and the sidewall appears due to the curved free surface of the steady-state flow over topography. It still remains in the dark how this free surface curvature affects the competing effects at the sidewalls[1] and concomitant the linear stability of the flow in the vicinity of the sidewalls.[2] Two intriguing questions arise, which will be considered in the following:

1) Are the measured linear stability charts presented in the Sections 4.1 - 4.3 significantly distorted by the presence of the sidewalls in the channels used in the experiments?

This question can be denied. The measured linear stability charts are in good agreement with the corresponding numerical results [108, 112, 113] (please also see Appendix A). The small

[1] For the flow over a flat incline, flat sidewalls give rise to a competition between the no-slip condition and the velocity overshoot due to the capillary elevation at the sidewalls [67].

[2] The shape of the steady-state free surface is decisive for the linear stability of the flow (Sections 4.1 and 4.2).

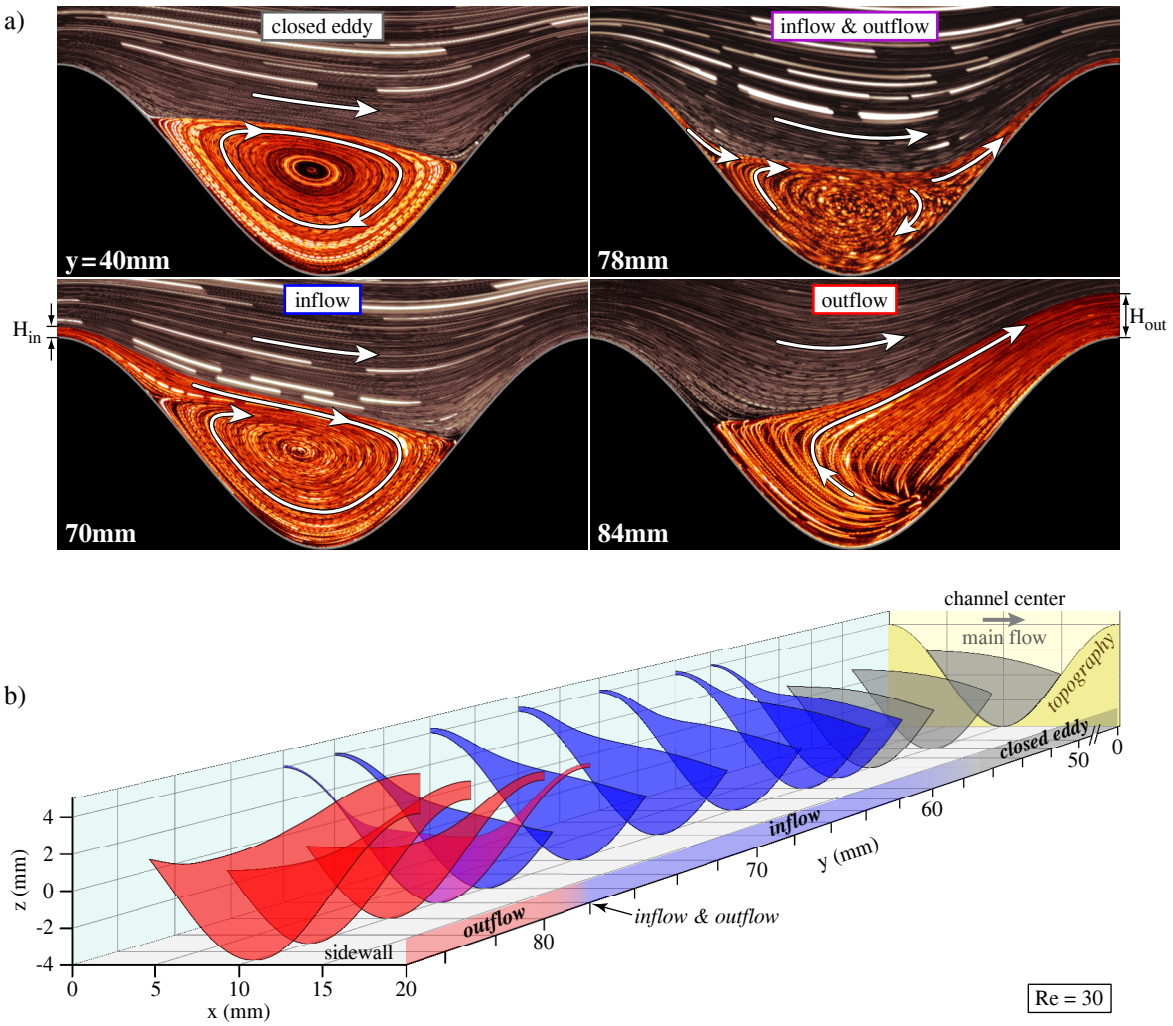

Figure 4.30.: (a) Measured steady-state flow patterns at four different crosswise distances y to the channel's center ($y = 0$). The sidewalls are located at $y = \pm 85$ mm. The arrows indicate the direction of the flow. The main flow is from left to right. The example corresponds to *Elbesil 145*, *Sin*, $A = 8$ mm, $L = 20$ mm, $\alpha = 10^\circ$ and $Re = 30$. At $y = 40$ mm, the eddy is closed and the pattern corresponds to the one at the channel's center. At $y = 70$ mm, the eddy breaks up and spiral-like pathlines indicate that material pours into the eddy (inflow). At $y = 84$ mm, material pours out of the eddy into the main flow (outflow). The inflection point between inflow and outflow was at $y = 78$ mm, where both phenomena appeared. (b) Scheme of the three-dimensional structure of the eddy. Gray: closed eddy. Blue: inflow. Red: outflow.

disparities between theory and experiment were attributed to the differences in the problem statements between theory (perturbation amplitude $a = 0$) and experiment ($a \neq 0$) as discussed in Section 4.4.2. As the calculations were performed for a two-dimensional system, the matching of the results of the numerical and the experimental approach indicates that the linear stability charts measured at the center of the channels were not distorted significantly by the presence of the sidewalls in the present study.

2) Are the sidewall effects qualitatively equal for both flat and corrugated inclines or do new phenomena appear, which significantly affect the steady-state flow and its linear stability?

To the author's knowledge, no precedent experimental or theoretical approach studied the effects of flat sidewalls on the steady-state flow over undulated inclines and its linear stability

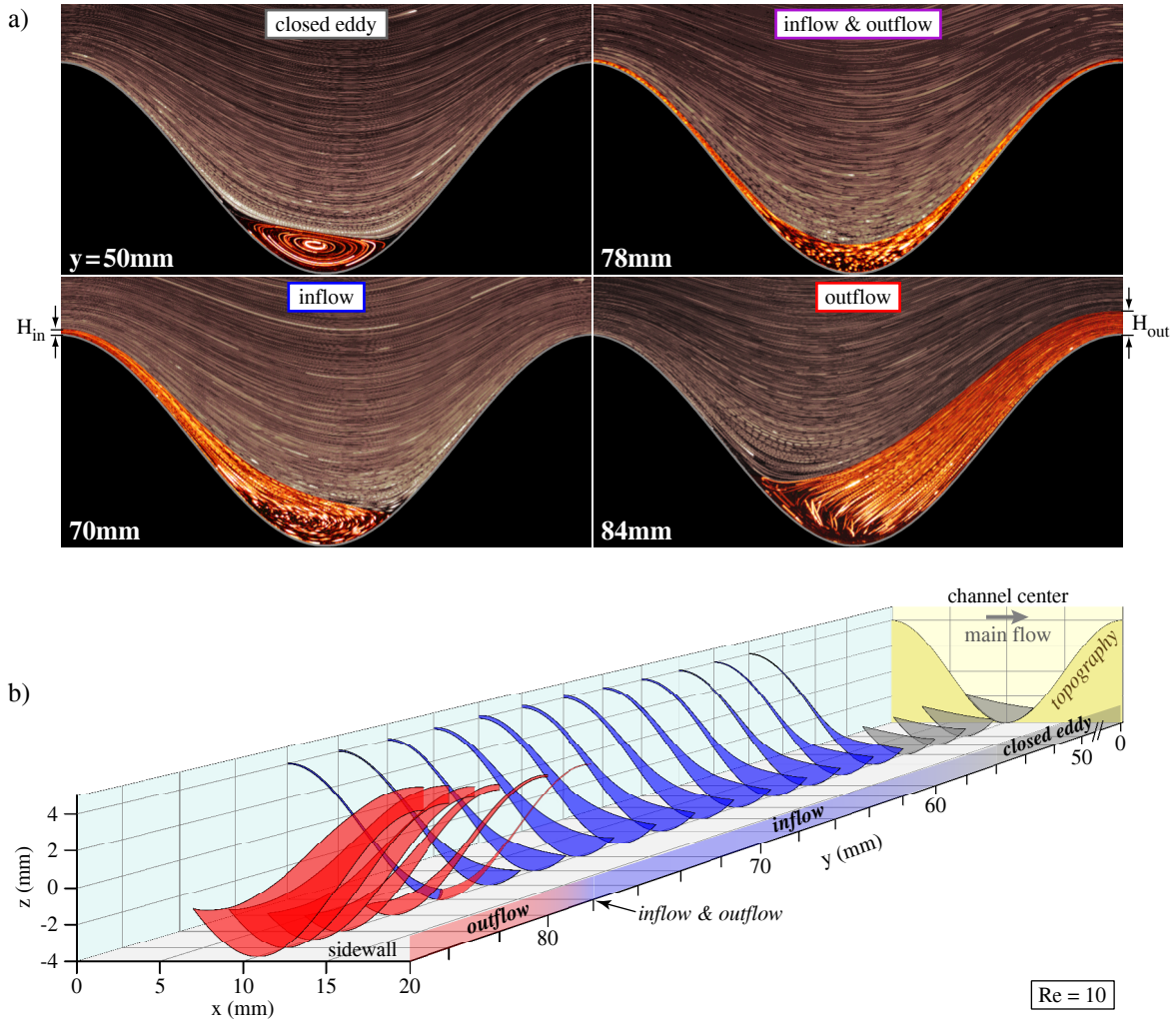

Figure 4.31.: (a) Measured steady-state flow patterns at four different crosswise distances y to the channel's center ($y = 0$). The sidewalls are located at $y = \pm 85$ mm. The arrows indicate the direction of the flow. The main flow is from left to right. The example corresponds to *Elbesil 145*, *Sin*, $A = 8$ mm, $L = 20$ mm, $\alpha = 10^\circ$ and $Re = 10$. At $y = 50$ mm, the eddy is closed and the pattern corresponds to the one at the channel's center. At $y = 70$ mm, the eddy breaks up and spiral-like pathlines indicate that material pours into the eddy (inflow). At $y = 84$ mm, material pours out of the eddy into the main flow (outflow). The inflection point between inflow and outflow was at $y = 78$ mm, where both phenomena appeared. (b) Scheme of the three-dimensional structure of the eddy. Gray: closed eddy. Blue: inflow. Red: outflow.

in-depth. In the following, first experimental findings on the effects of flat sidewalls on films over undulated inclines are presented with their relevance for the flow's linear stability being discussed.

According to the results presented in the Sections 4.1 and 4.2, the flow's linear stability is inextricably linked to the steady-state flow pattern, i.e. the steady-state free surface, which attunes as a consequence of eddy formation in the troughs. In order to figure out possible differences between the two-dimensional flow and the three-dimensional flow with sidewalls, the steady-state flow pattern in the vicinity of the sidewalls was visualized by measuring the pathlines of tracer particles at different y-positions between the channel's centerplane ($y = 0$) and the sidewall ($y = 85$ mm). Please see Section 3.2.3 for the corresponding measurement

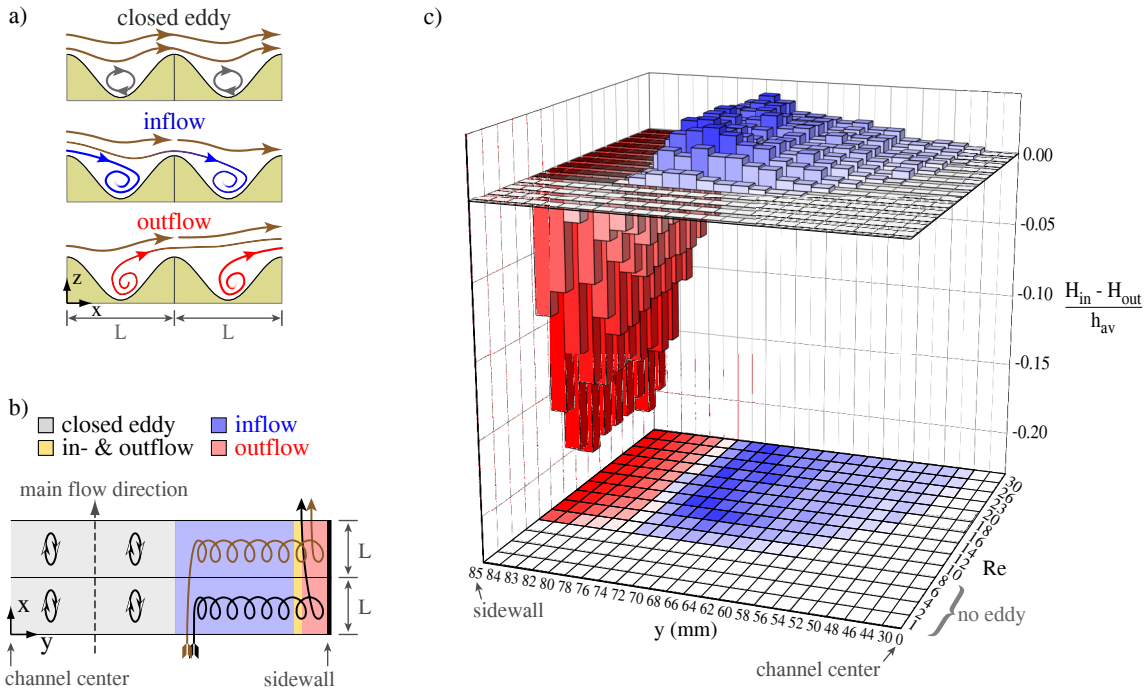

Figure 4.32.: Schematic side-view (a) and top-view (b) of the steady-state flow shown in the Figures 4.30 and 4.31. The mixing was found to be single-periodic in streamwise direction. The in- and outflow were found to be equal in each trough, i.e. to not alternate between consecutive troughs. (c) Dependence of the dimensionless mixing height $(H_{in} - H_{out})/h_{av}$ on the Reynolds number and the crosswise y-position. Near to the sidewall, the height of the outflow band H_{out} reached up to 20% of the average film thickness h_{av} at the channel's center.

technique to visualize the streamlines. The flow of *Elbesil 145* over a sinusoidal topography ($A = 8\,\text{mm}$, $L = 20\,\text{mm}$, $\alpha = 10°$) was chosen for demonstration purpose. As illustrated in Figure 4.30 for $Re = 30$, the flow pattern changes drastically in the vicinity of the sidewalls. Near to the center of the channel, the eddy remains closed and unaffected by the sidewalls. No material exchange between the eddy and the overlying main flow was visible. In the vicinity of the sidewalls steady-state mixing of the eddy and the main flow was observed. The symmetry break, induced by the presence of the sidewalls, led to a deformation of the vortex into a spiral. Spiral-like pathline-patterns, similar to those observed by Wierschem *et al.* [26] for creeping flow conditions (see Section 1.2.3), manifested.[3] Dependent on the distance to the sidewall either a closed eddy appeared, material poured into the eddy (inflow), material poured out of the eddy (outflow), or both inflow and outflow appeared.

In a first approach, the heights of the inflow band and the outflow band in z-direction at $x = \{0, L\}$ were chosen as a simple geometric measure to characterize the intensity of the material exchange between the eddy and the main flow. These heights were denoted as the mixing heights H_{in} (inflow) and H_{out} (outflow), as illustrated in Figure 4.30a and 4.31a. Both H_{in} and H_{out} significantly depended on the crosswise y-position. In the close vicinity of the sidewall, H_{out} reached its global maximum with $\max(H_{out}) >> H_{in}\ \forall y$. Decreasing the Reynolds number to $Re = 10$ provoked a shrinking of the eddy at the channel's center and the material exchange between the eddy and the main flow near the sidewall was lessend (see Figure 4.31). The overall structure of the three-dimensional flow pattern remained qualitatively unchanged for $Re = 10$,

[3] Despite the significantly differing boundary conditions, similar spiral-like pathline patterns were reported for the laminar flow through plane-symmetric sudden expansions [126].

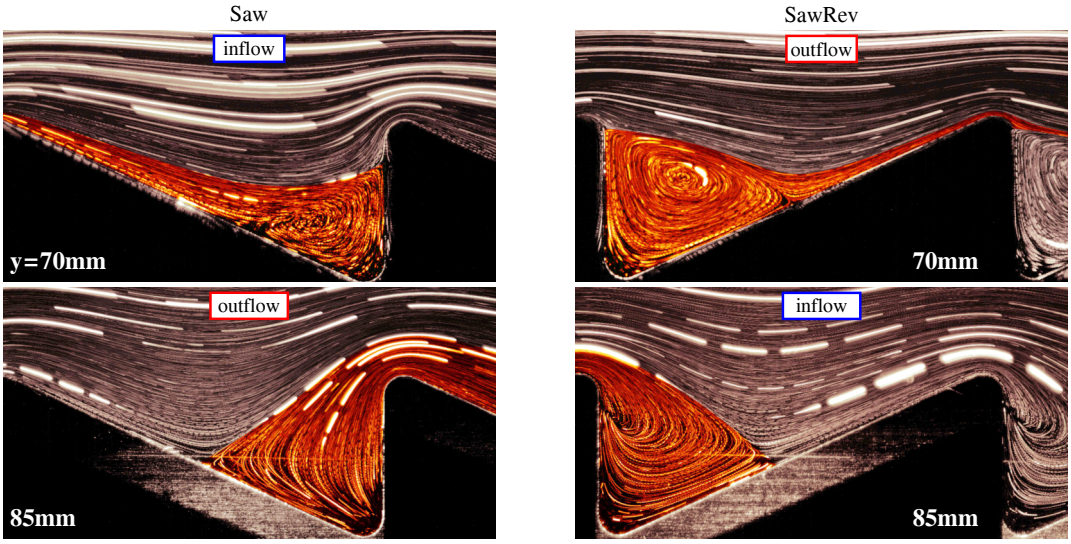

Figure 4.33.: Measured steady-state flow patterns at the two different crosswise positions $y = 70\,\text{mm}$ and $y = 85\,\text{mm}$ (at the sidewall) for the flow over sawtooth-like topographies with sidewalls. The examples correspond to *Elbesil 145*, $A = 8\,\text{mm}$, $L = 20\,\text{mm}$, $\alpha = 10°$, $Re = 30$ and *Saw* (left) and *SawRev* (right). The main flow is from left to right. Please note the inverted inflow and outflow regions for the *Saw* and the *SawRev* topography.

although the sidewall effects had a lower range in y-direction than for $Re = 30$ (please compare the Figures 4.30b and 4.31b). For $Re \leq 6$ no eddies and no mixing appeared at any crosswise position. However, as long as eddies were present, the range of the influence of the sidewalls on the steady-state flow was more than ten times larger than the generalized capillary length $2\sigma/(\rho g \cos\alpha) \approx 2\,\text{mm}$ [67] (please see, e.g., Figure 4.30b). Hence, the effects of flat sidewalls on the steady-state flow over the sinusoidal incline, which was considered for demonstration purpose, are significantly stronger than in the corresponding flow over a flat incline.

To ensure that the above-mentioned mixing was not provoked by a slight inclination of the channel against the y-axis, the pathline patterns were recorded on both sides of the channel, i.e. for $y > 0$ and $y < 0$. The structure of the flow pattern was found to be the same on both sides of the channel, e.g., at both sidewalls ($y = \pm 85\,\text{mm}$). Beyond, the main flow and the mixing phenomenon were single-periodic in the streamwise x-direction as illustrated in Figure 4.32a for side-view and in Figure 4.32b for top-view.

Although the three-dimensional flow pattern remained qualitatively unchanged by variations of the Reynolds number as long as eddies appeared at the channel's center, the dimensionless mixing height $(H_{in} - H_{out})/h_{av}$ depended on both the Reynolds number as well as the y-position (see Figure 4.32c). Near to the sidewalls, it reached about 20% of the average film thickness h_{av} at the channel's centerplane. This significant increase of the local flow rate has the potential to affect the free surface of the steady-state flow. As the steady-state free surface was found to be decisive for the flow's linear stability (see Sections 4.1 and 4.2), intriguing stability phenomena might appear as a consequence of the effects of the sidewalls.

Moreover, in contrast to the flow over the flat incline, where the stability pattern I is always present at the channel's center, the flow over undulated inclines can exhibit any of the stability patterns II - VI, there. It remains an open question how these stability patterns change when the distance to the sidewalls is reduced. Will the respective linear stability charts still follow the 'stability cycle' as it is the case for the flow over the flat incline in the vicinity of a flat sidewall?

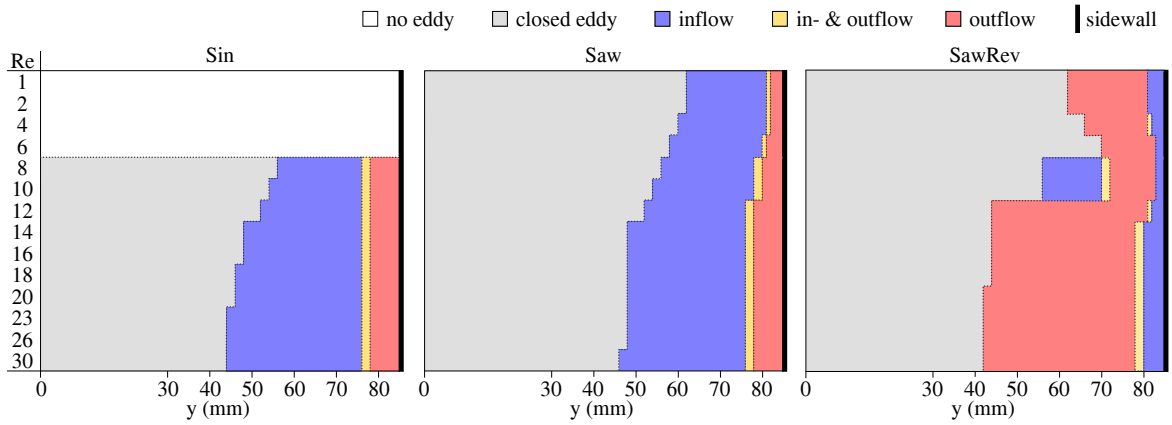

Figure 4.34.: Classification of the different flow regimes of the steady-state flow of *Elbesil 145* over the *Sin* (left), *Saw* (middle) and *SawRev* (right) topography of the amplitude $A = 8\,\text{mm}$, the wavelength $L = 20\,\text{mm}$ and the inclination $\alpha = 10°$. Dependent on both the Reynolds number and the crosswise y-position (channel center: $y = 0$; sidewall: $y = 85\,\text{mm}$) either no eddy (white), a closed eddy (gray), or an eddy breakup with inflow into the eddy (blue), outflow out of the eddy (red) or both in- and outflow (yellow) were determined. In contrast to Figure 4.32c, the charts shown in the present figure contain no information about the intensity of the mixing between the eddy and the main flow. They serve only to illustrate the qualitative similarities and differences of the flow patterns in the vicinity of the sidewalls, when the specific shape of the topography is altered.

The main result of Section 4.1 was that, as long as the steady-state free surface remains unchanged, the topography's specific shape does not significantly affect the linear stability of two-dimensional films flowing over undulated inclines. Is this result still valid for the three-dimensional flow in the vicinity of flat sidewalls? As illustrated in Figure 4.33, the mixing characteristics significantly differ when the specific shape of the topography is altered without changing its amplitude or wavelength. While for the *Sin* and *Saw* topography the inflow and outflow regions remained qualitatively similar, they differed decidedly for the *SawRev* topography (see Figure 4.34). For the *SawRev* topography, the inflow (not the outflow) occurred

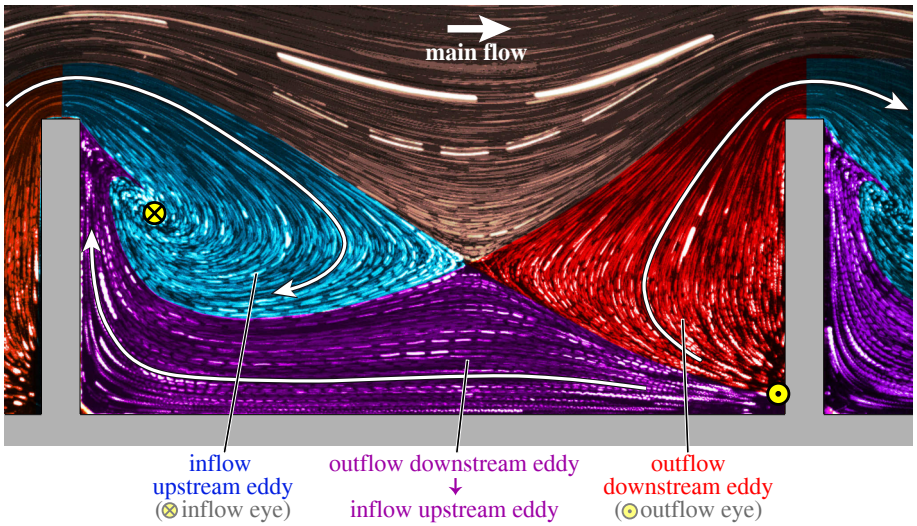

Figure 4.35.: Measured steady-state flow pattern of *Elbesil 145* at $Re = 30$ flowing over a rectangular topography ($A = 8\,\text{mm}$, $L = 20\,\text{mm}$, $W = 1\,\text{mm}$, $\alpha = 10°$) in the close vicinity of the sidewall ($y = 85\,\text{mm}$). For convenience, the different flow regimes are color coded. The arrows indicate the direction of the flow.

in the close vicinity of the sidewalls. For the *Rec* topography ($W = 1\,\mathrm{mm}$), the mixing phenomenon is even more complex (see Figure 4.35) as multiple eddies can appear in the troughs at the channel's center (see Figure 4.4b and 4.5). Following the same argumentation as in the previous paragraph, it will be interesting to see how the different types of mixing in channel flows over inclined topographies affect the steady-state free surface and thereby also the linear stability of the flow in the vicinity of the sidewalls. As real-world systems are always bounded by sidewalls, these findings would be appreciated, e.g., in the manufacturing of microelectronic devices or optical coatings.

Flat or corrugated inclines & corrugated sidewalls

The effects of corrugated sidewalls on films flowing down flat or corrugated inclines have not yet been addressed. Neither the steady-state solution of this problem, nor its stability against time-dependent free surface perturbations have been considered, although these highly demanding problem statements are closest related to real-world systems in the nature and in engineering technological applications of film flows. It will be interesting to see how the great challenge of calculating or measuring the time-dependent, fully three-dimensional free surface flow with corrugated sidewalls will be overcome.

4.4.4. Conclusions

The characteristic stability chart patterns and the stability cycle presented in Section 4.3 were found to be valid for all two-dimensional Newtonian films, which are perturbed by linear free surface waves and flowing down periodically undulated inclines. Yet, it remained an open question whether similar phenomena can appear beyond the linear stability of two-dimensional Newtonian film flows, e.g., for non-Newtonian fluids, nonlinear waves and three-dimensional channel flows with sidewalls as bounding topography. In the present Section 4.4, these three exemplary systems were briefly considered for demonstration purpose to unveil what can be beyond the linear stability of two-dimensional Newtonian films. For this sake, the sparse literature on this topic was studied and new experiments were performed. As the results presented in the Sections 4.1 and 4.2 provided the experimental evidence that the flow's stability is inextricably coupled to the phenomena of the steady-state flow, both were considered together wherever the available literature and the experimental setups permitted it. That way, new phenomena like, e.g., a mixing between the eddies in the troughs of the undulations and the overlying main flows were uncovered, with their effects on the flow's stability being briefly discussed. Although an in-depth investigation of non-Newtonian films, nonlinear disturbances and sidewall effects on channel flows is beyond the scope of the present dissertation, all available findings indicate that both the characteristic stability chart patterns and the stability cycle are, with some restrictions, still valid beyond the linear stability of two-dimensional Newtonian film flows.

5. Summary and Conclusions

The present thesis provides new insights into the effects of topographies on the stability of gravity-driven viscous film flows. Particular focus lies on the influence of periodic, one-dimensional topographies on the linear stability of two-dimensional Newtonian film flows, which are solely driven by gravity. Comprehensive and thorough experimental investigations unveiled new stability phenomena far beyond the well-known Nusselt regime and associated these phenomena to the structure of the underlying steady-state flow. The new experimental results were combined with all existing analytical, numerical and experimental findings on this complex problem. That way, the flow phenomena could be attributed to fundamental mechanisms, which determine the flow dynamics. The aim of the present study was to characterize all these results for the sake of unveiling a universal principle, being able to describe and unify all findings on the stability of viscous films flowing over inclined topographies.

First, the linear stability of gravity-driven two-dimensional Newtonian films flowing over five differently shaped topographies was measured, while the liquid and the inclination angle were retained. All topographies shared the same amplitude and wavelength but exhibited different specific shapes, e.g., sinusoidal, rectangular or sawtooth-like. Despite the significantly differing topography shapes, all linear stability charts were equal, aside from small deviations. In order to understand this astonishing finding, the associated flow fields of the corresponding steady-state flows were scrutinized. The upper boundary of the steady-state flowing domain, constituted by the free surface, as well as its lower boundary, defined by the substrate and the eddies in the troughs, were determined. The lower boundaries of the flowing domain differed decidedly for the five highly diverse topographies. Despite this severe disparity of the lower boundaries of the flowing domain, the free surface and concomitant the free surface stability remained unaffected. However, this statement cannot be true for all topographies of equal amplitude and wavelength. A gedankenexperiment led to the conclusion that when, e.g., the tip width of the rectangular undulations increases and finally reaches the wavelength of the topography, both the free surface shape and the flow's linear stability have to change, as the flow then corresponds to the flow over a flat incline. Consequently, the topography's specific shape does not matter in general for the linear stability of film flows, as long as the free surface remains unchanged. In other words, the free surface stability of gravity-driven film flows cannot be manipulated in general by even strong variations of the topography's specific shape. Indeed, this finding is of imperative importance for a wide range of technical applications of film flows, ranging from coating industries to energy-converting systems, where the specific shape of the topography over which the fluid moves cannot be modified freely.

In the subsequent parameter study, the linear stability charts of gravity-driven film flows over inclined topographies were found to exhibit a complex inner topology. The formation of stable and unstable isles in the linear stability chart and transitions from long-wave to short-wave instabilities are only a few of many examples. In order to illuminate these findings, the scope of the experiments was significantly enhanced compared to all previous approaches: either the depth of sinusoidal undulations was gradually increased or the tip width of rectangular corrugations was gradually decreased. Variations of the inclination of the channel, the viscosity of the liquid and the wavelength of the topography followed. This comprehensive approach

provided detailed experimental data on the stability charts as well as on the free surface shapes and the velocity fields of the corresponding steady-state flows. The complexity of the shape of the linear stability chart was found to grow when either the amplitude of the topography was increased or its tip width was decreased. Besides, it depended in a nontrivial way on the viscosity of the liquid and on the wavelength and inclination of the topography. The measurements of the steady-state free surfaces and velocity fields attributed the complex shapes of the stability charts to the simultaneous presence of stabilizing as well as destabilizing effects provoked by the topography. The stabilization of the flow due to an increased mean film thickness and the destabilization of the flow due to resonance of the steady-state free surface were shown to be competing effects. In particular, the unstable isle in the linear stability charts of gravity-driven viscous films over inclined periodical structures was attributed to the above-mentioned resonance phenomenon: the core of the unstable isle appeared at the same Reynolds number, where also the maximum of the first free surface harmonic amplitude was located. Decreasing the inclination or the viscosity, or increasing the topography wavelength shifted the resonance maximum and thus the unstable isle to higher Reynolds numbers. That way, the stabilizing effect of the increased mean film thickness dominated at low Reynolds numbers and the flows were more stable against long-wave perturbations than the corresponding Nusselt flows. Hence, the interplay between the topography's amplitude, wavelength, inclination, and tip width as well as the liquid's viscosity determines whether the stabilizing or the destabilizing effect prevails. This interaction between competing effects cannot be approximated properly by the well-known Nusselt solution of the unidirectional flow over a flat incline: Reducing a film flow over deep corrugations to a Nusselt flow would disregard the significantly differing steady-state flow phenomena, which govern the flow's stability – far beyond the limits of Nusselt's theory.

The aim of the next part of the present thesis was to provide a universal guide on how to tune the linear stability of gravity-driven two-dimensional Newtonian films flowing over inclined topographies. In other words, a fundamental question was considered: Is there a universal principle, being valid to describe the parametric evolution of the flow's linear stability chart for variations of different system parameters? For this sake, first, all experimental and numerical stability charts available in the literature were screened. In a second step, experiments were performed to fill the gaps which remained after the parameter spaces of the independent, precedent investigations were combined. That way, a set of six characteristic stability chart patterns was identified to be sufficient to describe and unify all previous results on the linear stability of viscous films flowing over undulated inclines. Variations of the liquid's viscosity or the topography's amplitude, wavelength, tip width or inclination against the horizontal led to transitions between these six patterns. The pattern transitions shift unstable and stable flow regimes and can provoke, e.g., crucial flow stabilization at high Reynolds numbers, important in physical and technical applications like coating or biofilm formation. By considering the whole set of transitions a universal pathway – the stability cycle – was unveiled, along which the linear stability charts of all considered film flows evolved when the above-mentioned system parameters were changed. Hence, the stability cycle can be interpreted as a universal guide on how to tune the linear stability of gravity-driven viscous films in a way which is desired or required, e.g., by energy-converting systems like falling-film heat exchangers, or by coating applications in medical, optical, biochemical, or semiconductor industries.

The characteristic stability chart patterns and the stability cycle were found to be valid for all two-dimensional Newtonian films which are perturbed by linear free surface waves and flowing down periodically undulated inclines. There are no contradicting observations reported,

falsifying their universal character. However, it remained an open question whether similar phenomena can appear for differing systems with, e.g., non-Newtonian fluids, nonlinear waves, or three-dimensional channel flow with sidewalls as bounding topography. In the last part of the present dissertation, these three exemplary systems were briefly considered to unveil what is beyond the linear stability of two-dimensional Newtonian films. For this sake, the sparse literature on this topic was studied and new experiments were performed. As the results presented previously in this thesis provided the experimental evidence that the flow's linear stability is inextricably coupled to the phenomena of the steady-state flow, both were considered together wherever the available literature and the experimental setups permitted it. Phenomena like an eddy breakup due to traveling free surface waves were uncovered with their effects on the flow's stability being briefly discussed. Although an in-depth investigation of non-Newtonian films, nonlinear disturbances and sidewall effects is beyond the scope of the present work, all available findings indicate that both the characteristic stability chart patterns and the stability cycle are, with some restrictions, still valid beyond the linear stability of two-dimensional Newtonian films. However, as this statement is based on a small sample of studied systems, it cannot claim the same universality and completeness as the findings on the linear stability of two-dimensional Newtonian films over inclined topographies. Yet, these observations can serve as first indications for what is beyond the linear stability of two-dimensional Newtonian films. As the computations and the experiments dealing with non-Newtonian fluids, nonlinear waves and three-dimensional channel flows are highly demanding, it will be interesting to see how the great challenge of exploring the limits of the validity of the stability cycle will be faced in the future.

As a final remark, the author would like to highlight the physical significance of the characteristic stability patterns and the universal stability cycle: both together can indeed be interpreted as a universal guide on how to tune the stability of viscous films flowing over inclined topographies in a way which is desired or required by the application. With the results presented in the present dissertation, previous limitations can be circumvented and the huge potential of structured substrates for passive flow stabilization is ready to be exploited.

A. All available systems and stability charts

A.1. Variation of the inclination angle α of the channel

A.1.1. Table of all available systems for variation of α

Nr.	$\nu(\mathrm{mm}^2/\mathrm{s})$	*shape*	$A(\mathrm{mm})$	$L(\mathrm{mm})$	$W(\mathrm{mm})$	$\alpha(\mathrm{deg})$
1	100	*Sin*	8	20	–	$4.1^\star$, 5.0, 8.0, 10.0, 14.0, 18.0, $21.0^\star$, 24.9, $36.7^\star$
2	144	*Sin*	8	20	–	$7.0^\star$, 10.0, 14.0, 17.0, 21.0, 23.0, 36.7
3	65	*Sin*	8	20	–	$4.1^\star$, $8.5^\star$, 10.0
4	144	*Sin*	4	20	–	10.0, $17.0^\star$
5	144	*Flat*	–	–	–	$10.0^\star$, 14.0, 17.0, 21.0, 23.0, 36.7

Table A.1.: Systems for which the linear stability of a gravity-driven film flow over topography was investigated at different inclination angles α of the channel. Data taken from [76, 107, 108, 110, 113, 122]. New experiments [114] are marked by a star ($\star$). The numbers on the left-hand side correspond to the numbers in the Figures 4.21 and A.1. Modified and reprinted with permission from [114].

A.1.2. All available stability charts for variation of α

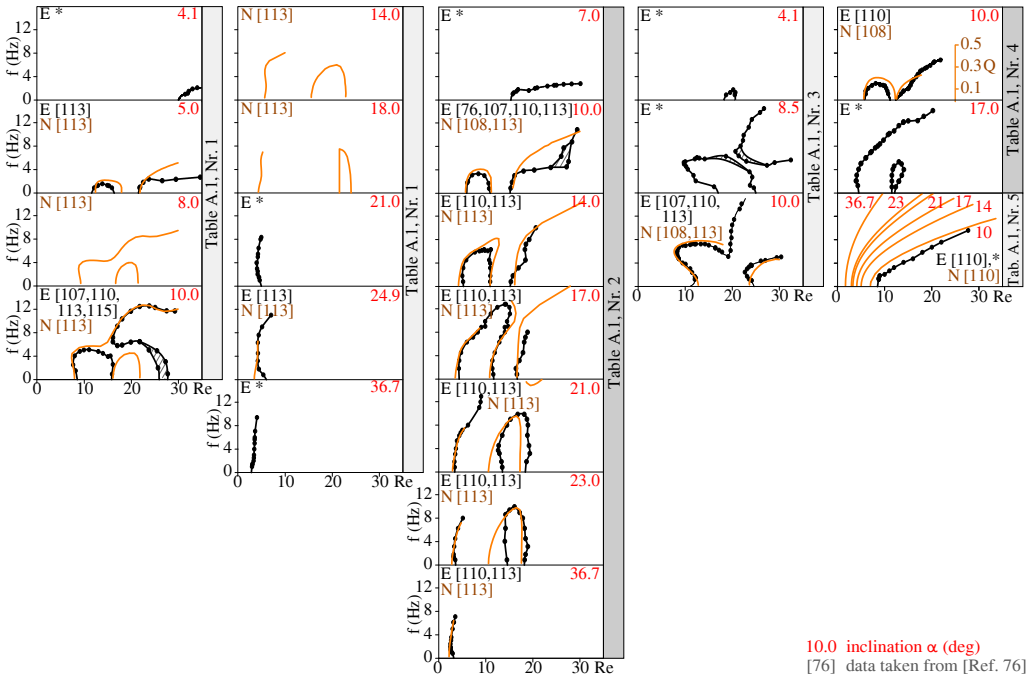

Figure A.1.: Linear stability at different inclination angles α. The charts include experiments (E) and numerics (N) taken from [76, 107, 108, 110, 113, 122] and new experiments ($\star$) from [114]. Hatched markings denote measurement uncertainties. Computed neutral curves are shown as $Q(Re)$ if no relation between Q and f was published. Modified and reprinted with permission from [114]. © AIP Publishing.

A.1.3. Pathway of the stability for variation of α

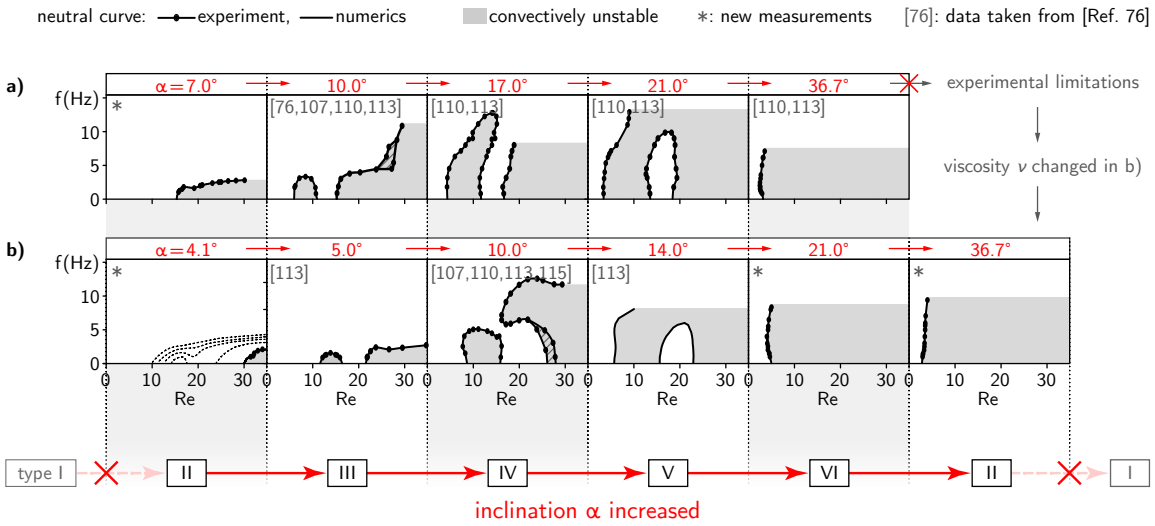

Figure A.2.: Evolution of the stability chart with the inclination α increasing from left to right inside (a) and (b) while all other parameters *shape*, ν, L, A, W were kept constant. The given examples correspond to Sin, $A = 8\,\mathrm{mm}$, $L = 20\,\mathrm{mm}$ and (a) $\nu = 144\,\mathrm{mm}^2/\mathrm{s}$ or (b) $\nu = 100\,\mathrm{mm}^2/\mathrm{s}$. The measured stability charts shown in (a) and (b) were assigned to the schematic chart patterns I - VI defined in Figure 4.20. The red arrows symbolize the transitions between different patterns of stability charts which occurred when α was increased. Transitions between pattern I and II are not possible (red cross) as explained in Section 4.3.3. Hatched markings denote measurement uncertainties. Contour lines of the growth rate b are shown as dashed lines in steps of $\Delta b = 0.5\,\mathrm{m}^{-1}$ for $\alpha = 4.1\,^\circ$ in (b). Modified and reprinted with permission from [114]. © AIP Publishing.

A.2. Variation of the viscosity ν of the liquid

A.2.1. Table of all available systems for variation of ν

Nr.	α(deg)	*shape*	A(mm)	L(mm)	W(mm)	ν(mm^2/s)
1	10.0	Sin	8	20	–	65, 80, 100, 119, 123, 144
2	4.1	Sin	8	20	–	65*, 100*
3	21.0	Sin	8	20	–	100*, 144
4	36.7	Sin	8	20	–	100*, 144
5	10.0	Rec	8	20	1	100, 144*
6	10.0	Rec	8	40	1	100*, 144*
7	10.0	Sin	4	20	–	100*, 144
8	10.0	Sin	2	20	–	65*, 144
9	10.0	Rec	8	10	1	100*, 144*
10	10.0	Rec	8	30	1	100*, 144*
11	10.0	Rec	8	20	10	100*, 144*
12	10.0	Saw	8	20	–	100*, 144*
13	10.0	$Flat$	–	–	–	65*, 100*, 144*

Table A.2.: Systems for which the linear stability of a gravity-driven film flow over topography was investigated at different viscosities ν of the liquid. Data taken from [76, 107, 108, 110, 112, 113, 122]. New experiments [114] are marked by a star ($\star$). The numbers on the left-hand side correspond to the numbers in the Figures 4.21 and A.3. Modified and reprinted with permission from [114].

A.2.2. All available stability charts for variation of ν

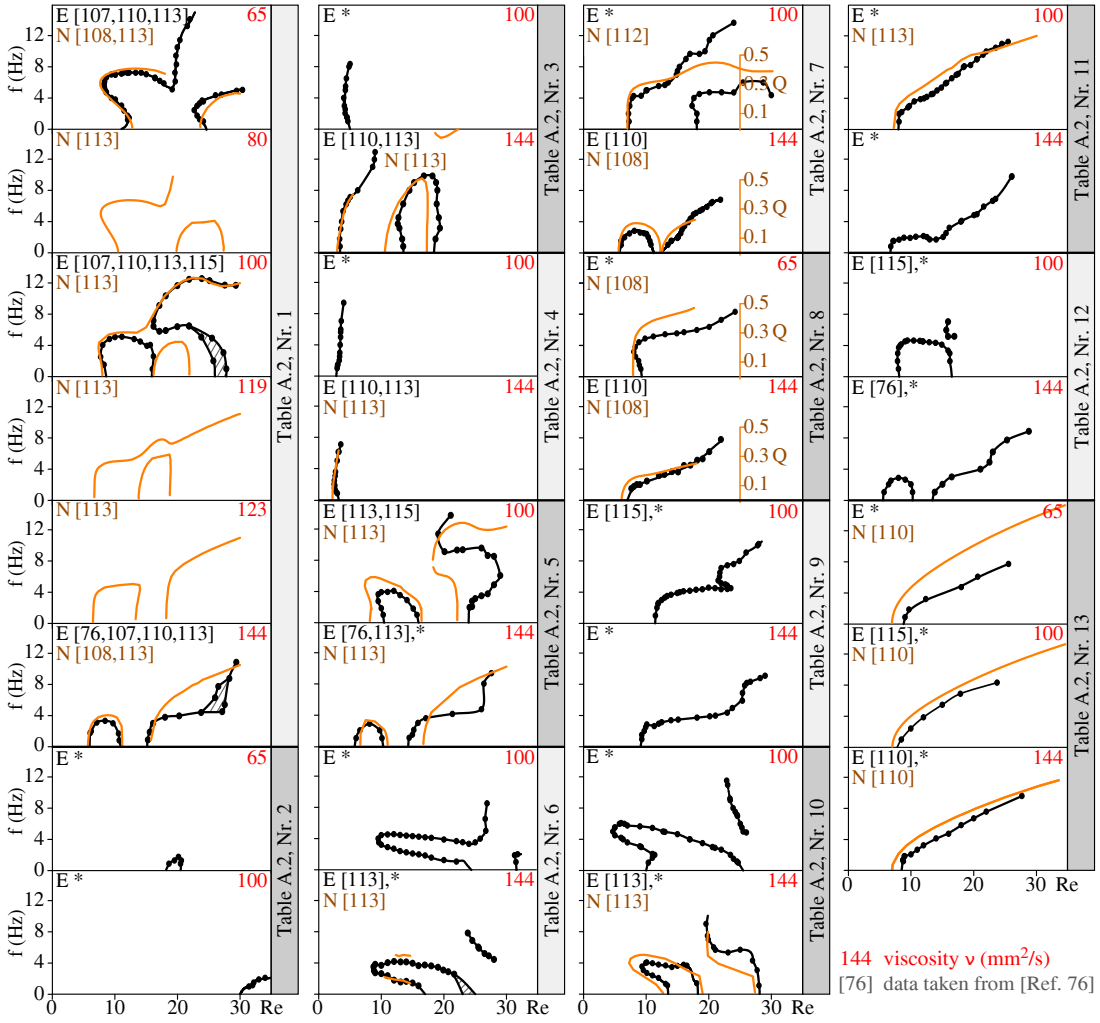

Figure A.3.: Linear stability at different viscosities ν. The charts include experiments (E) and numerics (N) taken from [76, 107, 108, 110, 112, 113, 122] and new experiments ($\star$) from [114]. Hatched markings denote measurement uncertainties. Computed neutral curves are shown as $Q(Re)$ if no relation between Q and f was published. Modified and reprinted with permission from [114]. © AIP Publishing.

A.2.3. Pathway of the stability for variation of ν

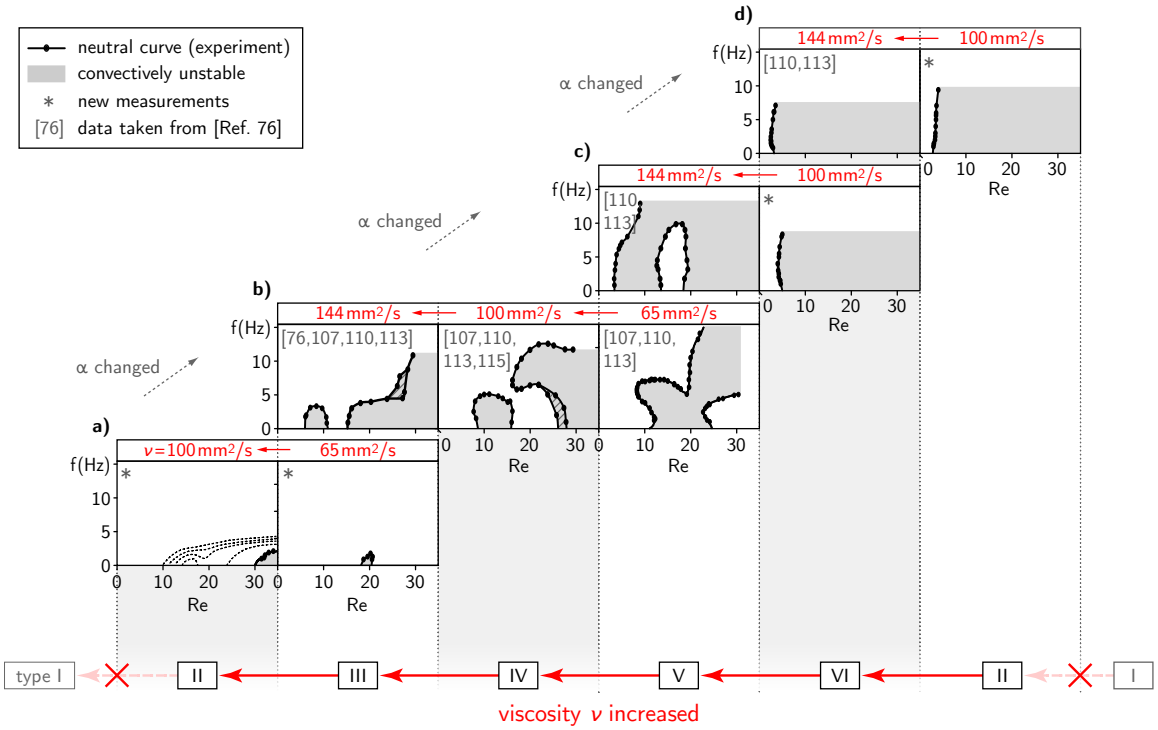

Figure A.4.: Evolution of the stability chart with the viscosity ν increasing from right to left inside each of the figures (a) - (d), while all other parameters *shape*, α, L, A, W of the system were retained. The measured stability charts were assigned to the schematic chart patterns I - VI defined in Figure 4.20. The red arrows symbolize the transitions between different patterns of stability charts which occurred when ν was increased. Transitions between pattern I and II are not possible (red cross) as explained in Section 4.3.3. The given examples correspond to *Sin*, $A = 8\,\mathrm{mm}$, $L = 20\,\mathrm{mm}$ and (a) $\alpha = 4.1^\circ$, (b) $\alpha = 10.0^\circ$, (c) $\alpha = 21.0^\circ$ and (d) $\alpha = 36.7^\circ$. Hatched markings denote measurement uncertainties. Contour lines of the growth rate b are shown as dashed lines in steps of $\Delta b = 0.5\,\mathrm{m}^{-1}$ for $\nu = 100\,\mathrm{mm}^2/\mathrm{s}$ in (a). Modified and reprinted with permission from [114]. © AIP Publishing.

A.3. Variation of the wavelength L of the topography

A.3.1. Table of all available systems for variation of L

Nr.	$\nu(\mathrm{mm}^2/\mathrm{s})$	$\alpha(\mathrm{deg})$	*shape*	$A(\mathrm{mm})$	$W(\mathrm{mm})$	$L(\mathrm{mm})$
1	144	10.0	*Rec*	8	1	$0^\star$, $10^\star$, $20^\star$, $30^\star$, $40^\star$, $\infty^\star$
2	100	10.0	*Rec*	8	1	$0^\star$, $10^\star$, 20, $30^\star$, $40^\star$, $100^\star$, $\infty^\star$
3	144	10.0	*Sin*	8	–	$0^\star$, 20, 30, 40, $\infty^\star$
4	100	10.0	*Rec*	8	$L/2$	$0^\star$, $20^\star$, $40^\star$, $200^\star$, $\infty^\star$

Table A.3.: Systems for which the linear stability of a gravity-driven film flow over topography was investigated at different corrugation wavelengths L. Data taken from [76, 107, 108, 110, 113, 122]. New experiments [114] are marked by a star ($\star$). The numbers on the left-hand side correspond to the numbers in the Figures 4.21 and A.5. Modified and reprinted with permission from [114].

A.3.2. All available stability charts for variation of L

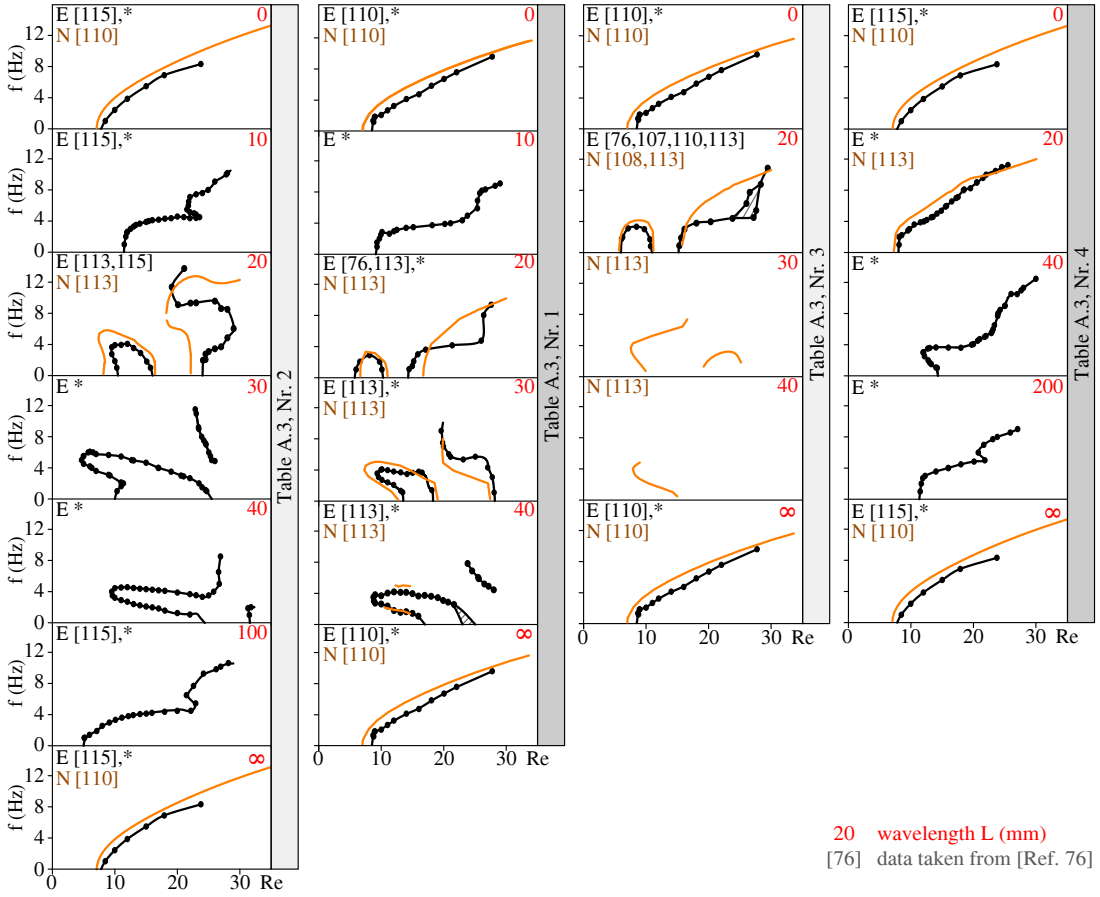

Figure A.5.: Linear stability at different corrugation wavelengths L. The charts include experiments (E) and numerics (N) taken from [76,107,108,110,113,122] and new experiments ($\star$) from [114]. Hatched markings denote measurement uncertainties. Modified and reprinted with permission from [114]. © AIP Publishing.

A.3.3. Pathway of the stability for variation of L

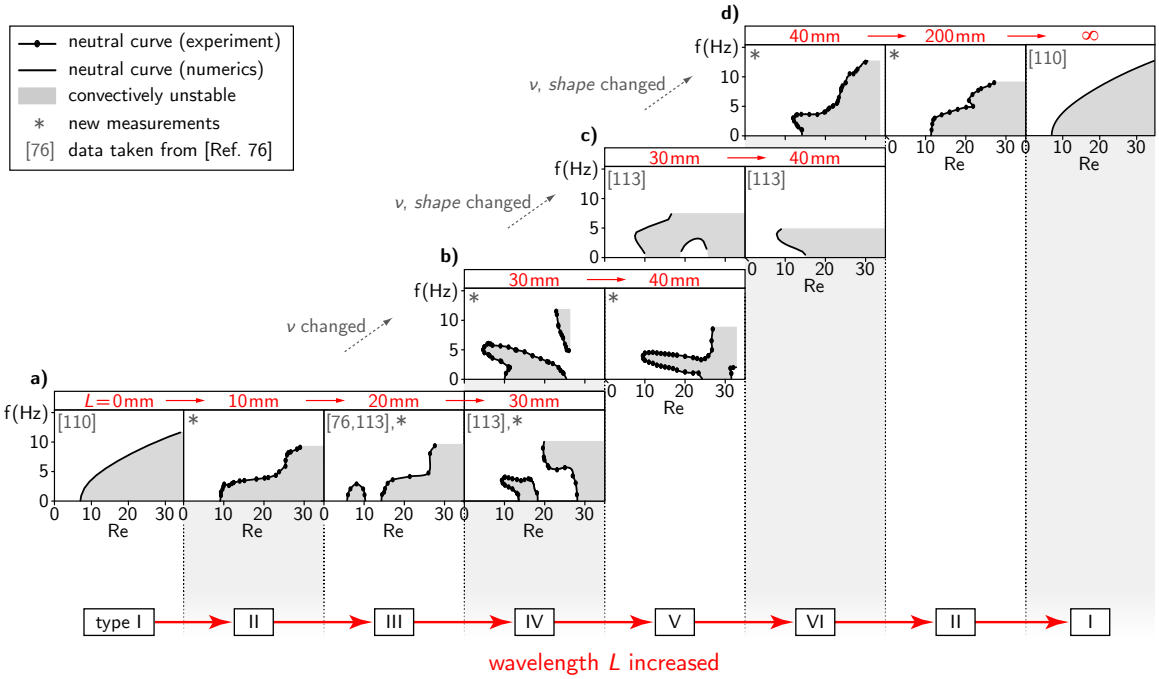

Figure A.6.: Evolution of the stability chart with the wavelength L of the topography increasing from left to right inside each of the figures (a) - (d), while all other parameters *shape*, α, ν, A, W of the system were retained. The measured stability charts were assigned to the schematic chart patterns I - VI defined in Figure 4.20. The red arrows symbolize the transitions between different patterns of stability charts which occurred when L was increased. The given examples correspond to $A = 8\,\mathrm{mm}$, $\alpha = 10.0\,^\circ$ and (a) *Rec*, $\nu = 144\,\mathrm{mm}^2/\mathrm{s}$, $W = 1\,\mathrm{mm}$, (b) *Rec*, $\nu = 100\,\mathrm{mm}^2/\mathrm{s}$, $W = 1\,\mathrm{mm}$, (c) *Sin*, $\nu = 144\,\mathrm{mm}^2/\mathrm{s}$ and (d) *Rec*, $\nu = 100\,\mathrm{mm}^2/\mathrm{s}$, $W = L/2$. Modified and reprinted with permission from [114]. © AIP Publishing.

A.4. Variation of the amplitude A of the topography

A.4.1. Table of all available systems for variation of A

Nr.	$\nu(\mathrm{mm}^2/\mathrm{s})$	$\alpha(\mathrm{deg})$	*shape*	$L(\mathrm{mm})$	$W(\mathrm{mm})$	$A(\mathrm{mm})$
1	144	10.0	*Sin*	20	–	$0.0^\star$, 1.0, 2.0, 4.0, 8.0, $12.0^\star$
2	100	10.0	*Sin*	20	–	$0.0^\star$, 2.0, $4.0^\star$, 8.0, $12.0^\star$
3	65	10.0	*Sin*	20	–	$0.0^\star$, 0.4, 1.0, $2.0^\star$, 8.0
4	65	10.0	*Sin*	36	–	$0.0^\star$, 0.8, 1.8, 3.6, 14.4
5	144	10.0	*Sin*	36	–	$0.0^\star$, 1.8, 3.6, 7.2, 14.4
6	144	17.0	*Sin*	20	–	0.0, $4.0^\star$, 8.0
7	100	10.0	*Sin*	15	–	$0.0^\star$, 1.5, 2.9, 5.8

Table A.4.: Systems for which the linear stability of a gravity-driven film flow over topography was investigated at different corrugation amplitudes A. Data taken from [76, 107, 108, 110, 112, 113, 122]. New experiments [114] are marked by a star ($\star$). The numbers on the left-hand side correspond to the numbers in the Figures 4.21 and A.7. Modified and reprinted with permission from [114].

A.4.2. All available stability charts for variation of A

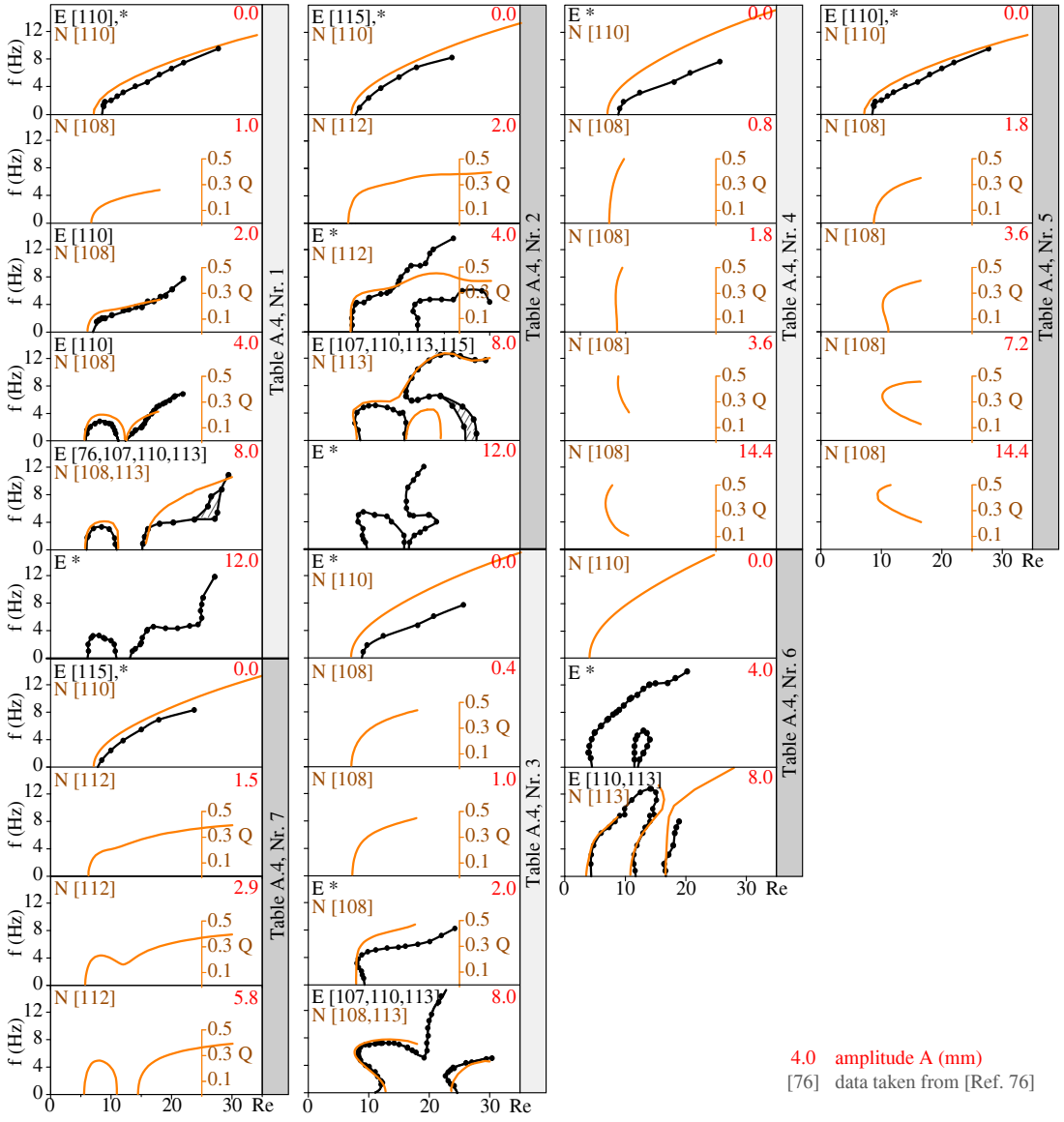

Figure A.7.: Linear stability at different corrugation amplitudes A. The charts include experiments (E) and numerics (N) taken from [76, 107, 108, 110, 112, 113, 122] and new experiments ($\star$) from [114]. Hatched markings denote measurement uncertainties. Computed neutral curves are shown as $Q(Re)$ if no relation between Q and f was published. Modified and reprinted with permission from [114]. © AIP Publishing.

A.4.3. Pathway of the stability for variation of A

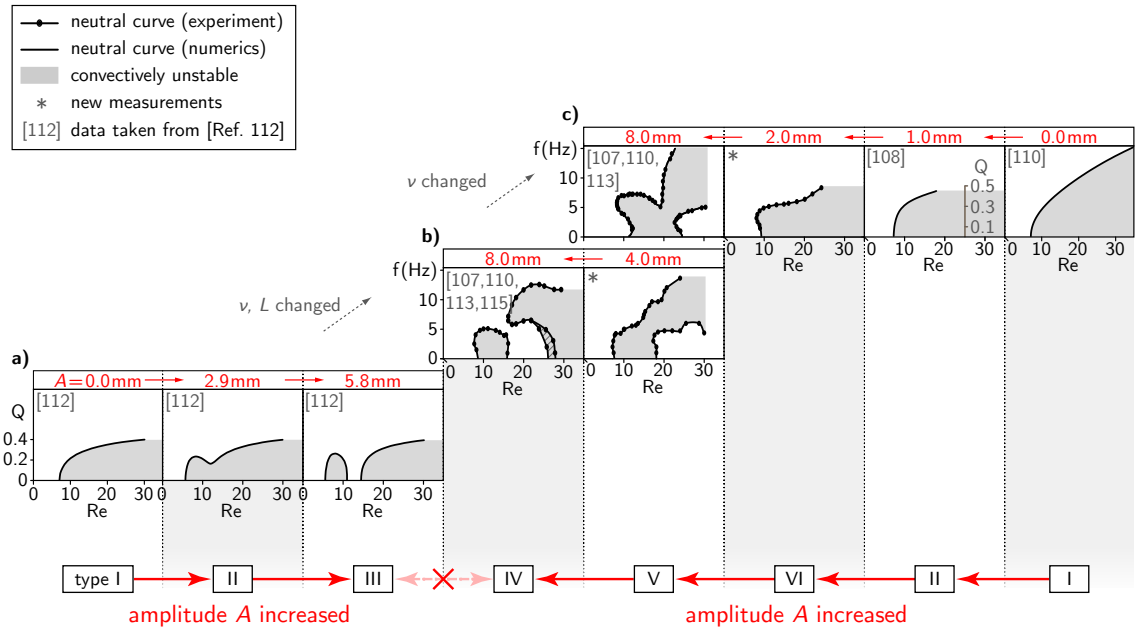

Figure A.8.: Evolution of the stability chart with the amplitude A of the corrugation increasing in the direction of the red arrows inside each of the figures (a) - (c), while all other parameters *shape*, α, ν, L, W of the system were retained. The measured stability charts were assigned to the schematic chart patterns I - VI defined in Figure 4.20. The red arrows symbolize the transitions between different patterns of stability charts which occurred when A was increased. No example for a transition between pattern III and IV was found (red cross). The given examples correspond to *Sin*, $\alpha = 10.0\,^{\circ}$ and (a) $\nu = 100\,\mathrm{mm}^2/\mathrm{s}$, $L = 15\,\mathrm{mm}$, (b) $\nu = 100\,\mathrm{mm}^2/\mathrm{s}$, $L = 20\,\mathrm{mm}$ and (c) $\nu = 65\,\mathrm{mm}^2/\mathrm{s}$, $L = 20\,\mathrm{mm}$. Hatched markings denote measurement uncertainties. Computed neutral curves are shown as $Q(Re)$ if no relation between Q and f was published. Modified and reprinted with permission from [114]. © AIP Publishing.

A.5. Variation of the tip width W of the topography

A.5.1. Table of all available systems for variation of W

Nr.	$\nu(\mathrm{mm}^2/\mathrm{s})$	$\alpha(\mathrm{deg})$	*shape*	$A(\mathrm{mm})$	$L(\mathrm{mm})$	$W(\mathrm{mm})$
1	144	10.0	*Rec*	8	20	$1^{\star}$, $10^{\star}$, $20^{\star}$
2	100	10.0	*Rec*	8	20	1, 6, $10^{\star}$, $20^{\star}$
3	100	10.0	*Rec*	8	40	$1^{\star}$, $20^{\star}$, $30^{\star}$, $40^{\star}$
4	100	10.0	*Rec*	8	30	$1^{\star}$, $10^{\star}$, $30^{\star}$
5	144	10.0	*Rec*	8	30	$1^{\star}$, $10^{\star}$, $30^{\star}$

Table A.5.: Systems for which the linear stability of a gravity-driven film flow over topography was investigated at different tip widths W of the rectangular corrugations. Data taken from [76, 110, 113, 122]. New experiments [114] are marked by a star ($\star$). The numbers on the left-hand side correspond to the numbers in the Figures 4.21 and A.9. Modified and reprinted with permission from [114].

A.5.2. All available stability charts for variation of W

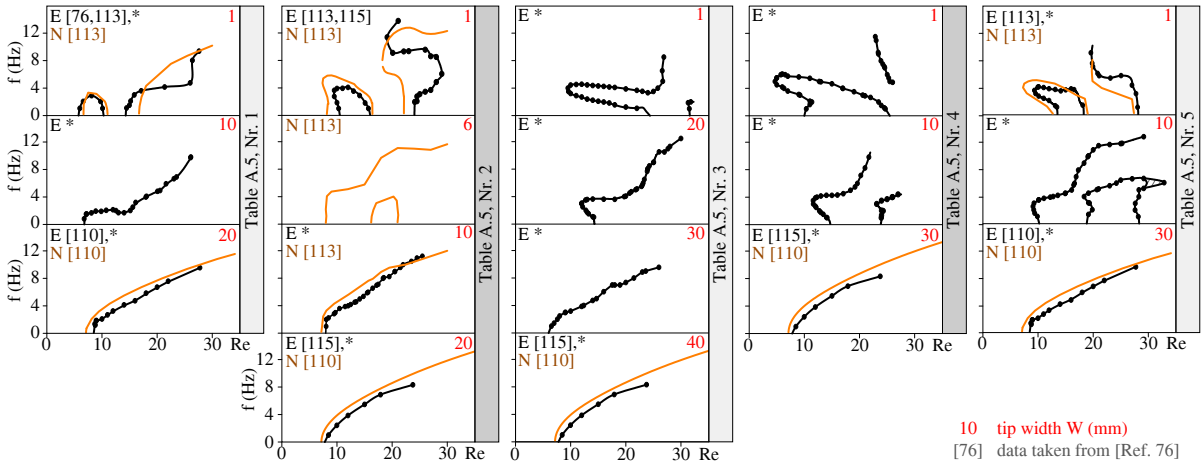

Figure A.9.: Linear stability at different tip widths W of the corrugation. The charts include experiments (E) and numerics (N) taken from [76, 110, 113, 122] and new experiments ($\star$) from [114]. Hatched markings denote measurement uncertainties. Modified and reprinted with permission from [114]. © AIP Publishing.

A.5.3. Pathway of the stability for variation of W

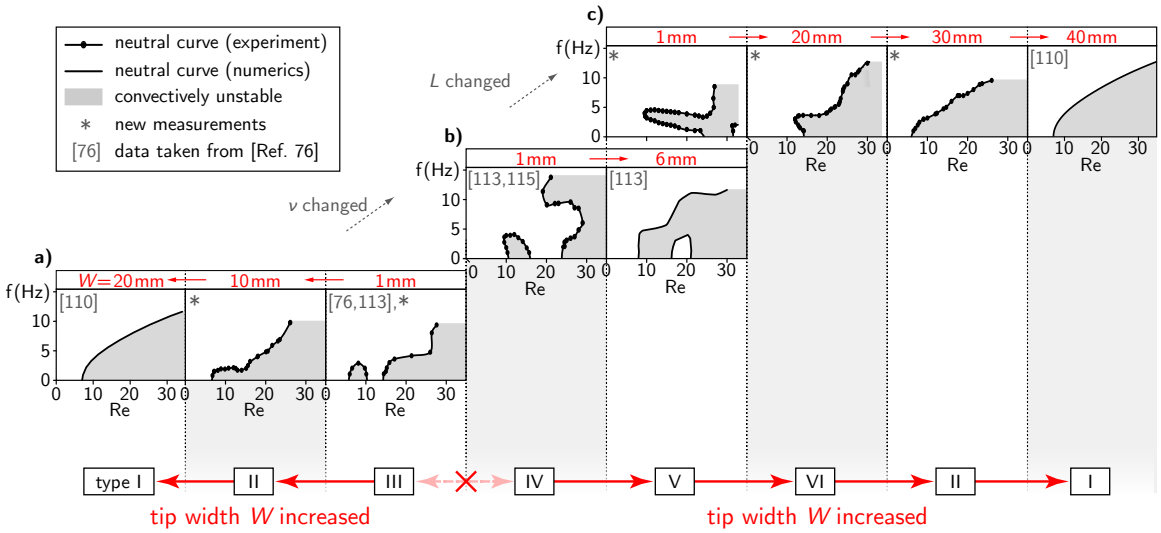

Figure A.10.: Evolution of the stability chart with the tip width W of the rectangular corrugation increasing in the direction of the red arrows inside each of the figures (a) - (c), while all other parameters *shape*, α, ν, L, A of the system were retained. The measured stability charts were assigned to the schematic chart patterns I - VI defined in Figure 4.20. The red arrows symbolize the transitions between different patterns of stability charts which occurred when W was increased. No example for a transition between pattern III and IV was found (red cross). The given examples correspond to Rec, $A = 8\,\mathrm{mm}$, $\alpha = 10.0\,^\circ$ and (a) $\nu = 144\,\mathrm{mm}^2/\mathrm{s}$, $L = 20\,\mathrm{mm}$, (b) $\nu = 100\,\mathrm{mm}^2/\mathrm{s}$, $L = 20\,\mathrm{mm}$, (c) $\nu = 100\,\mathrm{mm}^2/\mathrm{s}$, $L = 40\,\mathrm{mm}$. Modified and reprinted with permission from [114]. © AIP Publishing.

A.6. Variation of the specific *shape* of the topography

A.6.1. Table of all available systems for variation of *shape*

Nr.	$\nu(\mathrm{mm}^2/\mathrm{s})$	$\alpha(\mathrm{deg})$	$A(\mathrm{mm})$	$L(\mathrm{mm})$	$W(\mathrm{mm})$	*shape*
1	144	10.0	8	20	1	Sin, $SinMod^{\star}_{13}$, $Saw^{\star}$, $SawRev^{\star}$, $Rec^{\star}$
2	100	10.0	8	20	1	Sin, $SinMod^{\star}_{19}$, $Saw^{\star}$, Rec
3	144	10.0	8	30	1	Sin, $Rec^{\star}$
4	144	10.0	8	40	1	Sin, $Rec^{\star}$

Table A.6.: Systems for which the linear stability of a gravity-driven film flow over topography was investigated at different specific shapes *shape* of the corrugations. Data taken from [76,107,108,110,113,122]. New experiments [114] are marked by a star ($\star$). The numbers on the left-hand side correspond to the numbers in Figure A.11. The modified sinusoidal geometry *SinMod* is the sinusoidal geometry *Sin*, modified by replacing the eddies, which appear in the troughs at the specific Reynolds number $Re = 13$ or $Re = 19$, by a solid contour [76, 107]. Modified and reprinted with permission from [114].

A.6.2. All available stability charts for variation of *shape*

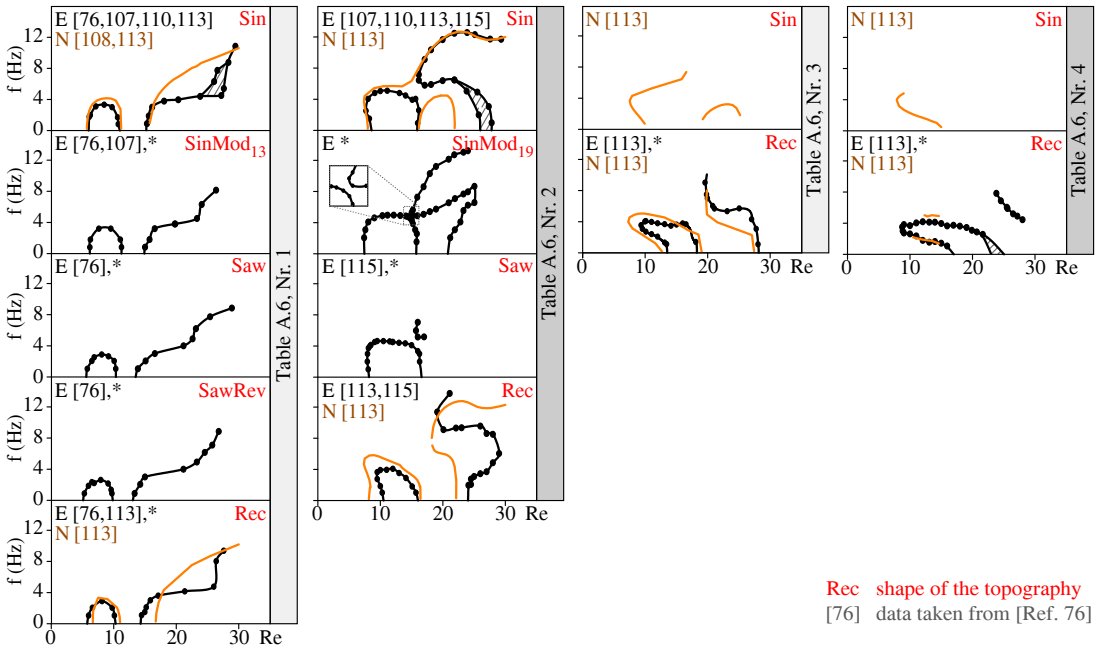

Figure A.11.: Linear stability for different specific shapes *shape* of the corrugation. The charts include experiments (E) and numerics (N) taken from [76, 107, 108, 110, 113, 122] and new experiments ($\star$) from [114]. Hatched markings denote measurement uncertainties. Modified and reprinted with permission from [114]. © AIP Publishing.

List of Symbols

symbol (unit)	description	page list
α (°)	Inclination angle of the channel	46–48, 50–53, 56–60, 62–72, 74–84, 87–91, 97, 98, 100, 102, 104–106, 112
β (°)	Inclination angle of the lasers used for the stability measurements	54
η (Pas)	Dynamic viscosity	45, 47
λ (m)	Wavelength of the traveling free surface wave	54, 56
ν (m^2s^{-1})	Kinematic viscosity	45, 46, 48, 62–67, 72, 74–79, 82, 84, 97–100, 102, 104–106, 112
ρ (kgm^{-3})	Liquid density	45–47, 90
ρ_p (kgm^{-3})	Particle density	47
σ (Nm^{-1})	Surface tension	45, 46, 90
θ (°C)	Temperature	45, 46, 114
ξ	Topography steepness	79
ξ_d	Grade of dispersity	47
A (m)	Topography amplitude	47, 50–53, 56, 58, 62–84, 87–91, 97, 98, 100, 102–106, 112
a (m)	Amplitude of the traveling free surface wave	54–56, 66, 80–84, 87
a_1 (m)	First free surface harmonic amplitude	51, 69–72
a_2 (m)	Second free surface harmonic amplitude	51, 69–72
A_e (m)	Paddle amplitude; excitation amplitude	54, 82–84
b (m^{-1})	Exponential growth rate of linear waves	55, 56, 64, 66, 76, 98, 100
B_1 (a.u.)	Amplitude of the Gaussian fit of the main peak of $\hat{p}_1(f')$	55
B_2 (a.u.)	Amplitude of the Gaussian fit of the main peak of $\hat{p}_2(f')$	55
b_c (m)	Channel width; substrate width	46, 48
B_i (a.u.)	Amplitude of the Gaussian fit of the main peak of $\hat{p}_i(f')$	55
ΔB (a.u.)	Measure for the difference of the free surface amplitudes of the traveling waves at the positions x_1 and x_2	55, 56

symbol (unit)	description	page list
Δb (m^{-1})	Step width of the exponential growth rate of linear waves	76, 98, 100
D	Deviation from the maximum value of the cross-correlation function K	60
d_1 (m)	Inflow distance	56
d_2 (m)	Outflow distance	56
d_L (m)	Distance between the lasers 1 and 2 in the stability measurements	56
d_p (m)	Particle diameter	47
$d_{V,16}$ (m)	Particle size, which is greater than or equal to 16% of all particles	47
$d_{V,50}$ (m)	Median particle size	47
$d_{V,84}$ (m)	Particle size, which is greater than or equal to 84% of all particles	47
$d_{V,j}$ (m)	Particle size, which is greater than or equal to j% of all particles	47
$\vec{e}_x$	Unity vector in x-direction	48, 69
f (s^{-1})	Paddle frequency; excitation frequency	54–56, 59, 62–64, 66, 71, 75, 80–84, 97, 99, 103, 104
f' (s^{-1})	Frequency	55
f_0 (m)	Lower boundary of the steady-state flowing domain	52, 59–61
$Flat$	Flat topography shape	47, 74, 76, 97, 98
g (ms^{-2})	Gravitational acceleration	45, 47, 48, 90
h (m)	Time-dependent local film thickness	51
h_0 (m)	Local film thickness of the steady-state flow; upper boundary of the steady-state flowing domain	49–51, 53, 59–61, 68, 69, 71
h_{av} (m)	Mean film thickness	51, 69–72, 89, 90
H_{in} (m)	Inflow height	89, 90
h_n (m)	Nusselt film thickness	48, 69, 71, 79
H_{out} (m)	Outflow height	89, 90
K	Cross-correlation function	59, 60
Ka	Kapitza number	45, 46, 56, 57
κ	Ratio of the travelling wave's free surface amplitude to its wavelength	56
L (m)	Topography wavelength	47, 50–53, 56, 58, 59, 61–72, 74–84, 87–91, 97, 98, 100–102, 104–106, 112
n	Power-law index	79
$\mathbf{p}_i$ (m)	Position of the laser spot i	55
$\hat{\mathbf{p}}_i$ (m)	Fourier transformed laser spot position of the laser i	55
$\hat{p}_i$ (m)	Absolute value of the Fourier transformed laser spot position of the laser i	55

symbol (unit)	description	page list
$p_{x',i}$ (m)	The x'-position of the spot of laser i on the screen	55
$\hat{p}_{x',i}$ (m)	Fourier transformed x'-position of the spot of laser i	55
$p_{z',i}$ (m)	The z'-position of the spot of laser i on the screen	55
$\hat{p}_{z',i}$ (m)	Fourier transformed z'-position of the spot of laser i	55
Q	Floquet parameter	75, 81, 97, 99, 103, 104
$\dot{q}$ (m^2s^{-1})	Two-dimensional flow rate	48
Re	Reynolds number	48, 50–52, 55–60, 62–72, 75, 80, 81, 87–91, 97, 99, 103, 104, 106
Re_c	Critical Reynolds number	58, 63, 65, 78
Rec	Rectangular topography shape	47, 56, 58, 67, 74, 76, 92, 98, 100, 102, 104–106
S_1	Specific sinusoidal topography	58–61
S_2	Modified S_1 topography	58
S_3	Specific rectangular topography	58, 59
S_4	Specific sawtooth-like topography	58
S_5	Reversely mounted S_4 topography	58–61
S_i	Topography shape as specified by the index i	59, 60
Saw	Sawtooth-like topography shape	47, 58, 74, 90, 91, 98, 106
$SawRev$	Reverse sawtooth-like topography shape	47, 58, 74, 90, 91, 106
$shape$	Specific shape of the topography	47, 58, 62–64, 74–78, 97, 98, 100, 102, 104–106, 112
Sin	Sinusoidal topography shape	47, 50–52, 58, 64–66, 74, 76, 80, 87, 88, 91, 97, 98, 100, 102, 104, 106
$SinMod$	Modified sinusoidal topography shape	47, 58, 74, 106
t (s)	Time	51, 55
u (ms^{-1})	Absolute value of the local flow velocity	52, 53, 68, 69
u_s (ms^{-1})	Local free surface velocity	49, 53, 69, 70
$\bar{u}_s$ (ms^{-1})	Mean free surface velocity	53, 70, 71
∇u_s (s^{-1})	Free surface velocity gradient	70, 71
$\vec{u}$ (ms^{-1})	Velocity vector	48, 52, 53, 68, 69
u_x (ms^{-1})	The x-component of the velocity vector	69
u_z (ms^{-1})	The z-component of the velocity vector	69
$u_{s,max}$ (ms^{-1})	Maximum value of the free surface velocity	70
$u_{s,min}$ (ms^{-1})	Minimum value of the free surface velocity	70

symbol (unit)	description	page list
$u_{s,n}$ (ms^{-1})	Nusselt free surface velocity	48, 70
$\dot{V}$ ($\mathrm{m}^3\mathrm{s}^{-1}$)	Three-dimensional volume flux	46, 48, 54
W (m)	Topography tip width	47, 53, 56, 58, 61–63, 66, 67, 71–79, 82–84, 91, 92, 97, 98, 100, 102, 104–106, 112
w_{sed} (ms^{-1})	Sedimentation speed	47
x (m)	The x-coordinate	46, 47, 49–53, 59–61, 68–71, 89, 90
x' (m)	The x'-coordinate of the reference frame of the screen	55, 56
x_1 (m)	x-position of laser 1	54, 55
x_2 (m)	x-position of laser 2	54, 55
x_i (m)	x-position of laser i	54, 55
y (m)	The y-coordinate; distance to the channel's centerplane	46, 48–54, 86–91
z (m)	The z-coordinate	48–54, 68, 69, 89
z' (m)	The z'-coordinate of the reference frame of the screen	55, 56

To acknowledge the original works reviewed in Chapter 1, the author sticks to their individual nomenclatures, there. The present "List of Symbols" covers all other parts of the present thesis.

List of Figures

List of Tables

References

[1] de Gennes, P.-G., Brochard-Wyart, F., Quere, D.: Capillarity and Wetting Phenomena (Springer, Berlin, 2004).

[2] Braun, R. J.: Dynamics of the tear film. Annu. Rev. Fluid Mech. **44**, 267–297 (2011).

[3] Luca, I., Hutter, K., Tai, Y. C., Kuo, C. Y.: A hierarchy of avalanche models on arbitrary topography. Acta Mech. **205**, 121–149 (2009).

[4] Greve, R., Blatter, H.: Dynamics of Ice Sheets and Glaciers (Springer, Berlin, 2009).

[5] Kumar, A., Karig, D., Acharya, R., Neethirajan, S., Mukherjee, P. P., Retterer, S., Doktycz, M. J.: Microscale confinement features can affect biofilm formation. Microfluid. Nanofluid. **14**, 895–902 (2013).

[6] Webb, R. L.: Principles of Enhanced Heat Transfer (Wiley, New York, 1994).

[7] Kistler, S. F., Schweizer, P. M.: Liquid Film Coating (Springer, Netherlands, 1997).

[8] Weinstein, S. J., Ruschak, K. J.: Coating flows. Annu. Rev. Fluid Mech. **36**, 29–53 (2004).

[9] Gugler, G., Beer, R., Mauron, M.: Operative limits of curtain coating due to edges. Chem. Eng. Process. Process. Intensif. **50**, 462 – 465 (2011).

[10] Oron, A., Davis, S. H., Bankoff, S. G.: Long-scale evolution of thin liquid films. Rev. Mod. Phys. **69**, 931–980 (1997).

[11] Chang, H. C., Demekhin, E. A.: Complex Wave Dynamics on Thin Films (Elsevier, Amsterdam, 2002).

[12] Craster, R. V., Matar, O. K.: Dynamics and stability of thin liquid films. Rev. Mod. Phys. **81**, 1131–1198 (2009).

[13] Nusselt, W.: Die Oberflächenkondensation des Wasserdampfes. VDI Z. (1857-1968) **60**, 541–546 (1916).

[14] Aksel, N., Schörner, M.: Films over topography: from creeping flow to linear stability, theory, and experiments, a review. Acta Mech. **229**, 1453–1482 (2018).

[15] Spurk, J.-H., Aksel, N.: Fluid Mechanics, 2.ed. (Springer, Berlin, 2008).

[16] Kalliadasis, S., C. Bielarz, Homsy, G. M.: Steady free-surface thin film flows over topography. Phys. Fluids **12**, 1889 – 1898 (2000).

[17] Kalliadasis, S., C. Bielarz, Homsy, G. M.: Erratum: "Steady free-surface thin film flows over topography" [Phys. Fluids 12, 1889 (2000)]. Phys. Fluids **12**, 3305 (2000).

[18] Mazouchi, A., Homsy, G. M.: Free surface Stokes flow over topography. Phys. Fluids **13**, 2751–2761 (2001).

[19] Aksel, N.: Influence of the capillarity on a creeping film flow down an inclined plane with an edge. Arch. Appl. Mech. **70**, 81–90 (2000).

[20] Heining, C., Sellier, M., Aksel, N.: The inverse problem in creeping film flows. Acta Mech. **223**, 841–847 (2012).

[21] Gaskell, P. H., Jimack, P. K., Sellier, M., Thompson, H. M., Wilson, M. C. T.: Gravity-driven flow of continuous thin liquid films on non-porous substrates with topography. J. Fluid Mech. **509**, 253 – 280 (2004).

[22] Wang, C. Y.: Liquid film flowing slowly down a wavy incline. AIChE J. **27**, 207 – 212 (1981).

[23] Scholle, M., Wierschem, A., Aksel, N.: Creeping films with vortices over strongly undulated bottoms. Acta Mech. **168**, 167–193 (2004).

[24] Scholle, M., Rund, A., Aksel, N.: Drag reduction and improvement of material transport in creeping films. Acta Mech. **75**, 93–112 (2006).

[25] Pozrikidis, C.: The flow of a liquid film along a periodic wall. J. Fluid Mech. **188**, 275–300 (1988).

[26] Wierschem, A., Scholle, M., Aksel, N.: Vortices in film flow over strongly undulated bottom profiles at low Reynolds numbers. Phys. Fluids **15**, 426–435 (2003).

[27] Nguyen, P. K., Bontozoglou, V.: Steady solutions of inertial film flow along strongly undulated substrates. Phys. Fluids **23**, 052103 (2011).

[28] Moffatt, H. K.: Viscous and resistive eddies near a sharp corner. J. Fluid Mech. **18**, 1 – 18 (1964).

[29] Pozrikidis, C., Thoroddsen, S. T.: The deformation of a liquid film flowing down an inclined plane wall over a small particle arrested on the wall. Phys. Fluids A **3**, 2546–2558 (1991).

[30] Hayes, M., O'Brien, S. B. G., Lammers, J. H.: Green's function for steady flow over a small two-dimensional topography. Phys. Fluids **12**, 2845–2858 (2000).

[31] Blyth, M. G., Pozrikidis, C.: Film flow down an inclined plane over a three-dimensional obstacle. Phys. Fluids **18**, 052104 (2006).

[32] Baxter, S. J., Power, H., Cliffe, K. A., Hibberd, S.: Three-dimensional thin film flow over and around an obstacle on an inclined plane. Phys. Fluids **21**, 032102 (2009).

[33] Lee, Y. C., Thompson, H. M., Gaskell, P. H., An efficient adaptive multigrid algorithm for predicting thin film flow on surfaces containing localised topographic features. Comput. Fluids **36**, 838 – 855 (2007).

[34] Sellier, M., Lee, Y.C., Thompson, H. M., Gaskell, P. H.: Thin film flow on surfaces containing arbitrary occlusions. Comput. Fluids **38**, 171 – 182 (2009).

[35] Lee, Y. C., Thompson, H. M., Gaskell, P. H.: Three-dimensional thin film and droplet flows over and past surface features with complex physics. Comput. Fluids **46**, 306 – 311 (2011).

[36] Lee, Y. C., Thompson, H. M., Gaskell, P. H.: Dynamics of thin film flow on flexible substrate. Chem. Eng. Process. Process. Intensif. **50**, 525 – 530 (2011).

[37] Luo, H., Pozrikidis, C.: Gravity-driven film flow down an inclined wall with three-dimensional corrugations. Acta Mech. **188**, 209–225 (2007).

[38] Bontozoglou, V., Serifi, K.: Falling film flow along steep two-dimensional topography: The effect of inertia. Int. J. Multiph. Flow **34**, 734–747 (2008).

[39] Wierschem, A., Scholle, M., Aksel, N.: Comparison of different theoretical approaches to experiments on film flow down an inclined wavy channel. Exp. Fluids **33**, 429 – 442 (2002).

[40] Wierschem, A., Aksel, N.: Influence of inertia on eddies created in films creeping over strongly undulated substrates. Phys. Fluids **16**, 4566–4574 (2004).

[41] Scholle, M., Haas, A., Aksel, N., Wilson, M. C. T., Thompson, H. M., Gaskell, P. H.: Competing geometric and inertial effects on local flow structure in thick gravity-driven fluid films. Phys. Fluids **20**, 123101 (2008).

[42] Bontozoglou, V., Kalliadasis, S., Karabelas, A. J.: Inviscid free-surface flow over a periodic wall. J. Fluid Mech. **226**, 189 – 203 (1991).

[43] Bontozoglou, V., Papapolymerou, G.: Laminar film flow down a wavy incline. Int. J. Multiph. Flow **23**, 69 – 79 (1997).

[44] Trifonov, Y. Y.: Viscous liquid film flows over a periodic surface. Int. J. Multiph. Flow **24**, 1139–1161 (1998).

[45] Bontozoglou, V.: Laminar film flow along a periodic wall. CMES-Comp. Model Eng. **1**, 133 – 142 (2000).

[46] Wierschem, A., Aksel, N.: Hydraulic jumps and standing waves in gravity-driven flows of viscous liquids in wavy open channels. Phys. Fluids **16**, 3868–3877 (2004).

[47] Wierschem, A., Bontozoglou, V., Heining, C., Uecker, H., Aksel, N.: Linear resonance in viscous films on inclined wavy planes. Int. J. Multiph. Flow **34**, 580–589 (2008).

[48] Anshus, B. E., Goren, S. L.: A method of getting approximate solutions to the Orr-Sommerfeld equation for flow on a vertical wall. AICHE J. **12**, 1004–1008 (1966).

[49] Heining, C., Bontozoglou, V., Aksel, N., Wierschem, A.: Nonlinear resonance in viscous films on inclined wavy planes. Int. J. Multiph. Flow **35**, 78 – 90 (2009).

[50] Duffing, G.: Erzwungene Schwingungen bei Veränderlicher Eigenfrequenz (F. Vieweg und Sohn, Braunschweig, 1918).

[51] Malamataris, N. A., Bontozoglou, V.: Computer aided analysis of viscous film flow along an inclined wavy wall. J. Comput. Phys. **154**, 372 – 392 (1999).

[52] Pak, M. I., Hu, G. H.: Numerical investigations on vortical structures of viscous film flows along periodic rectangular corrugations. Int. J. Multiph. Flow **37**, 369 – 379 (2011).

[53] Vlachogiannis, M., Bontozoglou, V.: Experiments on laminar film flow along a periodic wall. J. Fluid Mech. **457**, 133–156 (2002).

[54] Argyriadi, K., Vlachogiannis, M., Bontozoglou, V.: Experimental study of inclined film flow along periodic corrugations: the effect of wall steepness. Phys. Fluids **18**, 012102 (2006).

[55] Wierschem, A., Pollak, T., Heining, C., Aksel, N.: Suppression of eddies in films over topography. Phys. Fluids **22**, 113603 (2010).

[56] Valluri, P., Matar, O. K., Hewitt, G. F., Mendes, M. A.: Thin film flow over structured packings at moderate Reynolds numbers. Chem. Eng. Sci. **60**, 1965 – 1975 (2005).

[57] Varchanis, S., Dimakopoulos, Y., Tsamopoulos, J.: Steady film flow over a substrate with rectangular trenches forming air inclusions. Phys. Rev. Fluids **2**, 124001 (2017).

[58] Decré, M. M. J., Baret, J.-C.: Gravity-driven flows of viscous liquids over two-dimensional topographies. J. Fluid Mech. **487**, 147–166 (2003).

[59] Veremieiev, S., Thompson, H. M. Gaskell, P. H.: Inertial thin film flow on planar surfaces featuring topography. Comput. Fluids **39**, 431 – 450 (2010).

[60] Veremieiev, S., Thompson, H. M., Gaskell, P. H.: Free-surface film flow over topography: full three-dimensional finite element solutions. Comput. Fluids **122**, 66 –82 (2015).

[61] Wang, C. Y.: Low Reynolds number film flow down a three-dimensional bumpy surface. J. Fluids Eng. **127**, 1122 – 1127 (2005).

[62] Luo, H., Pozrikidis, C.: Effect of inertia on film flow over oblique and three-dimensional corrugations. Phys. Fluids **18**, 078107 (2006).

[63] Luo, H., Pozrikidis, C.: Publisher's note: "Effect of inertia on film flow over oblique and three-dimensional corrugations" [Phys. Fluids 18, 078107 (2006)]. Phys. Fluids **18**, 129901 (2006).

[64] Heining, C., Pollak, T., Aksel, N.: Pattern formation and mixing in three-dimensional film flow. Phys. Fluids **24**, 042102 (2012).

[65] Scholle, M., Aksel, N.: An exact solution of visco-capillary flow in an inclined channel. Zeitschrift für Angewandte Mathematik und Physik ZAMP **52**, 749–769 (2001).

[66] Scholle, M. Aksel, N.: Thin film limit and film rupture of the visco-capillary gravity-driven channel flow. Zeitschrift für Angewandte Mathematik und Physik ZAMP **54**, 517–531 (2003).

[67] Haas, A., Pollak, T., Aksel, N.: Side wall effects in thin gravity-driven film flow: steady and draining flow. Phys. Fluids **23**, 062107 (2011).

[68] Sellier, M.: Inverse problems in free surface flows: a review. Acta Mech. **227**, 913–935 (2016).

[69] Sellier, M.: Substrate design or reconstruction from free surface data for thin film flows. Phys. Fluids **20**, 062106 (2008).

[70] Heining, C., Aksel, N.: Bottom reconstruction in thin-film flow over topography: steady solution and linear stability. Phys. Fluids **21**, 083605 (2009).

[71] Heining, C.: Velocity field reconstruction in gravity-driven flow over unknown topography. Phys. Fluids **23**, 032101 (2011).

[72] Heining, C., Pollak, T., Sellier, M.: Flow domain identification from free surface velocity in thin inertial films. J. Fluid Mech. **720**, 338–356 (2013).

[73] Anjalaiah, Y., Chakraborty, S., Usha, R.: Steady solution of an inverse problem in gravity-driven shear-thinning film flow: reconstruction of an uneven bottom substrate. J. Non-Newton Fluid Mech. **219**, 65–77 (2015).

[74] Usha, R., Anjalaiah: Steady solution and spatial stability of gravity-driven thin-film flow: reconstruction of an uneven slippery bottom substrate. Acta Mech. **227**, 1685–1709 (2016).

[75] Heining, C., Sellier, M.: Flow domain identification in three-dimensional creeping flows. Phys. Fluids. **29**, 012107 (2017).

[76] Schörner, M., Reck, D., Aksel, N.: Does the topography's specific shape matter in general for the stability of film flows? Phys. Fluids **27**, 042103 (2015).

[77] Kapitza, P. L: Wavy flow of thin layers of a viscous fluid. Zh. Eksp. Teor. Fiz. **18**, 3–28 (1948).

[78] Kapitza, P. L., Kapitza, S. P.: Wavy flow of thin layers of a viscous fluid. Zh. Eksp. Teor. Fiz. **19**, 105-120 (1949).

[79] Benjamin, T. B.: Wave formation in laminar flow down an inclined plane. J. Fluid Mech. **2**, 554–574 (1957).

[80] Yih, C. S.: Stability of liquid flow down an inclined plane. Phys. Fluids **6**, 321–334 (1963).

[81] Orr, W. M'F.: The stability or instability of the steady motions of a perfect liquid and of a viscous liquid. Part I: A perfect liquid. Proc. R. Ir. Acad. A Math. Phys. Sci. **27**, 9–68 (1907).

[82] Orr, W. M'F.: The stability or instability of the steady motions of a perfect liquid and of a viscous liquid. Part II: A viscous liquid. Proc. R. Ir. Acad. A Math. Phys. Sci. **27**, 69–138 (1907).

[83] Sommerfeld, A.: Ein Beitrag zur hydrodynamischen Erklärung der turbulenten Flüssigkeitsbewegungen. In: Proceedings of the 4th International Congress of Mathematicians **3**, 116–124 (1908).

[84] Lin, S. P.: Finite-amplitude stability of a parallel flow with a free surface. J. Fluid Mech. **36**, 113–126 (1969).

[85] Gjevik, B.: Occurrence of finite-amplitude surface waves on falling liquid films. Phys. Fluids **13**, 1918–1925 (1970).

[86] Benney, D. J.: Long waves on liquid films. J. Math. Phys. (Cambridge, Mass.) **45**, 150 (1966).

[87] Liu, J., Paul, J. D., Gollub, J. P.: Measurements of the primary instabilities of film flows. J. Fluid Mech. **250**, 69 – 101 (1993).

[88] Liu, J., Gollub, J. P.: Solitary wave dynamics of film flows. Phys. Fluids **6**, 1702–1712 (1994).

[89] Liu, J., Gollub, J. P.: Onset of spatially chaotic waves on flowing films. Phys. Rev. Lett. **70**, 2289–2292 (1993).

[90] Liu, J., Schneider, J. B., Gollub, J. P.: Three-dimensional instabilities of film flows. Phys. Fluids **7**, 55 – 67 (1995).

[91] Trifonov, Y. Y.: Stability of the wavy film falling down a vertical plate: the DNS computations and Floquet theory. Int. J. Multiph. Flow **61**, 73–82 (2014).

[92] Kalliadasis, S., Homsy, G. M.: Stability of free-surface thin-film flows over topography. J. Fluid Mech. **448**, 387–410 (2001).

[93] Bielarz, C., Kalliadasis, S.: Time-dependent free-surface thin film flows over topography. Phys. Fluids **15**, 2512–2524 (2003).

[94] Dávalos-Orozco, L. A.: Instabilities of thin films flowing down flat and smoothly deformed walls. Microgravity Sci. Technol. **20**, 225–229 (2008).

[95] Dávalos-Orozco, L. A.: Nonlinear instability of a thin film flowing down a smoothly deformed surface. Phys. Fluids **19**, 074103 (2007).

[96] Wierschem, A., Aksel, N.: Instability of a liquid film flowing down an inclined wavy plane. Physica D **186**, 221–237 (2003).

[97] Wierschem, A., Lepski, C., Aksel, N.: Effect of long undulated bottoms on thin gravity-driven films. Acta Mech. **179**, 41–66 (2005).

[98] Trifonov, Y. Y.: Stability and nonlinear wavy regimes in downward film flows on a corrugated surface. J. App. Mech. Tech. Phys. **48**, 91–100 (2007).

[99] Trifonov, Y. Y.: Stability of a viscous liquid film flowing down a periodic surface. Int. J. Multiph. Flow **33**, 1186–1204 (2007).

[100] Heining, C., Aksel, N.: Effects of inertia and surface tension on a power-law fluid flowing down a wavy incline. Int. J. Multiphase Flow **36**, 847–857 (2010).

[101] D'Alessio, S. J. D., Pascal, J. P., Jasmine, H. A.: Instability in gravity-driven flow over uneven surfaces. Phys. Fluids **21**, 062105 (2009).

[102] Jordan, D. W., Smith, P.: Nonlinear Ordinary Differential Equations, 2nd ed. (Oxford University Press, Oxford, 1987).

[103] Ruyer-Quil, C., Manneville, P.: Improved modeling of flows down inclined planes. Eur. Phys. J. B **15**, 357 (2000).

[104] Balmforth, N. J., Mandre S.: Dynamics of roll waves. J. Fluid Mech. **514**, 1–33 (2004).

[105] Kármán, Th. v.: Über laminare und turbulente Reibung. ZAMM **1**, 233–252 (1921).

[106] Pohlhausen, K.: Zur näherungsweisen Integration der Differentialgleichung der laminaren Reibungsschicht. ZAMM **1**, 252–268 (1921).

[107] Pollak, T., Aksel, N.: Crucial flow stabilization and multiple instability branches of gravity-driven films over topography. Phys. Fluids **25**, 024103 (2013).

[108] Trifonov, Y. Y.: Stability of a film flowing down an inclined corrugated plate: the direct Navier-Stokes computations and Floquet theory. Phys. Fluids **26**, 114101 (2014).

[109] Cao, Z., Vlachogiannis, M., Bontozoglou, V.: Experimental evidence for a short-wave global mode in film flow along periodic corrugations. J. Fluid Mech. **718**, 304–320 (2013).

[110] Schörner, M., Reck, D., Aksel, N.: Stability phenomena far beyond the Nusselt flow – Revealed by experimental asymptotics. Phys. Fluids **28**, 022102 (2016).

[111] Trifonov, Y. Y.: Viscous liquid film flow down an inclined corrugated surface. Calculation of the flow stability to arbitrary perturbations using an integral method. J. Appl. Mech. Tech. Phys. **57**, 195 – 201 (2016).

[112] Trifonov, Y. Y.: Nonlinear waves on a liquid film falling down an inclined corrugated surface. Phys. Fluids **29**, 054104 (2017).

[113] Schörner, M., Reck, D. Aksel, N., Trifonov, Y. Y.: Switching between different types of stability isles in films over topographies. Acta Mech. **229**, 423–436 (2018).

[114] Schörner, M., Aksel, N.: The stability cycle: a universal pathway for the stability of films over topography. Phys. Fluids **30**, 012105 (2018).

[115] Vlachogiannis, M., Samandas, A., Leontidis, V., Bontozoglou, V.: Effect of channel width on the primary instability of inclined film flow. Phys. Fluids **22**, 012106 (2010).

[116] Leontidis, V., Vatteville, J., Vlachogiannis, M., Andritsos, N., Bontozoglou, V.: Nominally two-dimensional waves in inclined film flow in channels of finite width. Phys. Fluids **22**, 112106 (2010).

[117] Georgantaki, A., Vatteville, J., Vlachogiannis, M., Bontozoglou, V.: Measurements of liquid film flow as a function of fluid properties and channel width: evidence for surface-tension-induced long-range transverse coherence. Phys. Rev. E **84**, 026325 (2011).

[118] Pollak, T., Haas, A., Aksel, N.: Sidewall effects on the instability of thin gravity-driven films: from long-wave to short-wave instability. Phys. Fluids **23**, 094110 (2011).

[119] Guzanov, V. V., Bobylev, A. V., Heinz, O. M., Kvon, A. Z., Markovich, D. M.: Characterization of 3-D wave flow regimes on falling liquid films. Int. J. Multiph. Flow **99**, 474–484 (2018).

[120] Tropea, C., Yarin, A., Foss, J. F. (Eds.): Springer Handbook of Experimental Fluid Mechanics, p. 681 (Springer, Berlin, 2007).

[121] Happel, J., Brenner, H.: Low Reynolds number hydrodynamics (Springer, Netherlands, 1983).

[122] Dauth, M., Schörner, M., Aksel, N.: What makes the free surface waves over topographies convex or concave? A study with Fourier analysis and particle tracking. Phys. Fluids **29**, 092108 (2017).

[123] Crocker, J. C., Grier, D. G.: Methods of digital video microscopy for colloidal studies. J. Colloid Interface Sci. **179**, 298 – 310 (1996).

[124] Allan, D., Caswell, T., Keim, N., van der Wel, C.: "Trackpy version 0.3.2." Zendo, 2016.

[125] Reck, D., Aksel, N.: Experimental study on the evolution of traveling waves over an undulated incline. Phys. Fluids **25**, 102101 (2013).

[126] Chiang, T. P., Sheu, Tony W.H., Wang, S. K.: Side wall effects on the structure of laminar flow over a plane-symmetric sudden expansion. Comput. Fluids **29**, 467 – 492 (2000).

Danksagungen

Diese Dissertation entstand während meiner Tätigkeit als wissenschaftlicher Mitarbeiter am Lehrstuhl für Technische Mechanik und Strömungsmechanik der Universität Bayreuth. Mein Dank gebührt insbesondere dem Lehrstuhlinhaber Professor Dr. Nuri Aksel für die exzellente Betreuung dieser Arbeit. Er nahm sich stets viel Zeit für Diskussionen über offene Fragestellungen, die mannigfaltige Anregungen und Denkanstöße lieferten. Unsere zahlreichen Gespräche werden mir immer als bereichernd und konstruktiv in Erinnerung bleiben. Besonders bedanken möchte ich mich zudem für das entgegengebrachte Vertrauen und die damit einhergehenden großen wissenschaftlichen Freiheiten. Regelmäßig räumte er mir außerdem die Möglichkeit ein, an internationalen Fachtagungen teilzunehmen, bei denen viele interessante Kontakte zu Forschungskollegen aus aller Welt aufgebaut und vertieft werden konnten.

Mein Dank gilt auch Professor Dr. Yuri Trifonov vom Intitute of Thermophysics, Siberian Branch of the Russian Academy of Sciences (Novosibirsk), für die ausgezeichnete Kooperation im Rahmen eines DAAD Projektes und darüber hinaus. Sowohl während seines Forschungsaufenthaltes in Bayreuth als auch auf internationalen Fachtagungen waren seine konstruktiven Ideen eine außerordentlich sachkundige und wertvolle Unterstützung.

Bei allen Mitarbeitern des Lehrstuhls für Technische Mechanik und Strömungsmechanik möchte ich mich ganz herzlich für die hervorragende Zusammenarbeit und die sehr angenehme, produktive und freundschaftliche Arbeitsatmosphäre bedanken. Insbesondere bei zahlreichen Fachdiskussionen mit meinen Kollegen Dr. Thilo Pollak, Dr. Daniel Reck, Markus Dauth und Armin Kögel entstanden wertvolle neue Ideen und Lösungsansätze, die es ermöglichten viele anspruchsvolle Projekte gemeinschaftlich weiterzuentwickeln. Hervorzuheben sind auch Marion Märkl, Gabriele Jena, Markus Horn und Stephan Eißner, deren Fachkenntnisse und handwerkliches Geschick sowohl bei Laborarbeiten als auch bei der Durchführung von Experimenten effizientes wissenschaftliches Arbeiten erst ermöglichten. Mein spezieller Dank gilt auch Andrea Siegmund, Kaori Laino, Maximilian Bauer, Peter Wagner, Moritz Faden, Dominik Schröder und Mario Linz, die durch ihre Tätigkeit als studentische Hilfskraft oder durch Studienarbeiten Beiträge und Anregungen zu dieser Dissertation lieferten. Bedanken möchte ich mich auch bei Dr. Lutz Heymann für seine stete Hilfsbereitschaft und sein Engagement, mir immer mit seiner Fachkenntnis als Diskussionspartner zur Verfügung zu stehen. Weiterhin danke ich Katja Helmrich für ihre kostbare Unterstützung bei organisatorischen Angelegenheiten und ihr jederzeit tatkräftiges und herzliches Entgegenkommen. Der Mechanikwerkstatt der Universität Bayreuth danke ich außerdem für die sehr gute und flexible Zusammenarbeit bei der Auslegung und Fertigung hochwertiger Versuchskomponenten.

Von ganzem Herzen danke ich meiner Frau für ihre Liebe und ihr Verständnis.

Ganz besonders herzlich möchte ich mich bei meinen Eltern für ihre uneingeschränkte, liebevolle und vielseitige Unterstützung auf meinem gesamten Lebensweg bedanken.

Selbstständigkeitserklärung

Hiermit versichere ich, dass ich die vorliegende Dissertation selbstständig verfasst und keine anderen als die von mir angegebenen Quellen und Hilfsmittel verwendet habe.

Ich erkläre, dass ich diese Dissertation nicht bereits zur Erlangung eines akademischen Grades eingereicht habe und dass ich nicht bereits diese oder eine gleichartige Doktorprüfung endgültig nicht bestanden habe.

Des Weiteren erkläre ich, dass ein gewerblicher Promotionsberater bzw. Promotionsvermittler weder bisher in Anspruch genommen wurde noch künftig in Anspruch genommen wird.

(Ort, Datum) (Dipl.-Phys. Mario Schörner)